# ULTRA-WIDE, LOW-MASS BINARIES: CONSTRAINTS ON BINARY FORMATION THEORY AND CALIBRATION OF FUNDAMENTAL STELLAR PARAMETERS

By

Saurav Dhital

Dissertation
Submitted to the Faculty of the
Graduate School of Vanderbilt University
in partial fulfillment of the requirements
for the degree of

DOCTOR OF PHILOSOPHY
in

PHYSICS

May, 2012

Nashville, Tennessee

Approved:
Keivan G. Stassun
Andrew A. West
Sydney A. Barnes
David A. Weintraub
Kelly Holley-Bockelmann
Thomas J. Weiler

To

Mamu & Daddy

who gave up their own dreams so mine could be formed.

# ACKNOWLEDGMENTS

For endless patience, tutelage, and encouragement as I learned the labyrinthine ways of research, my advisers, Keivan Stassun and Andrew West. For teaching me the value and ways of good writing and presentations, Keivan Stassun. For making sure I stayed focused and knew what I was doing, Andrew West.

For teaching me how to use a telescope: Sydney Barnes. For the excellent class on stellar structure: Andreas Berlind. For guiding my dissertation, committee members: Keivan Stassun, Andrew West, Sydney Barnes, Kelly Holley-Bockelmann, David Weintraub, and Thomas Weiler.

For forcing me to temporarily stop reading fiction and instead dive into college astronomy text books while in ninth grade, Comet Hale-Bopp. For helping deepen my love for Hale-Bopp and astronomy, Fr. Bill Robins, S. J. For endless guidance and help, my undergraduate adviser, Eric Jensen.

For their significant and indispensable help along the past five years, collaborators: Adam Burgasser, John Bochanski, Nick Law, and Kevin Covey. For giving me observing time for components of this dissertation and beyond: Kitt Peak National Observatory and Lowell Observatory. For providing me with the data and the basis of my dissertation: the Sloan Digital Sky Survey. For supporting me throughout my graduate student years: NSF grant AST-0909463 and NASA SIM grant. For support through the Dissertation Enhancement Grant and multiple travel grant: Vanderbilt Graduate School.

For being there during the thick and thin of graduate student years, be it to do astronomy or to create mischief: Alicia Aarnio, Phill Cargile, and Manodeep Sinha. For helping me get

through the endless tunnel that is graduate school: fellow graduate students Ron Belmont, Tommy Le Blanc, Doug Watson, Jennifer Piscionere, and Qingqing Mao. For endless support at various points in graduate school, a motley non-astronomy friends: Alev Atalay, John Williams, Anmol Tikoo, Arvind Nair, Kristy Simmons, Si-Ken Long, Niraj Dhungel, and Subodh Paudel.

For helping me continue seeing the wonders in physics and the might of gravity and ultimately stopping me from defecting to history, fellow (physics/astrophysics) Swatties: Zach Wolfson, Michelle Tomasik, Andy Skemer, Cynthia Wu, Jessica Gersh, Yusra Naqvi, and George Hang. For the four wonderful years where I learned more physics that I possibly could have imagined, Swarthmore professors: Eric Jensen, Amy Bug, John Boccio, Peter Collings, Catherine Crouch, David Cohen, Doc Brown, and Carl Grossman.

For simply being there, my family: Daddy, Mamu, Shweta, and Shaishab.

TABLE OF CONTENTS

LIST OF TABLES

LIST OF FIGURES

# CHAPTER I

# INTRODUCTION

## 1.1 Motivation: Decoding Formation of Ultra-wide Binary Stars

Star formation is widely believed to be dynamic process driven by local instabilities in the molecular cloud. Observations have virtually ruled out system-wide bulk properties (e.g., rotation) playing a large role in these processes. An average molecular cloud has a cross-section of ∼60,000 AU (0.3 pc); the star that results from its collapse is only ∼1/200 AU (1 $R_\odot$). The processes that precipitate and drive this collapse, over 7–8 orders of magnitudes in size, are by nature chaotic. The initial conditions—mass, size, temperature, angular momentum, and formation environment—can vary widely. The instability that leads to the collapse can be induced by thermal motion, convection, gravity, magnetic fields, or their combination (Stahler & Palla 2005). Yet, there is tremendous order; for example, the stellar initial mass function seems to be universal (Bastian et al. 2010).

Moreover, while we know a majority of cores fragment into two or more pieces, we do not understand what causes the fragmentation, how often is happens, or how angular momentum is conserved when it does not happen. Observations of young star-forming regions show that almost all stars are in binary or multiple systems; by this time they are mostly in stable equilibrium. So evidently they are formed well before the pre-main sequence stage (PMS; ∼1 Myr) of their lives (Mathieu 1994). The majority of solar-type F and G dwarfs in the field, for which the census is most complete, are also doubles (Duquennoy & Mayor 1991, hereafter DM91). The lower-mass M and L dwarfs are much more likely to be single, although a combination of dynamical evolution over time and the incompleteness of our surveys could account for the difference. Even so, star formation and binary star formation are generally regarded as one, and the same, question (e.g., Larson 2001).

Often times it is the extremes of a distribution that encode the most valuable information about the underlying physics. While the typical semi-major axis of a binary star system ($a$) is ∼30 AU, a large number of ultra-wide binaries ($a \gtrsim 10^5$ AU) have been identified. Almost 10–

15% of all binaries are expected to be wider than $10^3$ AU (Lépine & Bongiorno 2007), while 1–2% are expected to be wider than $10^5$ AU. However, systems with such large separations cannot be formed via fragmentation of the collapsing cloud core (see Section 1.4). Similarly, we do not understand how the tightest of binaries ($\lesssim 0.1$ AU) are formed. These two groups of binaries are boundary conditions of the binary formation process and provide valuable constraints to formation theories. Knowing what processes form these extreme systems and how they differ from, and interplay with, the ones that form the typical binary system is imperative to understand binary and, ultimately, star formation.

There are two possible scenarios that can produce binaries with $a \sim 10^{4-6}$ AU: dynamical widening and cluster dissipation. In dynamical widening, the outer orbit in a primordial hierarchical triple—a tight binary with a wide tertiary—or quadruple becomes wider via angular momentum transfer from the inner orbit. Once the outer orbit is wider than a few thousand AU, it can dissipate further via interactions with external potentials like the Galactic tide and giant molecular clouds, eventually resulting in $10^{4-6}$ AU systems. In cluster dissipation, the components of wide binaries are not formed together but get bound as they are ejected from their natal cloud cores or as they evaporate from star clusters (Kouwenhoven et al. 2010; Moeckel & Clarke 2011). These two scenarios offer completely different formulations for the formation of ultra-wide binary systems, with cluster dissipation radically different than our assumption of coevality of the stars in a multiple system (White & Ghez 2001; Kraus & Hillenbrand 2009a). If binaries do form during cluster dissipation is indeed physical, it will fundamentally alter how we think or binary and multiple systems and how they are formed. Currently, the fraction of binaries formed via any kind of capture processes is believed to less than 1–2% (Mathieu 1994). Moreover, the frequency and distributions of binaries formed during cluster dissipation could provide important insights into the substructure of the molecular clouds and star-forming regions. Lastly, as most stars are expected to have formed in large molecular clouds and later dispersed in to the field, binary formation via cluster dissipation has important implications on how single and binary stars populate the Galactic field.

In addition to putting constraints on models of star formation, the components of wide binary (or multiple) systems are ideal *coeval laboratories* to benchmark stellar evolutionary

models (e.g., Stassun et al. 2007, 2008) as well as to constrain and calibrate empirical properties/relations (e.g., Dhital et al. 2012; Chanamé & Ramírez 2012), as they were born at the same time of the same primordial material. Moreover, *identical twins* with the same initial conditions and properties (same mass, age, and metallicity) can be selected to explore the intrinsic variations of stellar properties. Binaries wider than ∼100 AU have the added benefit of having evolved completely independent of each other (Clarke 1992); they are effectively two single stars that share the same initial conditions and formation and evolutionary history. Therefore, a catalog of wide binaries—spanning large ranges in mass, metallicity, age, and evolutionary stages—would be an invaluable resource.

*The focus of this dissertation is to identify a large sample of ultra-wide binary systems. The resultant ensemble will then allow for the following two questions to be addressed: (1) What is the frequency and distribution of ultra-wide binary star systems in the Galactic field, and what can they tell us about formation processes? and (2) how can we use wide binaries to measure the fundamental parameters—specifically, metallicity and age—of low-mass stars?*

Historically, samples of ultra-wide binaries have been limited to bright and fast-moving stars in the local neighborhood. They had to be manually identified based on their common movement over time in photographic plates and, hence, previous investigations were time-consuming and error-prone. There were some studies that identified over-densities of stars from small, "complete" catalogs; but their scope was limited, and very few real pairs were able to be identified (see Section 1.5 for a review of the early work on wide binaries). However, with the advent of large scale, all-sky surveys, the potential for mining for large numbers of wide binaries was present. Not only did the surveys like the the Sloan Digital Sky Survey (SDSS; York et al. 2000) and the Two Micron All Sky Survey (2MASS; Cutri et al. 2003) have millions of stars in their catalogs, the astrometry and photometry are incredibly precise and accurate. Based on these catalogs, wide pairs can be identified based on their co-movement, as well as their over-density as compared to the Galactic field. In this dissertation, I will exploit the opportunity afforded by the SDSS and its catalog of more than 200 million stars with exquisite astrometry and multi-band photometry (Abazajian et al. 2009) as well as proper motions measured by cross-matching with the USNO-B catalog (Munn et al. 2004).

## 1.2 Characteristics of Young and Old Binary Populations

The past two decades have seen a tremendous leap in our understanding of binary and multiple star systems and of the processes that precipitate and govern their formation and early dynamical evolution. Following the pioneering works of Heintz (1969) and Abt & Levy (1976), long-term observational programs have robustly characterized the binary populations across the main sequence (MS) for the O and B (e.g., Gies 1987; Mason et al. 1998), F and G (DM91; Raghavan et al. 2010), M (e.g., Fischer & Marcy 1992; Henry & McCarthy 1993; Reid et al. 2003), and L (e.g., Burgasser et al. 2003b; Close et al. 2003; Basri & Reiners 2006; Burgasser et al. 2007c) dwarfs. Despite the significant challenges presented by several magnitudes of extinction due to gas and dust, a combination of various imaging and spectroscopic techniques have been used to constrain the binary populations in the protostellar (e.g., Duchêne et al. 2004; Haisch et al. 2004; Connelley et al. 2009), T Tauri stages in star-forming regions (e.g., Ghez et al. 1993; Leinert et al. 1993; Reipurth & Zinnecker 1993; Kohler & Leinert 1998; Duchêne 1999; Duchêne et al. 1999; Ratzka et al. 2005), and in open clusters (e.g., Patience et al. 1998, 2002; Bouvier et al. 2001; Kraus & Hillenbrand 2009b). Increased computing capabilities have also meant realizations of much larger and longer simulations using smoothed-particle hydrodynamic (SPH; Goodwin et al. 2004a,b; Bate 2009, 2011) and adaptive mesh refinement (AMR; Offner et al. 2008, 2010; Kratter et al. 2008) techniques. Here, we briefly review the characteristics of binary stars in the PMS and MS stages as well as our current understanding of the formation mechanisms. The focus will be on stars of a few solar masses to a few tenths of a solar mass, which together constitute >90% of the stellar population. For in-depth discussions, interested readers are recommended recent reviews on binary formation (Tohline 2002; Goodwin et al. 2007) and PMS populations (Mathieu 1994; Mathieu et al. 2000; Duchêne et al. 2007).

*Multiplicity:* While binary frequency is simply the fraction of binary stars in the total population, defining and using a multiplicity fraction is more physically relevant. For the purposes of this dissertation, we adopt the multiplicity frequency (Reipurth & Zinnecker 1993),

$$f_{\rm mult} = \frac{B + T + Q + \ldots}{S + B + T + Q + \ldots}, \tag{1.1}$$

where S, B, T, and Q refer to the number of single, binary, triple, and quadruple systems, respectively. $f_{\rm mult}$ quantifies the the fraction of the observed systems that are in multiple systems.[1] In the absence of higher-order systems, the multiplicity fraction simply reduces to binary fraction.

Multiplicity has been measured to decrease with the mass and age of the system. It is also highly dependent on the environment in which a system is formed. Wulff Heintz was the first to do a statistical study of the binarity fraction and found that higher mass stars were more likely to be in multiple star systems (Heintz 1969). Among the higher-mass O and B stars, most multiple systems are binaries; more than 75% of stars in clusters and associations are in multiple systems while only 58% of the field stars are multiples. Among runaway stars, the fraction decreases to 26% (Mason et al. 1998). This is generally consistent with the idea that the runaway and field stars are dynamically ejected or dispersed from clusters, when some binaries may be disrupted.

In what is regarded as the seminal study on multiplicity, DM91 found $f_{mult} = 0.58$ (0.49 without being corrected for incompleteness) for solar-type F and G dwarfs in the local neighborhood (see also Abt & Levy 1976; Halbwachs et al. 2003). Raghavan et al. (2010) revisited the issue with a larger sample, some of which overlapped with the DM91 sample, and found a raw $f_{mult} = 0.46$. However, they argued that very few undiscovered companions remain in their sample and large corrections to the observed $f_{\rm mult}$ were unnecessary. Additionally, DM91 assumed a large fraction of undetected low-mass and brown dwarf companions, which have still not been detected today even with better sensitivity. However, Raghavan et al. (2010) did find that the increased sensitivity resulted in twice as many triples and quadruples as found in DM91.

The low-mass M dwarfs have a lower multiplicity of 0.35–0.42 (Fischer & Marcy 1992; Henry & McCarthy 1993; Reid & Gizis 1997); however, this analysis is dependent on ex-

[1] Another useful quantity is the companion frequency that refers to the number of companions, on average, around an individual star (Reipurth & Zinnecker 1993):

$$f_{\rm comp} = \frac{2B + 6T + 12Q + \ldots}{S + 2B + 3T + 4Q + \ldots}.$$

.

trapolations that assume a similar distribution as the DM91 study. Continuing this trend of decreasing multiplicity, only 10–25% of brown dwarfs are in multiple systems (Bouy et al. 2003; Close et al. 2003; Gizis et al. 2003; Martín et al. 2003; Basri & Reiners 2006). However, given the bias toward very close separations which are not well-probed by existing observations, the multiplicity could plausibly be as high as 50% (Pinfield et al. 2003; Maxted & Jeffries 2005). Due to their intrinsic faintness, multiplicity surveys of M and L dwarfs have been limited to <100 stars, limiting their significance. The studies assume distributions similar to that of FGK dwarfs whereas, given their lower masses, they could have formed in a very different manner. Indeed, the L dwarfs are probably ejected protostars (Reipurth & Clarke 2001). These surveys are especially lacking at the largest separations, given the lack of wide, all-sky surveys that were sensitive to low-mass stars. Therefore, a survey of low-mass star (LMS) and very low-mass (VLM) star binaries would be a tremendous addition.

Multiplicity in PMS populations is significantly higher than in the field. However, there are significant variations depending on stellar density in the cluster. For $a \sim$ 100–2000 AU, Taurus, Ophiucus Chameleon, Lupus, and Corona Australis (Ghez et al. 1997; Kohler & Leinert 1998) and Hyades (Patience et al. 1998) have twice as many binaries as in the field. Extrapolating this to all separations, Duchêne (1999) concluded that the overall binary fraction can be ∼90–100% for Taurus. On the other hand, denser star-forming regions like the Trapezium in the Orion Nebula (Simon et al. 1999; Petr et al. 1998) and IC 348 (Duchêne et al. 1999) as well as in the Pleiades (Bouvier et al. 1997) and Praesepe (Bouvier et al. 2001) open clusters have a binary frequency similar to that in the field. There is also a significant difference in multiplicity fraction among the embedded and non-embedded regions of Taurus and Orion, suggesting that dynamical decay, or "dissipation of binaries," plays a large role, perhaps even before the onset of the PMS phase (∼1 Myr).

*Semi-major axis(a):* Figure 1.1 shows the distribution of semi-major axes for the G dwarf sample observed by DM91. It can be described by a log-normal Gaussian distribution with a mean of $a \sim$31 AU and standard deviation of $\sigma_{\log a} = 1.53$. The raw distribution, without the incompleteness corrections, is well-described by a Gaussian distribution (Raghavan et al. 2010). The lower-mass M dwarf distribution also peaks around the same value, although significant extrapolations and incompleteness corrections are needed due to small sample

sizes (Fischer & Marcy 1992). The brown dwarf distribution peaks around ∼4 AU (e.g., Burgasser et al. 2007c) but the spread is not well-constrained with suggested values of $\sigma_{\log a}$ ranging from 0.40 (Thies & Kroupa 2007) to 0.85 (Basri & Reiners 2006).

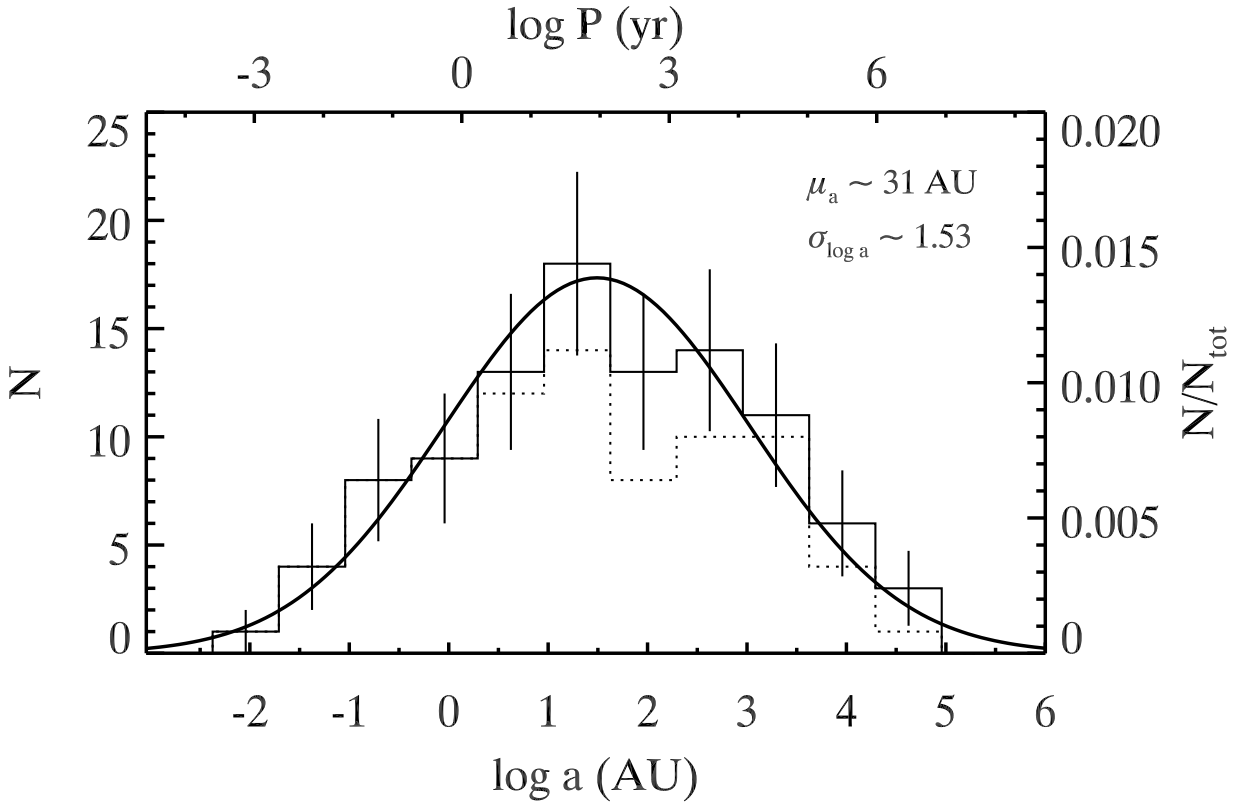


Figure 1.1: The distribution of semi-major axes, or $\log a$, after correcting for completeness biases (solid histogram), of nearby G dwarf binaries from the seminal study of DM91 can be described by a log-normal with $a \approx 31$ AU and $\sigma_{\log a} = 1.53$. The raw distribution is shown as the dotted histogram. The orbital period for a system, assuming $M_{tot} = 1\ M_{\odot}$, is shown on the top x-axis while the right y-axis shows the scale for a normalized Gaussian distribution.

*Mass ratio ($q = M_2/M_1$):* The observed mass ratio distribution seems to be very strongly dependent on the mass or the primary star. This might be an intrinsic property of the binary formation process—after all, whether the mass distribution of the secondary component follows the field mass function or not is central to distinguishing between formation mechanism—or a result of observational biases. O and B stars exhibit a dearth of low

mass-ratio ($q < 0.4$) systems for short-period binaries but a flat distribution for systems with orbital periods $\gtrsim$30 days (Abt et al. 1990; Mason et al. 1998). The lack of low-$q$ systems could be due to the difficulty of identifying low-mass, close companions to these high-luminosity stars, so a better understanding of the observational biases against these systems is imperative.

Among FGK dwarfs, short period binaries have been found to be biased toward having the mass ratio of or near unity (Mazeh et al. 1992). However, as a whole sample, there is a preference to be in systems low values of $q$ but the distribution of the secondaries does not follow the field mass function DM91. For M dwarfs, perhaps due to small sample sizes, the distributions have to be found to be similar to (Fischer & Marcy 1992) or incompatible with (Reid & Gizis 1997) the field mass function. Reid & Gizis (1997) find strong evidence for the survival of only the equal-mass ratio systems, i.e., the secondaries in field binaries follow the mass function of the primary. As the field mass function peaks around the ∼M4 (Bochanski et al. 2010), mass ratio distributions in M dwarfs might not be a good way to distinguish whether the secondary mass function follows the primary or the field mass functions (Chapter II).

*Eccentricity (e):* The eccentricity distribution for field dwarfs seems to be thermalized for periods $P \gtrsim 10^{3-4}$ d with tidal circularization happening at $P \lesssim 10 - 15$ d (DM91; Fischer & Marcy 1992, Meibom & Mathieu 2005). The PMS population is similar except that the tidal circularization is incomplete at ages less than ∼1 Myr (White & Ghez 2001; Meibom & Mathieu 2005). A lack of circular orbits at periods longer than the circularization period has been noted (Halbwachs et al. 2003), perhaps suggesting that binary systems do not naturally form with circular orbits.

*Age:* While the age of MS stars is notoriously hard to measure as their properties change very little between the time they arrive and leave the MS (Soderblom 2010), the age of PMS stars can be estimated using evolutionary models (e.g., D'Antona & Mazzitelli 1997; Baraffe et al. 1998). White & Ghez (2001) and Kraus & Hillenbrand (2009a) have conducted extensive surveys of T Tauri binary systems in the Taurus-Auriga star-forming region and found them to be coeval to $\lesssim$1 Myr, with the difference in ages (∼0.30–0.40 dex) comparable to the uncertainty involved in estimating the ages. When factors that could affect the age

estimate (e.g., unresolved multiplicity, disk contamination) are accounted for, the dispersion in relative ages decreases to 0.16 dex, typically a factor of 1.5 (Kraus & Hillenbrand 2009a).

On the other hand, observations of eclipsing binaries have suggested that components of a binary system could be non-coeval by as much as ∼0.5 Myr (Stassun et al. 2007, 2008). This timescale is much larger than the ∼0.1 Myr dynamical collapse timescale. The age difference between the components does not depend on the evolutionary models used; and, at these young ages, seems to manifest itself as surprisingly large difference in luminosity and/or temperatures. However, compared to the ages of stars in the field (∼1–10 Gyr), this difference in the age of components of a binary system is very, very small and nowhere near detectable given our current age-dating methods.

**So I still kind of want a summary here that says what we don't know and what challenges/questions are left so that we know why you are doing this.**

### 1.3 Our Current Understanding of (Binary) Star Formation

Theories for formation of binary systems have included fission, capture, and fragmentation. Jeans (1919) suggested that a rapidly rotating protostar, in quasi-equilibrium, will split into two parts due to the increasing angular momentum. However, numerical simulations demonstrated that for compressible liquids, like a star or a polytrope, spiral arms develop and help distribute the angular momentum and fission does not occur (Durisen et al. 1986; Bonnell 1994; Imamura et al. 2000). Similarly, capture of any manner—due to interactions with a third star, circumstellar disk, or tidal interaction between two stars—is (i) too inefficient to account for the multiplicity frequency and (ii) cannot account for the large range of observed separations. That leaves fragmentation into two or more parts due to the self-gravity of a dynamically evolving core (Larson 1981); it seems to be the mechanism that forms binary stars with masses from a few solar masses to the substellar limit.

### 1.3.1 The Virial Theorem

A stable, gravitationally bound molecular cloud—of mass $M$, radius $R$, temperature $T$, and mean density $\rho$—in equilibrium can be described by the virial theorem,

$$2(K_{\rm therm} + K_{\rm rot}) + U = 0 \tag{1.2}$$

where the thermal kinematic energy, the rotational kinetic energy, the gravitational potential energy of the gas are given by

$$K_{\rm therm} = \frac{3}{2}NkT = \frac{3MkT}{2\mu m_{\rm H}}, \tag{1.3}$$

$$K_{\rm rot} = \frac{1}{2}I\omega^2 = \frac{1}{5}MR^2\omega^2, \tag{1.4}$$

$$U = -\frac{3GM^2}{5R}, \tag{1.5}$$

respectively. $N$ is total number of molecules, $k$ is the Boltzmann constant, $\mu$ is the mean molecular weight of the gas, $m_{\rm H}$ is the mass of an hydrogen atom, $\omega$ is the angular velocity of gas, and $G$ is the gravitational constant. For simplicity, the cloud is assumed to be spherical and isothermal.

The star formation process is precipitated when a portion(s) of a molecular cloud becomes denser due to a local perturbation or random fluctuation. If the pressure due to the thermal motion or the rotation of the gas is big enough to overcome the self-gravity of the gas, the instability is smoothed; and the equilibrium is restored. However, if the instability happens over a big enough volume, the self-gravity overcomes the internal pressure and the cloud collapses to eventually form a protostar. The minimum perturbed mass needed to overcome the equilibrium is given by

$$\begin{aligned} M_J &= \frac{4\pi}{3}\left(\frac{\pi k}{G\ \mu\ m_{\rm H}}\right)^{3/2}\ T^{3/2}\ \rho^{-1/2} \\ &= 1.0\ M_\odot \left(\frac{T}{10\ {\rm K}}\right)^{3/2}\left(\frac{N}{10^4\ {\rm cm}^{-3}}\right)^{-1/2}. \end{aligned} \tag{1.6}$$

This is known as the Jeans criteria (Jeans 1919) and $M_J$ is the Jeans mass. This can be

rewritten in terms of the Jeans length, which is the minimum radius initial required for a collapse under its own self-gravity:

$$R_J = \sqrt{\frac{\pi\ k}{G\ \mu\ m_{\rm H}}}\ T^{1/2}\ \rho{-}1/2$$
$$= 0.19\ \mathrm{pc} \left(\frac{T}{10\ \mathrm{K}}\right)^{1/2} \left(\frac{N}{10^4\ \mathrm{cm}^{-3}}\right)^{-1/2}. \quad (1.7)$$

Typical dense H II regions have a mass of ∼11 $M_\odot$, a radius of ∼0.35 pc, and a density of $10^3$ cm$^{-3}$ with most of the gas colder than 30 K (Clemens et al. 1991). Hence, they are on the brink of gravitational instability. Some of the observed regions, in fact, have already started their collapse, with the gas decoupling from the dust and being significantly hotter (Clemens et al. 1991). Recent surveys also suggest an evolutionary trend between starless cores and cores that have already formed protostars: the cores contract to become smaller and denser at a fixed mass (Enoch et al. 2008).

### 1.3.2 The Collapse Process

Figure 1.2 shows the evolution of a 1 $M_\odot$ cloud—composed mostly of molecular hydrogen ($H_2$) at 10 K—in terms of gas temperature ($T$), Jean's mass ($M_J$), and Jeans radius ($R_J$) as a function of its mean density ($\rho$). The cloud becomes unstable at $\rho \sim 1.2{\times}10^{-18}$ g cm$^{-}3$ (point A), where the rate of compressional heating is balanced by radiative cooling (via molecular line emission and thermal coupling with the dust, the latter of which cannot happen at lower densities); and the cloud begins the isothermal phase ($P \propto \rho$) of its collapse. As the collapse accelerates and density continues to increase, the cloud becomes opaque to IR radiation, heats up, and turns adiabatic ($P \propto \rho^\gamma$ where $\gamma = 7/5$ and is the adiabatic exponent). This switch from isothermal to adiabatic collapse happens around $\rho_{crit} = 10^{-13}$ g cm$^{-}3$ (point B), and marks the first minimum of $M_J$ at $\sim 0.004 M_\odot$ ($R_J \sim 30$ AU). This is the first time that the core can fragment into two or more pieces. with the resulting binary being ∼100 AU wide.

As the core continues to collapse, the gas becomes hot enough to disassociate the $H_2$ causing the core to become unstable. During this phase, $T$ increases slightly and $M_J$ de-

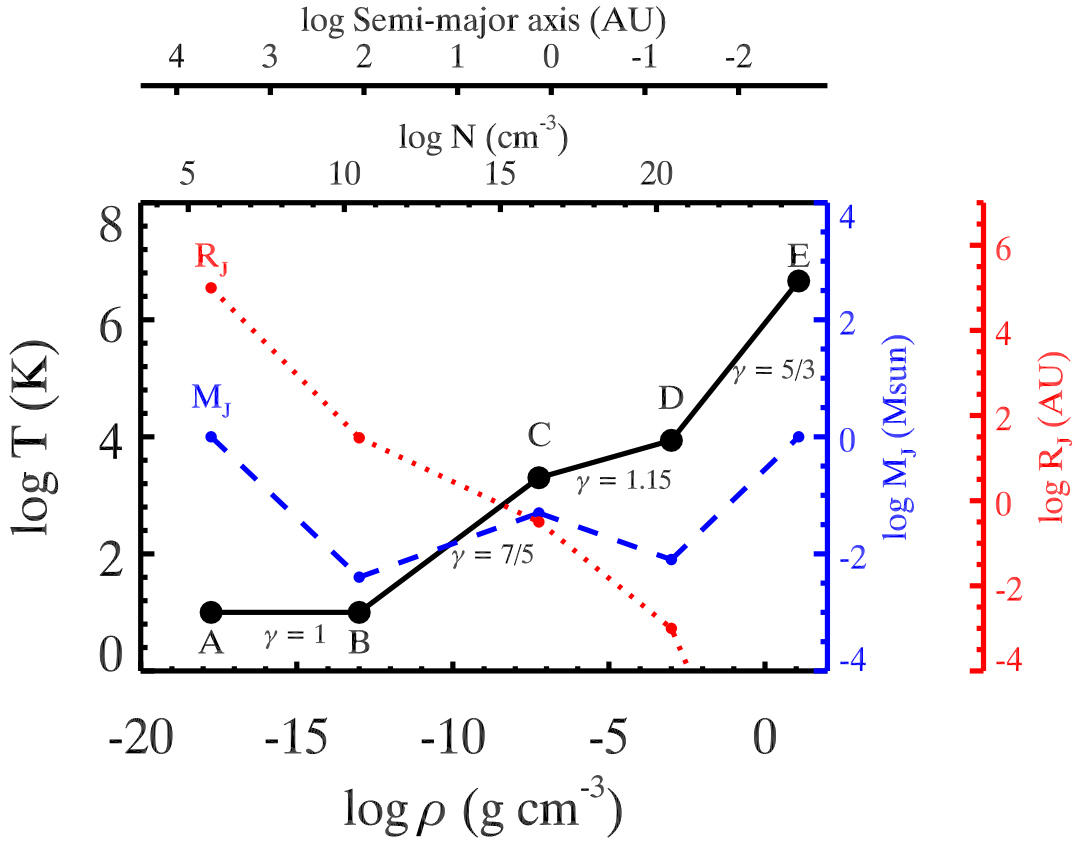


Figure 1.2: The gas temperature (solid, black line), Jeans mass (dashed, blue line), and Jeans radius (dotted, red line) of a 1 $M_\odot$ molecular cloud as a function of mean density as it collapses. The upper x-axes show the molecular density of $H_2$ and the semi-major axis of the binary that would form from a cloud of that mass and radius. B and D mark the two points where the core is allowed to fragment. Once a molecular cloud becomes unstable, it does not stop collapsing until it reaches stellar proportions (E). Plot adapted from Tohline (2002).

creases. This only stops when all the $H_2$ is in atomic state (point D). At this point, $M_J$ has another minimum and can fragment, forming binaries as small as ∼0.1 AU. If the core fragments at this point, its mass will be a minuscule ∼0.008 $M_\odot$. The core then begins its final collapse phase and becomes a protostar (point E), where virial equilibrium is finally attained and the collapse can stop.

The third and the last phase where fragmentation can happen is in the protostellar disk, which is generally precipitated by a rotational instability or a gravitational perturbation

(Bonnell 1994; Bate et al. 2003). Disk fragmentation tends to produce lower-mass companions, and only large disks around high-mass star tend to have enough material to produce a stellar-mass companion. However, recent numerical experiments have shown that in large disks around high-mass stars a companion core can accrete enough material to become as massive as the primary (Kratter et al. 2008). Given the large fraction of close binaries in O and B stars, disk fragmentation could be responsible for the creation of these systems.

### 1.3.3 Binary Formation via Turbulent Fragmentation

A collapsing molecular cloud has significant variations in local velocity gradients in both directions and magnitude, suggesting motion is much more complex and chaotic than a simple solid-body, bulk rotation (Caselli et al. 2002). These variations could be indicative of velocity and/or density imhomogeneities in the core, which would precipitate fragmentation. Simulations of core formation have also shown that there is a significant amount of turbulence present in the core; evolution of such turbulent cores also reproduce many of the observed properties (see review by Goodwin et al. 2007, and references therein).

Moreover, the line widths from even the most quiescent, dense cores cannot be explained by just thermal motion. Observations have shown that the coldest isolated cores have a temperature of ∼10 K and dust temperatures of 6–12 K. For a gas temperature of 10 K, the $H_2$ $1\sigma$ velocity dispersion should be about 0.2 km s$^{-1}$, which is at the very low-end of the observed values (between ∼0.2–1 km s$^{-1}$, with the peak at 0.4 km s$^{-1}$). Hence, local velocity gradients have been attributed for the higher observed dispersion (Goodwin et al. 2007).

Smoothed particle hydrodynamics (SPH) simulations for turbulence-driven binary formation have also shown that turbulence can effectively produce binary systems as wide as 30 AU. Generally, such simulations are set up to mimic the parameters of an observed cloud core. A Plummer-like[2] potential is assumed, and turbulent velocity field[3] is initialized as $P(k) \propto k^{-n}$ where $k = 3 - 4$.

[2]The Plummer potential is described by $\rho(r) = \frac{\rho_c}{(1+(r/R_c)^2)^2}$ where the subscript $c$ denotes the value at the center of the core.

[3]The average line-of-sight velocity dispersion, $\sigma$, of molecular clouds depends on their linear size, $L$, as $\sigma = 1.10 km\ s^{-1}(L/\mathrm{pc})^{3.8}$ (Larson 1981).

Even at low levels of turbulence—as quantified by the turbulent virial ratio, $\alpha_{\rm turb} = K_{\rm turb}/|U|$—a high fraction of stellar systems are multiple. In the Goodwin et al. (2004b) simulations of an isolated 5.4 $M_\odot$, 0.1 pc core (set up to mimic L1554), $\alpha_{\rm turb} = 0.05$ was used and produced binaries 80% of the time. In fact, at $\alpha_{\rm turb} = 0.10$ multiple systems are more frequent than in observed samples. However, as a population of cores are unlikely to be encoded with the same turbulent virial ratio, a distribution of $\alpha_{\rm turb}$ values is more realistic. Goodwin et al. (2004b) were able to reproduce the observed binary frequency in Taurus by using a 2:2:1 mixture of $\alpha_{\rm turb} = 0.05$, 0.10, 0.25 simulations. Simulations with higher levels of turbulence have also been conducted; (Delgado-Donate et al. 2004a,b) and (Bate et al. 2002, 2003; Bate & Bonnell 2005) all used $\alpha_{\rm turb} = 1$ in their simulation of 5 $M_\odot$ and 50 $M_\odot$ clouds, respectively.

In the low-turbulence case with $\alpha_{\rm turb} = 0.05$, Goodwin et al. (2004a) find that the initial collapse causes a significant over-density near the center of the core. Due to the local spin angular momentum or the merging of two turbulent flows, the core gets flattened and forms the primary star near the center of the mass of the core. This happens within one free fall time ($\tau_{\rm ff}$ $\sim$0.05 Myr) as the turbulence is not able to support the core for long. In the high-turbulence cases, the outward pressure is much higher and the core actually expands before collapsing. In all cases the primary star, once formed, starts to grow rapidly with the surrounding material accreting preferentially into the plane of the flattened core forming a circumprimary disk. The lumpy, variable accretion causes the disk to become unstable to spiral modes and fragment to form secondary objects, usually at $\sim$0.07–0.08 Myr. When multiple objects are formed in the same core, they can merge or get dynamically ejected. Most systems are formed with separations of $\gtrsim$20 AU, with closer systems formed solely via hardening caused by either accretion or ejection of low-mass objects (Goodwin et al. 2004a).

The number of cores formed via fragmentation increases with turbulence, with even very low levels of turbulence ($\alpha_{\rm turb}$) inducing fragmentation. However, observed low levels of non-thermal motion in cloud cores rule out high levels of turbulence (Goodwin et al. 2007).

The results of the simulations depend only on the level of turbulence and the initial velocity field. The number of objects formed seems to depend on how efficiently the turbulent flows can deliver material to the over-dense region. This is notably different from the

rotation-driven fragmentation in that the inflow is caused by local turbulence, not initial bulk rotation of the core. Hence, a core can form anywhere from 1 to 10 objects depending on how the turbulent velocity fields are seeded. Such chaotic behavior suggests that star formation can only be explained by an ensemble of scenarios, with a wide range of turbulence levels, initial core mass, and density.

## 1.4 Formation of Ultra-wide Binaries

While turbulent fragmentation seems to be the mode of binary star formation, it cannot produce produce primordial binaries that are 10,000–100,000 AU wide. After all, a typical protostellar core is only ∼20,000 AU (Clemens et al. 1991). However, as discussed above, a large number of wide binaries have been identified in the field; Lépine & Bongiorno (2007) have suggested a wide binary fraction of >10%. Similarly, protostellar (Connelley et al. 2008) and PMS (in Taurus and Upper Sco; Kraus & Hillenbrand 2009a) binaries as wide as ∼25,000 AU are known to exist. How these extremely wide systems is not understood. There are two plausible mechanisms that could produce such systems:

1. *Dynamical Widening*: A primordial hierarchical triple or quadruple—a tight binary with a wide tertiary or two tight binaries that are gravitationally bound—can dynamically evolve by tranferring angular momentum and energy to the outer orbit from the inner one. This results in the hardening of the inner binary and softening of the outer binary. Once the outer orbit is a few thousand AU large, it can further dissipate via interactions with the Galactic tide, giant molecular clouds, or other stars in the field (Weinberg et al. 1987; Kiseleva et al. 1998; Jiang & Tremaine 2010). With time this can produce extremely wide binaries, albeit ones that are slowly getting unbound. These dynamical interactions have been shown to be effective in widening and eventually dissolving wide binaries assuming fictitious initial separations (e.g. Weinberg et al. 1987). However, without knowing the initial (or final) distribution of wide binaries, the viability or the efficiency of such processes in forming ultra-wide systems was not possible.

   Observationally, a significant excess of wide tertiaries around known spectroscopic

binaries has been observed (Tokovinin 1997, 2000), suggesting that angular momentum transfer is the major mechanism for forming the sub-0.1 AU systems.

2. *Cluster Dissipation*: Results of N-body simulations have recently suggested that the majority of binaries wider than ∼1000 AU may not have been formed primordially. Instead, as stars are ejected from multiple systems (or protostellar cores are ejected from their natal clouds) some of them get bound and form loosely-bound binaries (Kouwenhoven et al. 2010; Moeckel & Clarke 2011). Alternatively, they could be stars that are evaporating from open clusters as it dissolves. It has also been suggested that stars primarily evaporate from Roche lobe-like tidal tails in clusters (Küpper et al. 2010). The probability of two stars getting bound is higher in this scenario as they have been shepherded into similar phase space into the tidal tails. Sometimes they might only be bound temporarily or might not even be bound but could appear to be bound in projected velocity space to a far-away observer.

   The probability of such bindings increases exponentially with the number of bodies involved, as it becomes easier to rearrange angular momentum and potential energy. Presumably, other stars or even the natal cluster or molecular cloud could act as facilitators. Some bindings could involve a tight binary that survived the ejection, thus, forming a hierarchical triple (or quadruple).

To discriminate between the two scenarios, a large sample of wide binaries is necessary. It is unlikely that a single mechanism is responsible for forming all ultra-wide binaries, so distinguishing between the populations formed via different mechanism should provide important insights into the star formation formation. In particular, the distribution and frequency of hierarchical multiples and the physical size of the inner orbit in hierarchical multiples would provide valuable insight. However, given the large separations of these binaries, measuring the ensemble properties is fraught with degeneracies as the orbital properties of such systems are mere projections.

## 1.5 Catalogs of Wide Binaries

The orbital periods of ultra-wide binaries (orbital separation, $a, \gtrsim 1000$ AU) are much longer than the human timescale: orbital period, $P, = 31,600$ yr for a systemic total mass, $M_{tot}$, $= 1$ $M_{\odot}$ and $a = 1000$ AU. Indeed, until the 1970s, such large spatial separations and orbital periods meant that they were not regarded as gravitationally bound, binary systems. Willem J. Luyten was the first to report common proper motion (CPM) binaries that he found with a blink microscope. He "believed that most of them actually belong together physically" (Luyten 1927). Luyten's work on surveys of high proper motion stars using Schmidt telescope plates, and a blink microscope, led him to eventually identify more than 6100 CPM binaries (Luyten 1927, 1969, 1972, 1977, 1979c, 1984, 1987, 1988, 1997). Largely due to Luyten's efforts, the conversation has shifted from whether CPM pairs are real binaries to identifying and utilizing them to study various types of science questions.

Without the luxury of retracing the orbits, ultra-wide binary systems have been identified primarily via two methods:

1. *Two-point correlation:* This technique can be used to identify excess pairs at small angular separations by comparing it to pairing that would be produced by the distribution of single stars. The resultant sample, however, is merely statistical. See Bahcall & Soneira (1981), Garnavich (1988), Wasserman & Weinberg (1991), and Longhitano & Binggeli (2010) for other studies that use this method.

2. *Common proper motion pairs:* To reduce the number of false positives inherent in the above, one can use additional information such as proper motions. Orbital motions for wide systems are small; hence, the space velocities of a gravitationally bound pair should be the same, within some uncertainty. In the absence of radial velocities, which are very hard to obtain for a very large number of field stars, proper motion alone can be used to identify binary systems. Luyten pioneered this technique, which has since been used by many other groups (Poveda et al. 1982; Halbwachs 1986; Allen et al. 2000; Chanamé & Gould 2004; Lépine & Bongiorno 2007; Sesar et al. 2008; Dhital et al. 2010).

We briefly summarize some of these studies below, in roughly chronological order:

- Between 1927 and 1988, Willem Luyten used a blink microscope to identify 6126 fast-moving ($\mu > 100$ mas yr$^{-1}$) CPM pairs from his Luyten Half-Second (LHS; Luyten 1979a) and the New Luyten Two-Tenths (NLTT; Luyten 1979b) catalogs. However, Luyten's identification of CPM pairs was done manually from a catalog with crude photometry and large proper motion errors; as a result, the listing of CPM pairs is incomplete and contains a significant number of chance alignments at the larger separations. He also did not record individual proper motions for stars that he believed were CPM pairs necessitating remeasurement of their proper motions so as to prove their fidelity (Chanamé & Gould 2004).

- Bahcall & Soneira (1981) used the two-point correlation function to calculate clustering scale among stars in the Weistrop catalog (a 13.5 deg$^2$ field in the direction of the North Galactic Pole; Weistrop 1972). Comparing the expected distribution of stars from their Galaxy model (Bahcall & Soneira 1980a,b), they found an excess of pairs at small separations and identified 20 pairs with angular separations of 10–120$''$. However, in a radial velocity followup, Latham et al. (1984) found only 6 of the 19 systems to be real.

- Halbwachs (1986) identified 326 pairs, with a false positive rate of 1%, from the AGK 3 catalog by matching proper motions.

- Based on the revised New Luyten Two-Tenths catalog (rNLTT; Gould & Salim 2003; Salim & Gould 2003), Chanamé & Gould (2004) identified 999 CPM binary systems, with $\mu > 180$ mas yr$^{-1}$, based on their proper motions and reduced proper motions. The catalog consisted of both disk and halo pairs, at separations up to $\Delta\theta = 900''$ and $a \gtrsim 1$ pc. They found the separation distribution of disk and halo populations to be similar, leading them to conclude that their formation histories must be similar. Ryan (1992) and Allen et al. (2000) also identified 25 and 122 binaries, respectively, from the NLTT catalog, most of which are included in the Chanamé & Gould (2004) catalog.

- Lépine & Bongiorno (2007) identified 521 CPM systems with a *Hipparcos* primary and a fainter secondary in Lepine-Shara Proper Motion-North (LSPM-N; Lépine &

Shara 2005) catalog at $\Delta\theta < 3$–$1500''$. All of these were high proper motion pairs with $\mu > 150$ mas yr$^{-1}$. The study noted a deficiency of systems with low-mass companions.

- Sesar et al. (2008) used the SDSS photometric catalog to identify a catalog of 22,000 pairs, with a ∼37% false positive rate, by minimizing the difference in the distance moduli. A smaller sample of about 5000 pairs also have common proper motion. The pairs are 2000–47,000 AU wide and are at distances up to ∼4 kpc. The sample has a high level of statistical completeness; however, a very low minimum proper motion cutoff, $\mu > 15$ mas yr$^{-1}$, that is only 2–3× larger than the typical error results in a catalog that is highly contaminated.

- Longhitano & Binggeli (2010) used the two-point correlation function to predict the presence of >800 pairs with physical separations of 0.1–0.8 pc in the SDSS photometric catalog in ∼675 deg$^2$ centered at the North Galactic Pole.

- Dhital et al. (2010, included in this dissertation) identified 1342 disk and halo low-mass pairs from the SDSS photometric catalog based on a statistical matching of proper motion components and photometric distances. The pairs had $\Delta\theta = 7$–$180''$ and $\mu > 40$ mas yr$^{-1}$. A Galactic model based on stellar number density and space velocity distributions was used to calculate the probability of chance alignment for each candidate pair; the resultant catalog only contains pairs with <5% probability of chance alignment. They used a highly rigorous selection algorithm and criteria to assemble a sample that is highly efficient for followup studies. In a followup study that measured radial velocities of 113 pairs from the catalog, Dhital et al. (2012) found the fidelity of the catalog to be >88%.

## 1.6 M Dwarfs

M dwarfs are low-mass stars (∼0.08–0.6 $M_\odot$) that make up ∼70% of all stars in the Galaxy (Henry & McCarthy 1993; Bochanski et al. 2010) making them, perhaps, the best tracers of the structure and kinematics of the local Milky Way and its components. Moreover, with lifetimes much longer than the age of the Universe, they are also the ideal tracers of

the chemical, dynamical, and evolutionary history of the Milky Way. However, as denizens of the bottom of the main sequence, they are intrinsically faint (luminosity, $L \lesssim 0.05\ L_{\odot}$), which hashistorically limited detailed studies of individual M dwarfs as well as construction of large samples of M dwarfs to enable statistical studies of their properties.

Loosely defined, the M spectral type comprises of main-sequence stars bracketed by the hydrogen-burning limit ($\sim$0.08 $M_{\odot}$) and the onset of molecular lines in the photosphere ($\sim$0.6 $M_{\odot}$).[4] Stars also turn fully-convective at the M3–M4 spectral types ($\sim$0.35 $M_{\odot}$ Chabrier & Baraffe 2000). As the regime where multiple major changes in the stellar interior are taking place, M dwarfs are especially interesting to study and challenging to understand.

In particular, a fundamental stellar property—metallicity—remains ill-calibrated. While spectral modeling has allowed for estimation of spectral parameters of OB through mid-K stars (e.g., Valenti & Fischer 2005), such efforts in the late-K and M spectral type regimes, similar efforts have met with notable problems, due to the ubiquitous broad molecular lines and the resulting incomplete line lists and uncertain opacities (e.g., Hauschildt et al. 1999). Recent efforts based on difficult, high-resolution spectroscopy have yielded [Fe/H] estimates (e.g., Woolf & Wallerstein 2005; Woolf et al. 2009) but with large error bars ($\sim$0.3 dex) and only in limited temperature and metallicity ranges. As a result, most metallicity studies have relied on either relative metallicity indicators (Lépine, Rich, & Shara 2007, hereafter LRS07) or photometric relationships (Johnson & Apps 2009; Johnson et al. 2011). Recent efforts to measure [Fe/H] based on near infrared features show promise but need to be tested and calibrated for a larger ranges of metallicity and temperature (Rojas-Ayala et al. 2010, 2012; Terrien et al. 2012). Moreover, all of these studies are based on a few features in the spectrum of photometry that might be degenerate with other parameters (e.g., gravity; Jao et al. 2008) or might not be measuring the real metallicity.

Age is a notoriously difficult property to measure for main-sequence stars as their properties do not evolve appreciably (Soderblom 2010). For M dwarfs, the problem is even more

[4]As to be expected of a system devised based on observed spectral features before the underlying properties were fully understood, spectral types are not always reflective of the physical processes inside the star. For example, the molecular lines start appearing at the K5–K7 spectral types while there is a overlap at the low-mass end as the youngest and brightest brown dwarfs have hot enough photospheres to be classified as late-M dwarfs.

acute. While techniques like asteroseismology (see review by Cunha et al. 2007), gyrochronology (Barnes 2003, 2007), and Ca II chromospheric emission have enabled age-dating of FGK stars, M dwarf ages are based solely on statistical methods. West et al. (2008) combined a dynamical heating model with empirical H$\alpha$-activity measurements to propose a new method dubbed Galactic stratigraphy. While its shows promise, it is yet to be calibrated for single stars and is only applicable to ensembles of stars.

Recently M dwarfs have also become the focus of planet search programs; the MEarth (Nutzman & Charbonneau 2008), PTF/M-dwarfs (Law et al. 2011), and CRIRES (Bean et al. 2010) programs are dedicated to detecting planets around M dwarfs. It is advantageous to search for planets around M dwarfs as (i) they are the most numerous stars in the Galaxy, (ii) their intrinsic faintness provides a higher planet–star contrast ratio, and (iii) their lower masses makes dynamical methods more sensitive to planets. In addition, early *Kepler* results have shown that M dwarfs seem to be much more likely to host small planets (2–4 $R_{\oplus}$) as compared to higher-mass F and G dwarfs (Howard et al. 2011), making M dwarfs the best bet to find earth-sized planets in the habitable zone. As exoplanet properties cannot be directly measured and are usually inferred from that of the host stars, it is imperative that we are able to measure the fundamental properties of the host stars to accurately characterize the detected exoplanets.

## 1.7 The Sloan Digital Sky Survey

One of the most ambitious and influential astronomical surveys, the Sloan Digital Sky Survey (SDSS; York et al. 2000) conducted imaging and spectroscopic observations of over 11,000 deg$^2$ in the Northern sky over the eight years of its operation (SDSS-I, 2000–2005; SDSS-II, 2005–2008). Using a wide-field, 2.5 m telescope and a 142 megapixel camera at the Apache Point Observatory, New Mexico, the imaging was carried out in drift-scan mode (Gunn et al. 1998) in five broad band filters—$u$, $g$,$r$, $i$, and $z$—spanning the range from 3000 Å to 10,000 Å (Fukugita et al. 1996). The effective exposure time per filter was 54.1 s, with 18.75 deg$^2$ imaged every hour in each of the five filters. From the photometric catalogs, targets for the spectroscopic survey were selected using various algorithms, consisting mainly of galaxies (Strauss et al. 2002; Eisenstein et al. 2001), quasars (Richards et al. 2002), and

stellar and calibration objects (Stoughton et al. 2002). Spectroscopy was conducted with a pair of multi-object double spectrographs fed by 640 optical fibers, each 3″ in diameter. The spectral coverage was from 3800 Å to 9200 Å at a resolution of $\lambda/\Delta\lambda \simeq 2000$. The exposures were each 15 minutes long, with three or more taken for a given plate to reach predefined requirements of signal-to-noise ratio (S/N): $(S/N)^2 > 15$ per 1.5 Å pixel for stellar objects of fiber magnitude $g = 20.2$, $r = 20.25$, and $i = 19.9$.

The seventh, and final, public data release (DR7) for the original SDSS project was in October 2008 (Abazajian et al. 2009). The photometric catalog had 357 million unique objects over 11,663 deg$^2$ while the spectroscopic catalog had over 1.6 million objects over 9380 deg$^2$. The photometry had calibration errors of 2% in $u$ and ∼1% in $griz$, with 95% completeness limits to 22.0, 22.2, 22.2, 21.3, and 20.5 mag and saturation at 12.0, 14.1, 14.1, 13.8, and 12.3 mag, respectively (Gunn et al. 1998). The astrometry was accurate to <0.″1 rms absolute per coordinate while the relative astrometry was accurate to <0.″05 rms per coordinate. The images were processed using specialized software (Lupton et al. 2001; Stoughton et al. 2002) and were astrometrically (Pier et al. 2003) and photometrically (Hogg et al. 2001; Tucker et al. 2006) calibrated using observations of a set of primary standard stars (Smith et al. 2002) observed on a neighboring 20 inch (51 cm) telescope.

More than any other large-scale surveys, SDSS transformed stellar astronomy by observing unprecedented numbers of M dwarfs. With a photometric catalog of more than 15 million (Bochanski et al. 2010) and a spectroscopic catalog of more than 70,000 (West et al. 2011) M dwarfs, SDSS has enabled studies of the spatial (Bochanski et al. 2010) and kinematic distributions (Bochanski et al. 2007b; Fuchs et al. 2009) in the Milky Way; the mass and luminosity functions (Covey et al. 2008; Bochanski et al. 2010); and magnetic activity (e.g., West et al. 2008, 2011; Kruse et al. 2010; Kowalski et al. 2009; Hilton et al. 2010) of low-mass stars. To put this into perspective, the previous largest spectroscopic sample of M dwarfs was the Palomar/Michigan State University Spectroscopic Survey of about 3000 nearby M dwarfs (Gizis et al. 2002; Hawley et al. 1996; Reid et al. 1995). SDSS has allowed for statistically robust studies of M dwarf and Galactic properties, even when the samples are subdivided by one or more parameters, including Galactic position, distance, spectral type, color, metallicity, and activity.

Table I.1. Comparison of modern, wide-field surveys

| | SDSS[a] | 2MASS[b] | UKIDSS[c] | Pan-STARRS[d] | VHS[e] | Skymapper[f] | WISE[g] | LSST[h] |
|---|---|---|---|---|---|---|---|---|
| Survey years | 2000–2008 | 1997–2001 | ··· | 2010–2013 | 2010–2017 | 2010-2015 | 2010 | 2018–2028 |
| Site | Apache Point, NM | Mt. Hopkins, AZ Cerro Tololo, Chile | Mauna Kea, HI | Haleakala, HI | Atacama, Chile | Siding Spring, NSW | Space | Cerra Pachon, Chile |
| Survey Area (deg$^2$) | 11,663 | 40,000 | 7000 | 30,000 | 19,000 | 22,000 | 40,000 | 20,000 |
| Aperture (m) | 2.5 | 1.3 | 3.8 | 4x1.8 | 4.1 | 1.35 | 0.4 | 8.4 |
| Field of view (deg$^2$) | 3 | ··· | ··· | 3 | 2.1 | 5.7 | 47′ | 9.6 |
| Pixel size (″) | 0.396 | 2 | 0.4 | 0.3 | 0.339 | 0.5 | 2.757 | 0.2 |
| Exposure time (s) | 53.9 | 6×1.3 | 40–80 | 30–60 | 180 | 110 | 11 | 2×15 |
| Number of epochs | 1[i] | 1[j] | 2 | 6 per filter | 1 | 6 per filter | 1 | 1000 |
| Filters | *ugriz* | $JHK_s$ | $ZYJHK$ | *grizy* | $JK$ ($ZYH$) | *uvgriz* | 3.4, 4.6, 12, 22 $\mu$m | *ugrizy* |
| $\lambda$ range ($\mu$m) | 0.3–1 | 1.25–2.16 | 0.83–2.37 | 0.5–1 | 0.88–2.15 | 0.3–1 | 3.5–23 | 0.32–1.05 |
| Faint limit (mag) | $r = 22.2$ | $K_s = 14.3$ | $K = 18.2$ | $r = 24$ (29.4)[k] | $J = 20.2$ | $r = 21.6$ (22.6)[k] | [3.4] = 16.5 | $r = 24.7$ (27.7)[k] |
| Photometry | 1% ($r$) | 5% | 2% | 1% | 2% | 3% | 1.1% | 1% |
| Astrometry (″) | <0.1 rms absolute | 0.1 rms | <0.1 rms | 0.07 | 0.1 | 0.05 | 0.15 rms | 0.03 absolute |

[a]The Sloan Digital Sky Survey (York et al. 2000)

[b]The Two Micron All Sky Survey (Skrutskie et al. 2006)

[c]The UKIRT Infrared Deep Sky Survey (Lawrence et al. 2007)

[d]The Panoramic Survey Telescope & Rapid Response System (Kaiser et al. 2010)

[e]The VISTA Hemisphere Survey (Arnaboldi et al. 2007)

[f]Keller et al. (2007)

[g]The Wide-field Infrared Survey Explorer (Wright et al. 2010)

[h]The Large Synoptic Survey Telescope (Ivezić et al. 2008a)

[i]Stripe 82, a 290 deg$^2$ area along the celestial equator, was observed multiple times, with the median field having ∼60 epochs (Ivezić et al. 2007).

[j]2MASS calibration field were observed repeatedly with sampling cadences of ∼1 min to 3.5 yr (Skrutskie et al. 2006).

[k]The number in the parenthesis refers to the faintness limit for the co-added images.

## 1.8 Summary

As discussed earlier in Section 1.1, the goals of this dissertation are to identify a large sample of ultra-wide binaries and use it to probe and put constraints on binary formation theories and fundamental properties of low-mass stars. We discuss the identification of 1342 wide pairs based on matching their proper motion components and heliocentric distances in Chapter II. Each of the pairs have a probability of chance alignment of <5% as quantified by comparing their 5D phase space parameters with a statistical Galactic model, built based on empirical stellar number density and space velocity distributions. This catalog, dubbed the Sloan Low-mass Wide Pairs of Kinematically Equivalent Stars (SLoWPoKES) was purposely rigorously sifted of false positives, even at the expense of identifying more genuine binary pairs, so as to allow for efficient followup observations.

In Chapter III, we report the discovery of a wide substellar binary: the M9+L6 binary 2MASS J01303563−4445411. While its physical separation is only ∼130 AU, its very low total mass ensures an extremely low binding energy and makes it a very fragile system. In fact, it is only one of six known VLM field binaries that are wider than 100 AU. According to current formation scenarios, 2MASS J01303563−4445411 is not supposed to exist, thus, it helps constrain formation theories. Moreover, as a system bracketing the regime where clouds in the atmosphere start to appear (late-M) and eventually condense (late-L), this is an important coeval laboratory.

In Chapter IV, we shift from using the SLoWPoKES wide binaries as probes of binary formation processes to using them as coeval laboratories. From followup spectroscopic data of 113 pairs, we find that the $\zeta_{\rm TiO/CaH}$ index—based on the CaH and TiO band heads in the optical spectrum LRS07—to be a good tracer of relative metallicity in early–mid M dwarfs. However, we found that $\zeta_{\rm TiO/CaH}$ overpredicts the relative metallicity of the higher-mass M dwarfs. We refined the definition assuming that the components of a binary are formed from the same material, making the redefined $\zeta_{\rm TiO/CaH}$ being a significantly better predictor of metallicity. The radial velocities and the $\zeta_{\rm TiO/CaH}$ values also underscore the fidelity of the SLoWPoKES catalog.

Chapter V summarizes our understanding of wide binary formation after the results from the SLoWPoKES catalog and talks about future experiments that need to be conducted to

further inform theoretical models. It also briefly described SLoWPoKES-II, the followup to the current catalog. We also briefly describe the current work that is being done based on the SLoWPoKES binaries as coeval laboratories and the future work that it has facilitated.

# CHAPTER II

## SLOAN LOW-MASS WIDE PAIRS OF KINEMATICALLY EQUIVALENT STARS (SLoWPoKES): A CATALOG OF ULTRA-WIDE, LOW-MASS PAIRS

The bulk of this chapter was published in the *The Astronomical Journal* as Dhital, West, Stassun, & Bochanski, (2010, 139:2566); the American Astronomical Society holds the copyright for the article.

This chapter presents the Sloan Low-mass Wide Pairs of Kinematically Equivalent Stars (SLoWPoKES) catalog of 1342 wide common proper motion binary systems. The SLoWPoKES catalog is was rigorously selected so as to comprise of only *bona fide* binary systems that could be efficiently used in followup programs as probes of binary formation and as coeval laboratory to study properties of low-mass stars. The algorithm used for he identification of the CPM pairs is discussed in detail. In essence, this chapter is the foundation of this dissertation and provides the sample that that is used in Chapter IV and other ongoing/future work. SLoWPoKES is the largest sample of wide binaries ever assembled.

The key science result presented in this chapter is the observed bimodality in the projected physical separation of wide binaries: (i) a tightly bound population of "wide" binaries and (ii) a loosely bound population of "ultra-wide" binaries based on the comparisons with dynamical dissipation calculations. This indicates that either different formation mechanisms might be producing the "wide" and "ultra-wide" binaries or sculpting by dynamical processes shapes the observed distribution of wide binaries.

The SLoWPoKES catalog and future ancillary data are publicly available on the world wide web for utilization by the astronomy community.

## 2.1 Introduction

The formation and evolution of binary stars remains one of the key unanswered questions in stellar astronomy. As most stars are thought to form in multiple systems, and with the possibility that binaries may host exoplanet systems, these questions are of even more importance. While accurate measurements of the fundamental properties of binary systems provide constraints on evolutionary models (e.g., Stassun et al. 2007), knowing the binary frequency, as well as the distribution of the periods, separations, mass ratios, and eccentricities of a large ensemble of binary systems are critical to understanding binary formation (Goodwin et al. 2007, and references therein). To date, multiplicity has been most extensively studied for the relatively bright high- and solar-mass local field populations (e.g., DM91). Similar studies of low-mass M and L dwarfs have been limited by the lack of statistically significant samples due to their intrinsic faintness. However, M dwarfs constitute ∼70% of Milky Way's stellar population (Miller & Scalo 1979; Henry et al. 1999; Reid et al. 2002; Bochanski et al. 2010) and significantly influence its properties.

Since the pioneering study of Heintz (1969), binarity has been observed to decrease as a function of mass: the fraction of primaries with companions drops from 75% for OB stars in clusters (Gies 1987; Mason et al. 1998, 2009) to ∼60% for solar-mass stars (Abt & Levy 1976, DM91, Halbwachs et al. 2003) to ∼30–40% for M dwarfs (Fischer & Marcy 1992; Henry & McCarthy 1993; Reid & Gizis 1997; Delfosse et al. 2004) to ∼15% for brown dwarfs (BDs; Bouy et al. 2003; Close et al. 2003; Gizis et al. 2003; Martín et al. 2003). This decrease in binarity with mass is probably a result of preferential destruction of lower binding energy systems over time by dynamical interactions with other stars and molecular clouds, rather than a true representation of the multiplicity at birth (Goodwin & Kroupa 2005). In addition to having a smaller total mass, lower-mass stars have longer main-sequence lifetimes (Laughlin, Bodenheimer, & Adams 1997) and, as an ensemble, have lived longer and been more affected by dynamical interactions. Hence, they are more susceptible to disruption over their lifetime. Studies of young stellar populations (e.g., in Taurus, Ophiucus, Chameleon) appear to support this argument, as their multiplicity is twice as high as that in the field (Leinert et al. 1993; Ghez et al. 1997; Kohler & Leinert 1998). However, in denser star-forming regions in the Orion Nebula Cluster and IC 348, where more dynamical interactions

are expected, the multiplicity is comparable to the field (Simon, Close, & Beck 1999; Petr et al. 1998; Duchêne, Bouvier, & Simon 1999). Hence, preferential destruction is likely to play an important role in the evolution of binary systems.

DM91 found that the physical separation of the binaries could be described by a log-normal distribution, with the peak at $a$ ∼30 AU and $\sigma_{\log a}$ ∼1.5 for F and G dwarfs in the local neighborhood. The M dwarfs in the local 20-pc sample of Fischer & Marcy (1992) seem to follow a similar distribution with a peak at $a$ ∼3–30 AU, a result severely limited by the small number of binaries in the sample.

Importantly, both of these results suggest the existence of very wide systems, separated in some cases by more than a parsec. Among the nearby ($d < 100$ pc) solar-type stars in the *Hipparcos* catalog, Lépine & Bongiorno (2007) found that 9.5% have companions with projected orbital separations $s > 1000$ AU. However, we do not have a firm handle on the widest binary that can be formed or on how they are affected by localized Galactic potentials as they traverse the Galaxy. Hence, a sample of wide binaries, especially one that spans a large range of heliocentric distances, would help in (i) putting empirical constraints on the widest binary systems in the field (e.g., Reid et al. 2001b; Burgasser et al. 2003b, 2007c; Close et al. 2003, 2007), (ii) understanding the evolution of wide binaries over time (e.g., Weinberg, Shapiro, & Wasserman 1987; Jiang & Tremaine 2010), and (iii) tracing the inhomogeneities in the Galactic potential (e.g., Bahcall, Hut, & Tremaine 1985 Weinberg et al. 1987; Yoo, Chanamé, & Gould 2004; Quinn et al. 2009).

Recent large scale surveys, such as SDSS (York et al. 2000), 2MASS (Cutri et al. 2003), and UKIDSS (Lawrence et al. 2007), have yielded samples of unprecedented numbers of low-mass stars. SDSS alone has a photometric catalog of more than 30 million low-mass dwarfs (Bochanski et al. 2010), defined as mid-K–late-M dwarfs, and a spectroscopic catalog of more than 44000 M dwarfs (West et al. 2008). The large astrometric and photometric catalogs of low-mass stars afford us the opportunity to explore anew the binary properties of the most numerous constituents of Milky Way, particularly at the very widest binary separations.

The orbital periods of very wide binaries (orbital separation $a > 100$ AU) are much longer than the human timescale ($P = 1000$ yr for $M_{tot} = 1$ $M_\odot$ and $a = 100$ AU). Thus, these systems can only be identified astrometrically, accompanied by proper motion or radial

velocity matching. These also remain some of the most under-explored low-mass systems. Without the benefit of retracing the binary orbit, two methods have been historically used to identify very wide pairs:

1. Bahcall & Soneira (1981) used the two-point correlation method to argue that the excess of pairs found at small separations is a signature of physically associated pairs; binarity of some of these systems was later confirmed by radial velocity observations (Latham et al. 1984). See Garnavich (1988) and Wasserman & Weinberg (1991) for other studies that use this method.

2. To reduce the number of false positives inherent in the above, one can use additional information such as proper motions. Orbital motions for wide systems are small; hence, the space velocities of a gravitationally bound pair should be the same, within some uncertainty. In the absence of radial velocities, which are very hard to obtain for a very large number of field stars, proper motion alone can be used to identify binary systems; the resulting pairs are known as CPM doubles. Luyten (1979a, 1988) pioneered this technique in his surveys of Schmidt telescope plates using a blink microscope and detected more than 6000 wide CPM doubles with $\mu$ >100 mas yr$^{-1}$ over almost fifty years. This method has since been used to find CPM doubles in the AGK 3 stars by Halbwachs (1986), in the revised New Luyten Two-Tenths (rNLTT; Salim & Gould 2003) catalog by Chanamé & Gould (2004), and among the *Hipparcos* stars in the Lepine-Shara Proper Motion-North (LSPM-N; Lépine & Shara 2005) catalog by Lépine & Bongiorno (2007). All of these studies use magnitude-limited high proper-motion catalogs and, thus, select mostly nearby stars.

More recently, Sesar, Ivezić, & Jurić (2008) searched the SDSS Data Release Six (DR6; Adelman-McCarthy et al. 2008) for CPM binaries with angular separations up to 30″ using a novel statistical technique that minimizes the difference between the distance moduli obtained from photometric parallax relations for candidate pairs. They matched proper motion components to within 5 mas yr$^{-1}$ and identified ∼22000 total candidates with excellent completeness, but with a one-third of them expected to be false positives. They searched the SDSS DR6 catalog for pairs at all mass ranges and find pairs separated by 2000–47000 AU,

at distances up to 4 kpc. Similarly, Longhitano & Binggeli (2010) used the angular two-point correlation function to do a purely statistical study of wide binaries in the $\sim$675 deg$^2$ centered at the North Galactic Pole using the DR6 stellar catalog and predicted that there are more than 800 binaries with physical separations larger than 0.1 pc but smaller than 0.8 pc. As evidenced by the large false positive rate in Sesar et al. (2008), such large-scale searches for wide binaries generally involve a trade-off between completeness on the one hand and fidelity on the other, as they depend on statistical arguments for identification.

Complementing this type of ensemble approach, a high-fidelity approach may suffer from incompleteness and/or biases; however, there are a number of advantages to a "pure" sample of *bona fide* wide binaries such as that presented in this work. For example, Faherty et al. (2010) searched for CPM companions around the brown dwarfs in the BDKP catalog (Faherty et al. 2009) and found nine nearby pairs; all of their pairs were followed up spectroscopically and, hence, have a much higher probability of being real. As mass, age, and metallicity can all cause variations in the observed physical properties, e.g., in radius or in magnetic activity, their effects can be very hard to disentangle in a study of single stars. Components of multiple systems are expected to have been formed of the same material at the same time, within a few hundred thousand years of each other (e.g., White & Ghez 2001; Goodwin, Whitworth, & Ward-Thompson 2004a; Stassun et al. 2008). Hence, binaries are perfect tools for separating the effects of mass, age, and metallicity from each other as well as for constraining theoretical models of stellar evolution. Some examples include benchmarking stellar evolutionary tracks (e.g.,White et al. 1999; Stassun, Mathieu, & Valenti 2007; Stassun et al. 2008), investigating the age-activity relations of M dwarfs (e.g., Silvestri, Hawley, & Oswalt 2005), defining the dwarf-subdwarf boundary for spectral classification (e.g., LRS07), and calibrating the metallicity indices (Woolf & Wallerstein 2005; Bonfils et al. 2005). Moreover, equal-mass multiples can be selected to provide identical twins with the same initial conditions (same mass, age, and metallicity) to explore the intrinsic variations of stellar properties. In addition, binaries with physical separations, or $a$, larger than $\sim$100 AU are expected to evolve independently of each other; even their disks are unaffected by the distant companion (Clarke 1992). Components of such systems are effectively two single stars that share their formation and evolutionary history. In essence

they can be looked at as *coeval laboratories* that can be used to effectively test and calibrate relations measured for field stars. Finally, as interest has grown in detecting exoplanets and in characterizing the variety of stellar environments in which they form and evolve, a large sample of *bona fide* wide binaries could provide a rich exoplanet hunting ground for future missions such as the *Space Interferometry Mission* (Unwin et al. 2008)

In this chapter, we present a new catalog of CPM doubles from SDSS, each with at least one low-mass component, identified by matching proper motions and photometric distances. In Section 2.2 we describe the origin of the input sample of low-mass stars; Section 2.3 details the binary selection algorithm and the construction of a Galactic model built to assess the fidelity of each binary in our sample. The resulting catalog and its characteristics are discussed in Section 2.4. We compare the result of our CPM double search with previous studies in Section 2.5 and summarize our conclusions in Section 2.6.

## 2.2 SDSS Data

### 2.2.1 SDSS Sample of Low-Mass Stars

SDSS is a comprehensive imaging and spectroscopic survey of the northern sky using five broad optical bands (*ugriz*) between ∼3000–10000 Å using a dedicated 2.5 m telescope (York et al. 2000; Fukugita et al. 1996; Gunn et al. 1998). Data Release Seven (DR7; Abazajian et al. 2009) contains photometry of 357 million unique objects over 11663 deg$^2$ of the sky and spectra of over 1.6 million objects over 9380 deg$^2$ of the sky. The photometry has calibration errors of 2% in $u$ and ∼1% in *griz*, with completeness limits of 95% down to magnitudes 22.0, 22.2, 22.2, 21.3, 20.5 and saturation at magnitudes 12.0, 14.1, 14.1, 13.8, 12.3, respectively (Gunn et al. 1998). We restricted our sample to $r \leq 20$ where the SDSS/USNO-B proper motions are more reliable (see Section 2.2.3); hence, photometric quality and completeness should be excellent for our sample.

Stellar sources with angular separations $\gtrsim 0.5$–$0.7''$ are resolved in SDSS photometry; we determined this empirically from a search in the NEIGHBORS table. For sources brighter than $r \sim 20$, the astrometric accuracy is 45 mas rms per coordinate while the relative astrometry between filters is accurate to 25–35 mas rms (Pier et al. 2003).

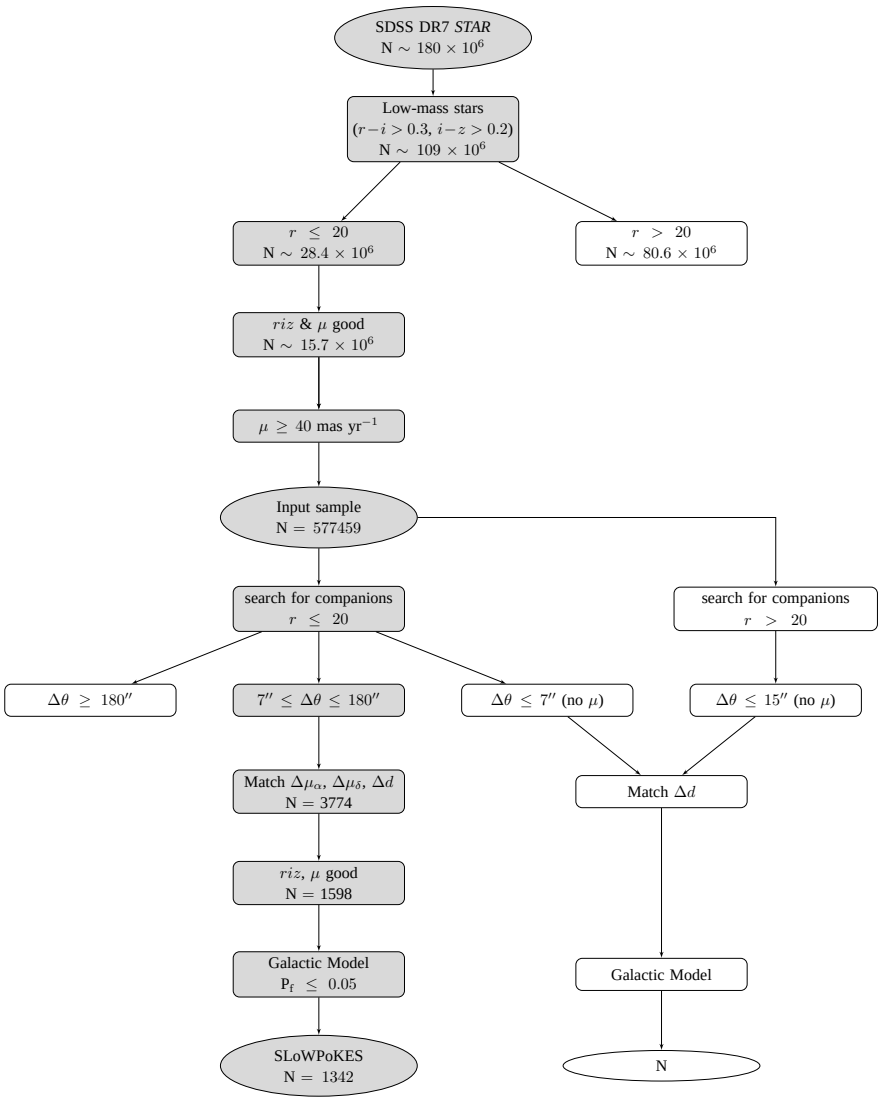


Figure 2.1: A graphical representation of the selection process used in the identification of SLoWPoKES pairs. The gray boxes show the steps involved in SLoWPoKES, with the results presented in this chapter. The pairs without proper motions (shown in white boxes) will be discussed in the future as part of SLoWPoKES-II.

The SDSS DR7 photometric database has more than 180 million stellar sources (Abazajian et al. 2009); to select a sample of low-mass stars, we followed the procedures outlined in Bochanski et al. (2010) and required $r - i \geq 0.3$ and $i - z \geq 0.2$, which represents the locus of sample K5 or later dwarfs. The STAR table was used to ensure that all of the selected objects had morphology consistent with being point sources (TYPE = 6) and were not

duplicate detections of the same source (PRIMARY)[1]. This yielded a sample of > 109 million low-mass stars with $r \sim 14$–24, at distances of ∼0.01–5 kpc from the Sun. Figure 2.1 shows a graphical flow chart of the selection process and criteria used; the steps needed in identifying kinematic companions, which are detailed in this chapter, are shown in gray boxes. The white boxes show subsets where kinematic information is not available; however, it is still possible to identify binary companions based on their close proximity. We will discuss the selection of those binaries, without available kinematic information, in the future as part of SLoWPoKES-II.

### 2.2.2 Proper Motions

The SDSS/USNO-B matched catalog (Munn et al. 2004), which is integrated into the SDSS database in the PROPERMOTIONS table, was used to obtain proper motions for this study. We used the proper motions from the DR7 catalog; the earlier data releases had a systematic error in the calculation of proper motion in right ascension (see Munn et al. 2008, for details). This catalog uses SDSS galaxies to recalibrate the USNO-B positions and USNO-B stellar astrometry as an additional epoch for improved proper motion measurements. The PROPERMOTIONS catalog is resolution limited in the USNO-B observations to 7″ and is 90% complete to $g = 19.7$[2], corresponding to the faintness limit of the POSS-II plates used in USNO-B. The completeness also drops with increasing proper motion; for the range of proper motions in our sample ($\mu$ = 40–350 mas yr$^{-1}$; see Section 2.2.3 below), the completeness is ∼ 85%. The typical 1 $\sigma$ error is 2.5–5 mas yr$^{-1}$ for each component

### 2.2.3 Quality Cuts

To ensure that the resultant sample of binaries is not contaminated due to bad or suspect data, we made a series of cuts on the stellar photometry and proper motions. With > 109 million low-mass stars, we could afford to be very conservative in our quality cuts and still have a reasonable number of stars in our input sample. We restricted our sample, as shown

[1]We note that binaries separated by less than ∼1″ might appear elongated in SDSS photometry and might not be listed in the STAR table.

[2]This corresponds to $r = 18.75$ for K5 and $r = 18.13$ for M6 dwarfs.

in Figure 2.1, to stars brighter than $r = 20$ and made a cut on the standard quality flags on the $riz$ magnitudes (PEAKCENTER, NOTCHECKED, PSF_FLUX_INTERP, INTERP_CENTER, BAD_COUNTS_ERROR, SATURATED – all of which are required to be 0)[3], which are the only bands pertinent to low-mass stars and the only bands used in our analysis.

On the proper motions, Munn et al. (2004) recommended a minimum total proper motion of 20 mas yr$^{-1}$ and cuts based on different flags for a "clean" and reliable sample of stellar sources. Therefore, we required that each star (i) matched an unique USNO-B source within $1''$ (MATCH $> 0$), (ii) had no other SDSS source brighter than $g = 22$ within $7''$ (DIST22 $> 7$), (iii) was detected on at least 4 of the 5 USNO-B plates and in SDSS (NFIT $= 6$ or (NFIT $= 5$ and ($O < 2$ or $J < 2$))), (iv) had a good least-squares fit to its proper motion (SIGRA $< 1000$ and SIGDEC $< 1000$), and (v) had 1 $\sigma$ error for both components less than 10 mas yr$^{-1}$.

A challenge inherent in using a deep survey like SDSS to identify CPM binaries, is that most of the stars are far away and, therefore, have small proper motions. To avoid confusing real binaries with chance alignments of stars at large distances, where proper motions are similar but small, a minimum proper motion cut needs to be applied. Figure 2.2 shows the distribution of candidate binaries (selected as detailed in Section 2.3.1) with minimum proper motion cuts of 20, 30, 40, and 50 mas yr$^{-1}$; the histograms have been normalized by the area of the histogram with the largest area to allow for relative comparisons. All four distributions have a peak at small separations of mostly real binaries, but the proportion of chance alignments at wider separations becomes larger and more dominant at smaller $\mu$ cutoffs.

If our aim were to identify a complete a sample of binaries, we might have chosen a low $\mu$ cutoff and accepted a relatively high contamination of false pairs. Such was the approach in the recent study of SDSS binaries by Sesar et al. (2008) who used $\mu \geq 15$ mas yr$^{-1}$. Our aim, in this chapter, was to produce a "pure" sample with a high yield of *bona fide* binaries. Thus, in our search for CPM pairs we adopted a minimum proper motion of $\mu = 40$ mas yr$^{-1}$ for our low-mass stellar sample since the number of matched pairs clearly declines with increasing $\Delta\theta$ with this cutoff (Figure 2.2). While this still allows for a number of (most likely) chance

[3]A PRIMARY object is already selected to not be BRIGHT and NODEBLEND or DEBLEND_NOPEAK

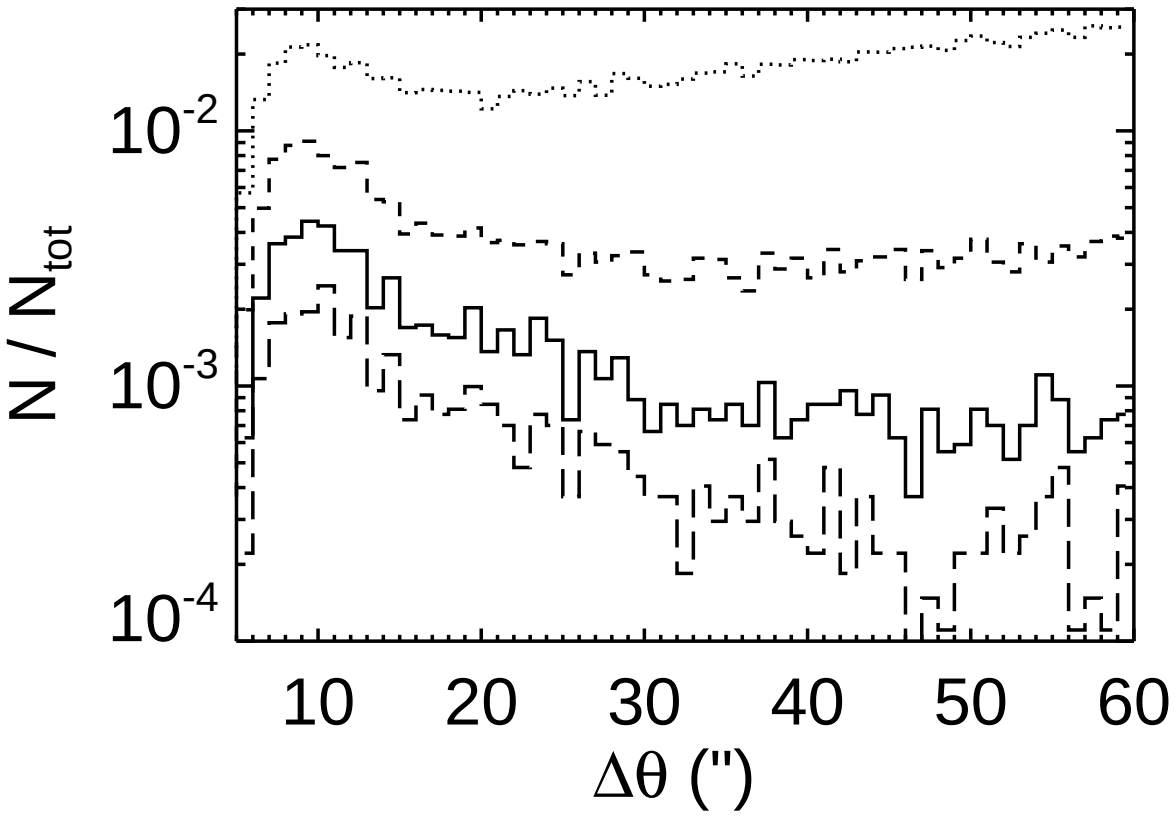


Figure 2.2: The angular separation distribution of candidate pairs with minimum proper motions cut-offs of 20 (dotted), 30 (dashed), 40 (solid), and 50 (long dashes) mas yr$^{-1}$. These candidates were selected by matching angular separations, proper motions, and photometric distances as described in Section 2.3.1. All histograms have been normalized by the area of the histogram with the largest area to allow for relative comparisons. It can be clearly deduced that a low proper motion cut-off will cause a large proportion of chance alignments. We adopted a cut-off of $\mu \geq 40$ mas yr$^{-1}$ as it allows for identification of CPM pairs with a reasonable number of false positives that are later sifted with our Galactic model.

alignments, they do not dominate the sample and can be sifted more effectively as discussed below.

Thus, on the $\sim$15.7 million low-mass stars that satisfied the quality cuts, we further imposed a $\mu \geq 40$ mas yr$^{-1}$ cut on the total proper motion that limits the input sample to 577,459 stars with excellent photometry and proper motions. As Figure 2.1 shows, this input sample constitutes all the stars around which we searched for companions. Figure 2.3 shows the distributions of photometric distances, total proper motions, $r - i$ vs. $i - z$ color-color

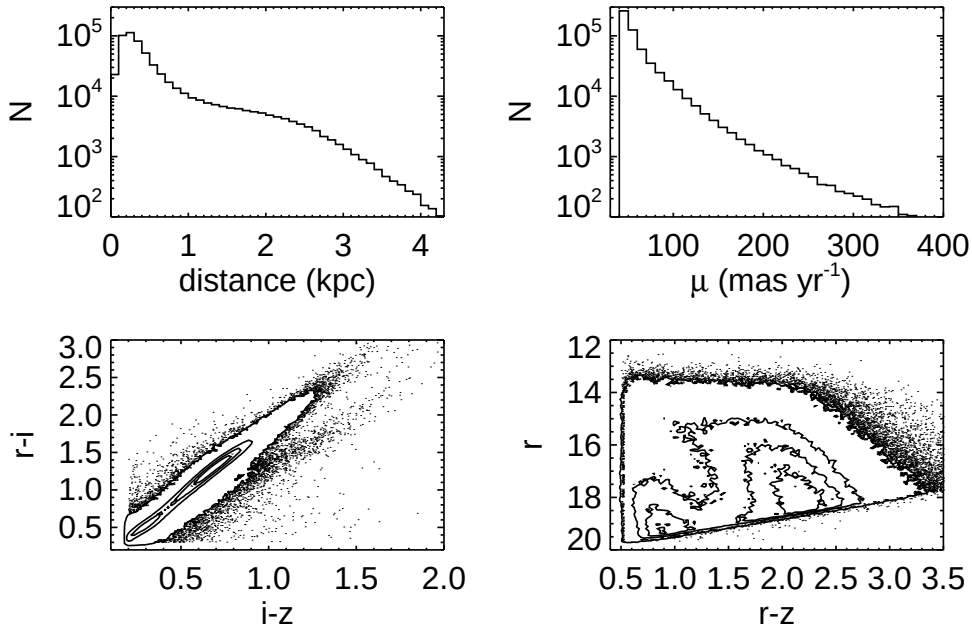


Figure 2.3: The characteristics of the sample of 577,459 low-mass stars in the SDSS DR7 photometric catalog that forms our input sample *(clockwise from top left)*: the photometric distances, the total proper motions, $r$ vs. $r-z$ Hess diagram, and the $r-i$ vs. $i-z$ color–color plot. In addition to quality cuts on proper motion and photometry, we require that stars in this sample to be low-mass ($r-i \geq 0.3$ and $i-z \geq 0.2$) and have a relatively high proper motion ($\mu \geq 40$ mas yr$^{-1}$). The contours show densities of 10–3000 in the color–color plot and 10–300 in the Hess diagram.

diagram, and the $r$ vs. $r-z$ Hess diagram for the input sample. As seen from their $r-z$ colors in the Hess diagram, the sample consists of K5–L0 dwarfs. Metal-poor halo subdwarfs are also clearly segregated from the disk dwarf population; however, due to a combination of the magnitude and color limits that were used, they are also mostly K subdwarfs and are limited to only the earliest spectral types we probe.

### 2.2.4 Derived properties

#### 2.2.4.1 Photometric Distances

**Disk dwarfs (DD)**: We determined the distances to the DDs in our sample by using photometric parallax relations, measured empirically with the SDSS stars. For M and L dwarfs (∼M0–L0; $0.94 < r-z < 4.34$), we used the relation derived by Bochanski et al.

Table II.1. Coefficients for $M_r(r-z)$, SpT$(r-z)$, and M$(r-z)$

| $a_N$ | $M_r(r-z)$ | | SpT$(r-z)$ | | M$(r-z)$ | |
|---|---|---|---|---|---|---|
| | O5-K9[a] | M0-L0[b] | O5-K5[c] | K5-L0[d] | O5-K5[e] | K5-L0[e] |
| $a_0$ | 5.190 | 3.144 | 50.40 | 33.60 | 1.210 | 0.640 |
| $a_1$ | 2.474 | 7.541 | 9.040 | 47.80 | −1.120 | 0.362 |
| $a_2$ | 0.434 | −3.225 | −2.970 | −20.10 | 1.060 | −0.5390 |
| $a_3$ | −0.086 | 0.576 | 0.5160 | −33.70 | −2.730 | 0.1700 |
| $a_4$ | ··· | ··· | −0.0280 | −58.10 | 2.970 | −58.20 |

[a]Fit based on data from Covey et al. (2007)

[b]Bochanski et al. (2010)

[c]Fit based on data from Covey et al. (2007)

[d]Fit based on data from Bochanski et al. (2010)

[e]Fit based on data from Kraus & Hillenbrand (2007)

(2010) based on data from D. Golimowski et al. (*in preparation*). For higher mass dwarfs (∼O5–K9; $-0.72 < r-z < 0.94$), we fit a third-order polynomial to the data reported in Covey et al. (2007):

$$M_r = \sum_N (r-z)^N \tag{2.1}$$

where the coefficients, $a_N$, are tabulated in Table II.1.

In both of the above relations, we used extinction-corrected magnitudes. Ideally, $M_r$ would have been a function of both color and metallicity; but the effect of metallicity is not quantitatively known for low-mass stars. This effect, along with unresolved binaries and the intrinsic width of the main-sequence, cause a non-Gaussian scatter of $\sim$ 0.3–0.4 magnitudes in the photometric parallax relations (West, Walkowicz, & Hawley 2005; Sesar et al. 2008; Bochanski et al. (2010)). Since we are matching the photometric distances, using the smaller error bars ensures fewer false matches. Hence, we adopted 0.3 magnitudes as our error, implying a 1 $\sigma$ error of ∼14% in the calculated photometric distances.

**Subdwarfs (SD)**: Reliable photometric distance relations are not available for SDs, so instead we used the relations for DDs above. As a result of appearing under-luminous at a given color, their absolute distances will be overestimated. However, the *relative* distance between two stars in a physical binary should have a small uncertainty. Because we are in-

terested in determining if two candidate stars occupy the same volume in space, the relative distances will suffice. While photometric parallax relations based on a few stars of a range of metallicities (Reid 1998; Reid et al. 2001c) or calibrated for solar-type stars (Ivezić et al. 2008b) do exist and can provide approximate distances for low-mass SDs, we refrained from using them due to the large uncertainties involved.

**White dwarfs (WD)**: We calculated the photometric distances to WDs using the algorithm used by Harris et al. (2006): *ugriz* magnitudes and the $u-g$, $g-r$, $r-i$, and $i-z$ colors, corrected for extinction, were fitted to the WD cooling models of Bergeron, Wesemael, & Beauchamp (1995) to get the bolometric luminosities and, hence, the distances[4]. The bolometric luminosity of WDs are a function of gravity as well as the composition of its atmosphere (hydrogen/helium), neither of which can be determined from the photometry. Therefore, we assumed pure hydrogen atmospheres with $\log\ g = 8.0$ to calculate the distances to the WDs. As a result, distances derived for WDs with unusually low mass and gravity (∼10% of all WDs) or with unusually high mass and gravity (∼15% of all WDs) will have larger uncertainties. Helium WDs redder than $g-i > 0.3$ will also have discrepant distances (Harris et al. 2006).

#### 2.2.4.2 Spectral Type & Mass

The spectral type of all (O5–M9; $-0.6 \leq r-z \leq 4.5$) disk dwarfs and subdwarfs were inferred from their $r-z$ colors using the following two-part fourth-order polynomial, with a break at the spectral type of K5:

$$\mathrm{SpT} = \sum_N a_N (r-z)^N \tag{2.2}$$

where the coefficients, $a_N$, are tabulated in Table II.1. The SpT ranges from 0–67 (O0=0 and M9=67 with all spectral types, except K for which K6, K8, and K9 are not defined, having 10 subtypes) and is based on the data reported in Covey et al. (2007) and West et al.

[4]SDSS *ugriz* magnitudes and colors for the WD cooling models are available on P. Bergeron's website: `http://www.astro.umontreal.ca/~bergeron/CoolingModels/`

(2008). The spectral types should be correct to ±1 subtype.

Similarly, the mass of B8–M9 disk dwarfs and subdwarfs were determined from their $r-z$ colors using a two-part fourth-order polynomial, with a break at the spectral type of K5:

$$M(M_{\odot}) = \sum_{N} a_N (r-z)^N \tag{2.3}$$

where the coefficients, $a_N$, are tabulated in Table II.1. The fit is based on the data reported in Kraus & Hillenbrand (2007), who used theoretical models, supplemented with observational constrains when needed, to get mass as a function of spectral type. The scatter of the fit, as defined by the median absolute deviation, is ∼2%.

As the polynomials for both the spectral type and mass are monotonic functions of $r-z$ over the entire range, the component with the bluer $r-z$ color was classified as the primary star of each binary found.

## 2.3 Method

### 2.3.1 Binary Selection

Components of a gravitationally bound system are expected to occupy the same spatial volume, described by their semi-axes, and to move with a common space velocity. To identify physical binaries in our low-mass sample, we implemented a statistical matching of positional astrometry (right ascension, $\alpha$, and declination, $\delta$), proper motion components ($\mu_\alpha$ and $\mu_\delta$), and photometric distances ($d$). The matching of distances is an improvement to the methods of previous searches for CPM doubles (Lépine & Bongiorno 2007; Chanamé & Gould 2004; Halbwachs 1986) and serves to provide further confidence in the binarity of identified systems.

The angular separation, $\Delta\theta$, between two nearby point sources, A and B, on the sky can be calculated using the small angle approximation:

$$\Delta\theta \simeq \sqrt{(\alpha_A - \alpha_B)^2 \cos\delta_A \cos\delta_B + (\delta_A - \delta_B)^2}. \tag{2.4}$$

We searched around each star in the input sample for all stellar neighbors, brighter than $r = 20$ and with good photometry and proper motions, within $\Delta\theta \leq 180''$ in the SDSS

photometric database using the Catalog Archive Server query tool[5]. Although CPM binaries have been found at much larger angular separations (up to 900″ in Chanamé & Gould 2004; 1500″ in Lépine & Bongiorno 2007; 570″ in Faherty et al. 2010), the contamination rate of chance alignments at such large angular separations was unacceptably high in the deep SDSS imaging (see Figure 2.2). In addition, searching the large number of matches at larger separations required large computational resources. However, since the SDSS low-mass star sample spans considerably larger distances than in previous studies (see below), our cutoff of 180″ angular separation probes similar *physical separations* of up to ∼0.5 pc, which is comparable to the typical size of prestellar cores (0.35 pc; Benson & Myers 1989; Clemens, Yun, & Heyer 1991; Jessop & Ward-Thompson 2000).

For all pairs that were found with angular separations of $7'' \leq \Delta\theta \leq 180''$, we required the photometric distances to be within

$$\Delta d \leq (1\ \sigma_{\Delta d}, 100\ \mathrm{pc}) \tag{2.5}$$

and the proper motions to be within

$$\left(\frac{\Delta\mu_\alpha}{\sigma_{\Delta\mu_\alpha}}\right)^2 + \left(\frac{\Delta\mu_\delta}{\sigma_{\Delta\mu_\delta}}\right)^2 \leq 2 \tag{2.6}$$

where $\Delta d$, $\Delta\mu_\alpha$, and $\Delta\mu_\delta$ are the scalar differences between the two components with their uncertainties calculated by adding the individual uncertainties in quadrature. An absolute upper limit on $\Delta d$ of 100 pc was imposed to avoid $\Delta d$ being arbitrarily large at the very large distances probed by SDSS; hence, at $d \gtrsim 720$ pc, distances are matched to be within 100 pc and results in a significantly lower number of candidate pairs. The proper motions are matched in 2-dimensional vector space, instead of just matching the total (scalar) proper motion as has been frequently done in the past. The latter approach allows for a significant number of false positives as stars with proper motions with the same magnitude but different directions can be misidentified as CPM pairs.

For our sample, the uncertainties in proper motions are almost always larger than the

[5] `http://casjobs.sdss.org/CasJobs/`

largest possible Keplerian orbital motions of the identified pairs. For example, a binary with a separation of 5000 AU and $M_{tot} = 1\ M_{\odot}$ at 200 pc, which is a typical pair in the resultant SLoWPoKES sample, will has a maximum orbital motion of $\sim$0.45 mas yr$^{-1}$, much smaller than error in our proper motions (typically 2.5–5 mas yr$^{-1}$). However, a pair with a separation of 500 AU pair and $M_{tot} = 1\ M_{\odot}$ at 50 pc has a maximum orbital motion of $\sim$5.62 mas yr$^{-1}$, comparable to the largest errors in component proper motions. Hence, our algorithm will reject such nearby, relatively tight binaries.

From the mass estimates and the angular separations from the resulting sample, we calculated the maximum Keplerian orbital velocities, which are typically less than 1 mas yr$^{-1}$; only 104, 34, and 3 out of a total of 1342 systems exceeded 1, 2, and 5 mas yr$^{-1}$, respectively. More importantly, only 7 pairs had maximum orbital velocities greater than 1-$\sigma$ error in the proper motion; so apart from the nearest and/or tightest pairs, our search should not have been affected by our restrictions on the proper motion matching in Eq. (2.6).

Applying these selection criteria to the stellar sample described in Section 2.2.1, we found a total of 3774 wide CPM binary candidates, where each has at least one low-mass component. Among these, we found 118 pairs shown in red pluses and dashed histograms in Figure 2.4, concentrated in a $20' \times 150'$ stripe, in the direction of open cluster IC 5146.As there is significant nebulosity that is not reflected in the extinction values, the photometry and, hence, the calculated photometric distances are not reliable. In addition, while the kinematics are not characteristic of IC 5146, they are more likely to be part of a moving group rather than individual CPM pairs. Thus, we rejected all of these candidates. No other distinct structures, in space and kinematics, were found. Then, we made the quality cuts described in Section 2.2.3 on the companions; 906 and 1085 companions did not meet our threshold for the photometry and proper motions, respectively, and were rejected. The majority of these rejections were near the Galactic Plane, which was expected due to higher stellar density. Thus, at the end, the resulting sample had 1598 CPM double candidates from the statistical matching (Figure 2.1). Inherent in statistical samples are false positives, arising from chance alignments within the uncertainties of the selection criteria. For any star, the probability of chance alignment grows with the separation making the wider companions much more likely to be chance alignments despite the selection criteria we just implemented.

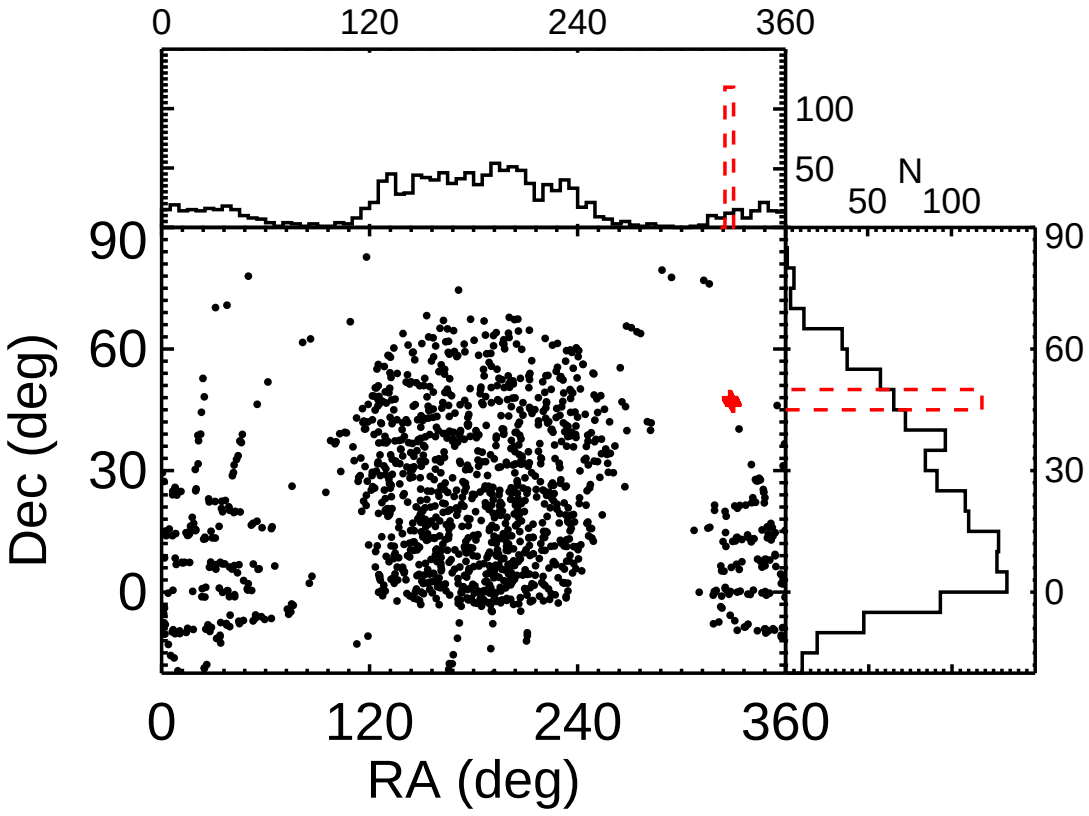


Figure 2.4: The spatial distribution of SLoWPoKES binaries, shown in equatorial coordinates, closely follows the SDSS footprint. The upper and right panels show the histogram of Right Ascension and Declination in 5° bins. We rejected the 118 CPM candidates found in the direction of open cluster IC 5146 (shown in red pluses and dashed histograms) due to the highly anomalous concentration of pairs and possibly contaminated photometry due to nebulosity (see Section 2.3.1).

Hence, it is necessary to complete a detailed analysis of the fidelity of the sample.

### 2.3.2 Galactic Model: Assessing False Positives in the Binary Sample

To quantitatively assess the fidelity of each binary in our sample, we created a Monte Carlo based Galactic model that mimics the spatial and kinematic stellar distributions of the Milky Way and calculates the likelihood that a given binary could arise by chance from a random alignment of stars. Clearly, for this to work the underlying distribution needs to be carefully constructed such that, as an ensemble, it reflects the statistical properties of the true

distribution. The model needs to take into account the changes in the Galactic stellar density and space velocity over the large range of galactocentric distances and heights above/below the Galactic disk plane probed by our sample. Previous studies, focused on nearby binaries, have been able to treat the underlying Galactic stellar distribution as a simple random distribution in two-dimensional space. For example, Lépine & Bongiorno (2007) assigned a random shift of 1–5° in Right Ascension for the secondary of their candidate pairs and compared the resultant distribution with the real one. As they noted, the shift cannot be arbitrarily large and needs to be within regions of the sky with similar densities and proper motion systematics. With stars at much larger heliocentric distances in our sample, even a 1° shift would correspond to a large shift in Galactic position (1° in the sky at 1000 pc represents ∼17.5 pc). Therefore, we could not use a similar approach to assess the false positives in our catalog.

The Galactic model is built on the canonical view that the Galaxy comprises three distinct components—the thin disk, the thick disk, and the halo—that can be cleanly segregated by their age, metallicity, and kinematics (Bahcall & Soneira 1980b; Gilmore, Wyse, & Kuijken 1989; Majewski 1993). We note that some recent work has argued for the disk to be a continuum instead of two distinct components (Ivezić et al. 2008b) or for the halo to be composed of two distinct components (Carollo et al. 2008, 2010). However, for our purposes, the canonical three-component model was sufficient. We also did not try to model the over-densities or under-densities, in positional or kinematic space, caused by co-moving groups, open clusters, star-forming regions, or Galactic streams. If such substructures were found in the SDSS data, they were removed from our sample (see Section 2.3.1). In essence, this model strictly describes stars in the field and produces the three-dimensional position and two-dimensional proper motion, analogous to what is available for the SDSS photometric catalog.

#### 2.3.2.1 Galactic stellar density profile

In the canonical Galactic model, the stellar densities ($\rho$) of the thin and the thick disks, in standard Galactic coordinates $R$ (Galactic radius) and $Z$ (Galactic height), are given by

$$\rho_{\rm thin}(R,Z) = \rho\ (R_\odot, 0)\ e^{-\frac{|Z|}{H_{\rm thin}}}\ e^{-\frac{|R-R_\odot|}{L_{\rm thin}}} \tag{2.7}$$

$$\rho_{\rm thick}(R,Z) = \rho\ (R_\odot, 0)\ e^{-\frac{|Z|}{H_{\rm thick}}}\ e^{-\frac{|R-R_\odot|}{L_{\rm thick}}}, \tag{2.8}$$

where $H$ and $L$ represent the scale height above (and below) the plane and the scale length within the plane, respectively. The halo is described by a bi-axial power-law ellipsoid

$$\rho_{\rm halo}(R,Z) = \rho\ (R_\odot, 0) \left( \frac{R_\odot}{\sqrt{R^2 + (Z/q)^2}} \right)^{r_{\rm halo}} \tag{2.9}$$

with a halo flattening parameter $q$ and a halo density gradient $r_{\rm halo}$. The three profiles are added together, with the appropriate scaling factors, $f$, to give the stellar density profile of the Galaxy:

$$\rho\ (R,Z) = f_{\rm thin}\ \rho_{\rm thin} + f_{\rm thick}\ \rho_{\rm thick} + f_{\rm halo}\ \rho_{\rm halo}. \tag{2.10}$$

The scaling factors are normalized such that $f_{\rm thin} + f_{\rm thick} + f_{\rm halo} = 1$. With the large number of stars imaged in the SDSS, robust stellar density functions have been measured for the thin and thick disks using the low-mass stars (Jurić et al. 2008; Bochanski et al. (2010)) and for the halo using the main-sequence turn-off stars (Jurić et al. 2008). The values measured for the disk in the two studies are in rough agreement. We adopted the disk parameters from Bochanski et al. (2010) and the halo parameters from Jurić et al. (2008); Table II.2 summarizes the adopted values.

#### 2.3.2.2 Galactic Kinematics

Compared to the positions, the kinematics of the stellar components are not as well characterized; in fact, apart from their large velocity dispersions, little is known about the halo kinematics. We seek to compare the proper motions of a candidate pair with the expected proper motions for that pair given its Galactic position. Thus, we found it prudent to (i)

Table II.2. Galactic model: Galactic structure parameters

| Component | Parameter name | Parameter description | Adopted Value |
|---|---|---|---|
| | $\rho\ (R_\odot, 0)$ | stellar density | 0.0064 |
| thin disk | $f_{\rm thin}$ | fraction[a] | 1-$f_{\rm thick}$-$f_{\rm halo}$ |
| | $H_{\rm thin}$ | scale height | 260 pc |
| | $L_{\rm thin}$ | scale length | 2500 pc |
| thick disk | $f_{\rm thick}$ | fraction[a] | 9% |
| | $H_{\rm thick}$ | scale height | 900 pc |
| | $L_{\rm thick}$ | scale length | 3500 pc |
| halo | $f_{\rm halo}$ | fraction[a] | 0.25% |
| | $r_{\rm halo}$ | density gradient | 2.77 |
| | $q\ (= c/a)$[b] | flattening parameter | 0.64 |

[a]Evaluated in the solar neighborhood

[b]Assuming a bi-axial ellipsoid with axes $a$ and $c$

Note. — The parameters were measured using M dwarfs for the disk (Bochanski et al. 2010) and main-sequence turn-off stars for the halo (Jurić et al. 2008) in the SDSS footprint.

ignore the halo component, with its unconstrained kinematics, at distances where its contributions are expected to be minimal and (ii) limit our model to a distance of 2500 pc, which corresponds to the Galactic height where the number of halo stars begins to outnumber disk stars (Jurić et al. 2008). In practice, all the SLoWPoKES CPM pairs, with the exceptions of subdwarfs for which distances were known to be overestimated, were within ∼1200 pc (see Figure 2.9 below); so we did not introduce any significant systematics with these restrictions.

An ensemble of stars in the Galactic Plane can be characterized as having a purely circular motion with a velocity, $V_{\rm circ}$. The orbits become more elliptic and eccentric over time due to kinematic heating causing the azimuthal velocity, $V_\phi$, to decrease with the Galactic height, Z. However, the mean radial ($V_r$) and perpendicular ($V_z$) velocities for the ensemble at any $Z$ remains zero, with a given dispersion, as there is no net flow of stars in either direction. In addition, this randomization of orbits also causes the asymmetric drift, $V_{\rm a}$, which increases with the age of stellar population and is equivalent to ∼10 km s$^{-1}$ for M dwarfs. Hence, the velocities of stars in the Galactic disk can be summarized, in Galactic cylindrical coordinates,

as:

$$\langle V_r\ (Z)\rangle = 0$$
$$\langle V_\phi\ (Z)\rangle = V_{\rm circ} - V_{\rm a} - f(Z)$$
$$\langle V_z\ (Z)\rangle = 0, \tag{2.11}$$

where $V_{\rm circ} = 220$ km s$^{-1}$, $V_{\rm a} = 10$ km s$^{-1}$, $f(Z) = 0.013\ |Z| - 1.56 \times 10^{-5}\ |Z|^2$ was derived by fitting a polynomial to the data in West et al. (2008), and $Z$ is in parsecs. This formulation of $V_\phi(Z)$ is consistent with a stellar population composed of a faster thin disk ($\langle V_\phi \rangle = 210$ km s$^{-1}$) and a slower thick disk ($\langle V_\phi \rangle = 180$ km s$^{-1}$). Then, we converted these galactocentric polar velocities to the heliocentric, Cartesian $UVW$ velocities. The $UVW$ velocities, when complemented with the dispersions, can be converted to a two-dimensional proper motion (and radial velocity; Johnson & Soderblom 1987), analogous to our input catalog. We used the $UVW$ velocity dispersions measured for SDSS low-mass dwarfs (Bochanski et al. 2007a). All the dispersions were well described by the power-law

$$\sigma(Z) = k\ |Z|^n, \tag{2.12}$$

where the values of constants $k$ and $n$ are summarized in Table II.3. As the velocity dispersions in Bochanski et al. (2007a) extend only up to ∼1200 pc, we extrapolated the above equation for larger distances. While the velocity ellipsoids of F and G dwarfs have been measured to larger distances (e.g., Bond et al. 2010), we preferred to use the values measured for M dwarfs for our low-mass sample.

#### 2.3.2.3 The Model

By definition, a chance alignment occurs because two physically unassociated stars randomly happen to be close together in our line of sight (LOS), within the errors of our measurements. Due to the random nature of these chance alignments, it is *not* sufficient to estimate the probability of chance alignment along a given LOS simply by integrating Eq. (2.10). This would tend to underestimate the true number of chance alignments because

Table II.3. Galactic model: Galactic kinematics parameters

| Galactic component | Velocity | $k$ | $n$ |
|---|---|---|---|
| thin disk | $U$ | 7.09 | 0.28 |
| | $V$ | 3.20 | 0.35 |
| | $W$ | 3.70 | 0.31 |
| thick disk | $U$ | 10.38 | 0.29 |
| | $V$ | 1.11 | 0.63 |
| | $W$ | 0.31 | 0.31 |

Note. — The constants in the power law, $\sigma(Z) = k|Z|^n$, that describes the velocity dispersions of the stars in the thin and thick disks. The velocity dispersions were measured from a spectroscopic sample of low-mass dwarfs (Bochanski et al. 2007a).

the density profiles in Eqs. (2.7–2.9) are smooth functions that, in themselves, do not include the random scatter about the mean relation that real stars in the real Galaxy have. Thus, the stars need to be randomly redistributed spatially about the average given by Eq. (2.10) in order to properly account for small, random fluctuations in position and velocity that could give rise to false binaries in our data.

In principle, one could simulate the whole Galaxy in this fashion in order to determine the probabilities of chance alignments as a function of LOS. In practice, this requires exorbitant amounts of computational time and memory. Since our aim was to calculate the likelihood of a false positive along specific LOSs, we, instead, generated stars in much smaller regions of space, corresponding to the specific binaries in our sample. For example, a $30' \times 30'$ cone integrated out to a distance of 2500 pc from the Sun will contain at least a few thousand stars within any of the specific LOSs in our sample. The number of stars is large enough to allow for density variations similar to that of the Milky Way while small enough to be simulated with ease. With a sufficient number of Monte Carlo realizations, the random density fluctuations along each LOS can be simulated. We found that $10^5$ realizations allowed for the results to converge, within $\sim$0.5%.

We implemented the following recipe to assess the false-positive likelihood for each candidate pair using our Galactic model:

1. The total number of stars in the LOS volume defined by a $30' \times 30'$ area, centered on

the $\alpha$ and $\delta$ of a given binary, over heliocentric distances of 0–2500 pc was calculated by integrating Eq. (2.10) in 5 pc deep, discrete cylindrical "cells."

Integrating Eq. (2.10) for $\Delta\theta = 30'$ and $d$ = 0–2500 pc resulted in ∼3300–1580 stars, with the higher numbers more likely to be the LOSs along the Galactic Plane. This number of stars, when randomly redistributed in the entire volume, was more than enough to recreate over-densities and under-densities.

2. The stars were then distributed in three-dimensional space defined by the LOS using the rejection method (Press et al. 1992), generating $\alpha$, $\delta$, and $d$ for each star. The rejection method ensured that the stars were randomly distributed while following the overlying distribution function, which, in this case, was the stellar density profile given by Eq. (2.10).

   The model did an excellent job of replicating the actual distribution of stars in the three-dimensional space. The red histograms in Figure 2.5 show the number of stars from the center of the LOS as a function of angular separation for the model (dashed lines) and the data (solid lines), averaged over all LOSs where candidate binaries were identified in Section 2.3.1. There is an excess of pairs at close separations, a signature of genuine, physically associated pairs, while the two distributions follow the same functional form at larger separations, where chance alignments dominate. The increasing number of pairs with angular separation is an evidence of larger volume that is being searched. Integrating the model predicts ∼8.0 stars within a search radius of $60''$ and ∼71 within $180''$. In other words, for a typical LOS with candidate binaries, we would, on average, expect to find 8 chance alignments within $60''$ and ∼71 within $180''$ when considering only angular separation.

   For the $180''$ radius around each LOS, the average number of stars in the model and the data were within a few $\sigma$ of each other, with the largest deviations found along the LOSs at low Galactic latitudes or large distances. As our model only integrated to $d$ = 2500 pc, deviations for LOSs at large distances were expected. Deviations for LOSs at low Galactic latitudes are reasonable as the parameters in Eqs. (2.7) and (2.8) as not as well constrained along the Galactic disk. Hence, we concluded that the rejection

method used in redistributing the stars in the $30' \times 30'$ LOS is correctly implemented and that the model successfully replicates the three dimensional spatial distribution of the stars in the Galaxy.

When the distances were matched, the number of pairs decreased as chance alignments were rejected (blue histograms in Figure 2.5); *there are, on average, only ∼0.41 and ∼3.6 chance alignments within 60″ and 180″, respectively.* Note that matching distances, in addition to the angular separation, significantly enhanced the peak at the small separations.

3. Based on the Galactic position of each randomly generated star, mean $UVW$ space velocities and their dispersions were generated based on Eq. (2.11) and Eq. (2.12), respectively. Proper motions were then calculated by using the inverse of the algorithm outlined in Johnson & Soderblom (1987). These generated proper motions represent the expected kinematics of stars at the given Galactic position.

   Figure 2.6 shows the comparison between the proper motions in the SDSS/USNO-B catalog and our model; component proper motions of stars within $60'$ of all LOSs, where candidate pairs were found. For the purposes of his plot, we restricted the stars to be within 1200 pc and of spectral type K5 or later so we could compare kinematics with a sample similar to our resultant catalog. We also did not compare the distributions at $\mu_\alpha$ or $\mu_\delta \lesssim 10$ mas yr$^{-1}$ where the proper motions are comparable to the 1-$\sigma$ errors and, hence, not reliable. Since our initial sample was has $\mu \geq 40$ mas yr$^{-1}$, stars with the small proper motion component are either rejected or their motion is dominated by the other component in our analysis. As evidenced in the figure, our model reproduced the overall kinematic structure of the thin and thick disks.

   When the proper motions were matched (purple histograms in Figure 2.5), in addition to the angular separation and distances, the number of chance alignments fell drastically, especially at the smaller separations. In fact, at $\Delta\theta \leq 15''$, there were $< 10^{-4}$ chance alignments, on average; even at $\Delta\theta = 180''$, the real pairs outnumbered the chance alignments by a factor of 4–5. Cumulatively, for a typical LOS, there were, on average, only ∼0.0097 and ∼0.086 chance alignments within $60''$ and $180''$, respec-

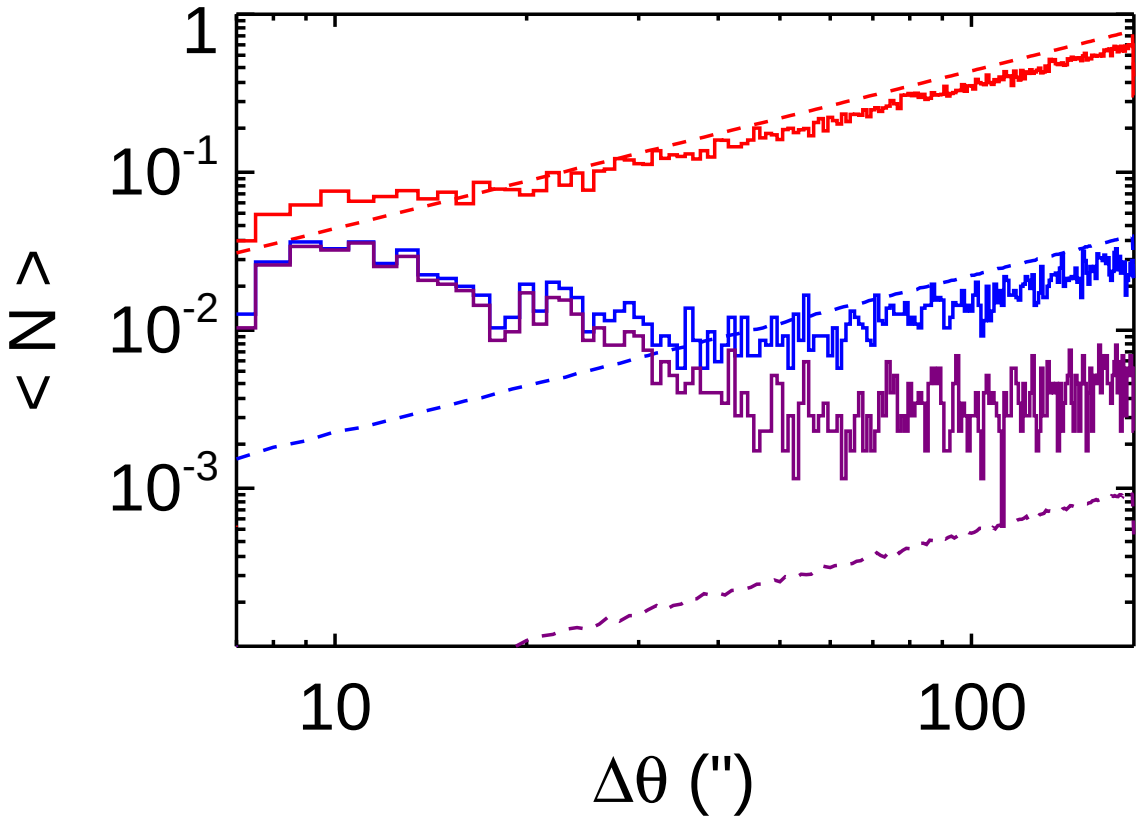


Figure 2.5: The distribution of the (average) number of stars found around the LOSs around our binary candidates as calculated from the SDSS DR7 data (solid histograms) and our Galactic model (dashed histograms). All optical pairs (red), pairs with matching distances (blue), and pairs with matching distances and proper motion components (purple) are shown. The excess at small separations, a signature of real pairs, is enhanced as additional properties are matched. Unlike the rest of the chapter, we counted all stars with $r \leq 22.5$, without any quality cuts, for this plot to do a realistic comparison with the model. Note that $\langle N \rangle$ denotes the number of stars found at that angular separation (counted in $1''$ bins). We used the raw parameters for the Galactic model (Jurić et al. 2008, Bochanski et al. (2010)). As a whole, the model does an excellent job of mimicking the number of stars and their spatial and kinematic distribution in the Milky Way along typical SDSS LOSs.

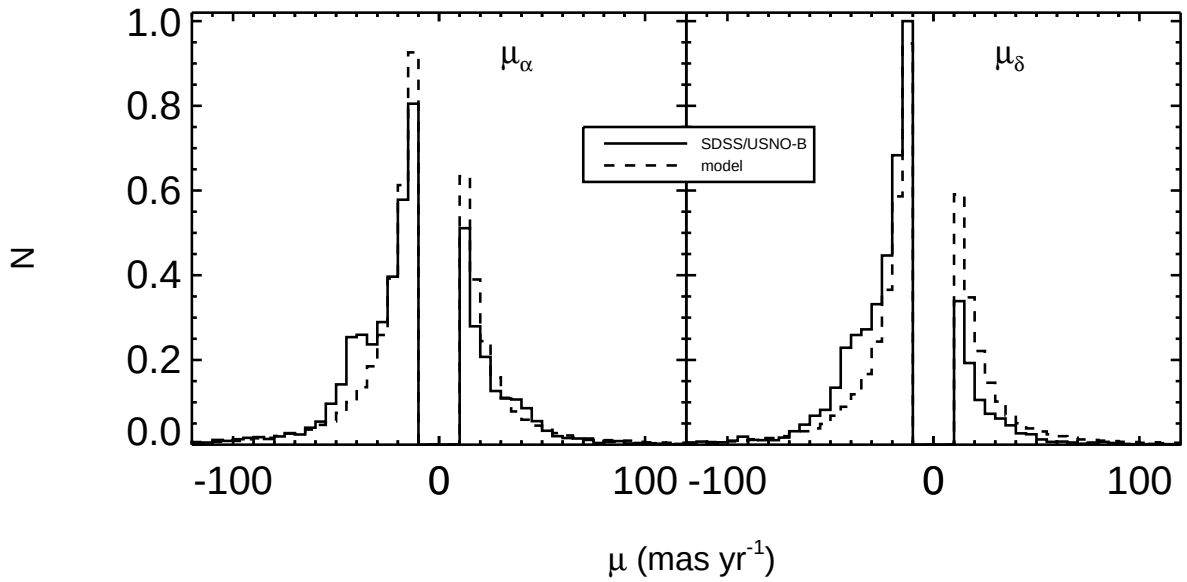


Figure 2.6: Proper motion distributions for stars within 60′ of LOSs along all identified candidate pairs in SDSS/USNO-B (solid histograms) and in our Galactic model (dashed histograms). For the purposes of this plot, we restricted the stars to be of spectral types K5 or later and be within 1200 pc to avoid being skewed by systematic differences. In addition, we do not compare proper motion components $< 10$ mas yr$^{-1}$ as they comparable to the 1-$\sigma$ errors and, hence, not reliable (see text). Again, the kinematics of the thin and thick disk of the Milky Way are very well reproduced by our Monte Carlo model.

tively. As a result of matching distance and proper motions components, the number of chance alignments within 180″ were reduced by a factor of ∼800.

4. In the model galaxy, we repeated the selection process used to find CPM pairs in the SDSS photometric catalog, as described in Section 2.3.1. To avoid double-counting, the input coordinates of the LOS were considered to be the primary star. Note that we did not intend to model and reproduce both stars of a given pair but wanted to see if a random chance alignment could produce a companion for a given primary. Hence, each additional star that was found to satisfy Eqs. (2.5) and (2.6) was counted as an optical companion. The average number of companions found in the $10^5$ Monte Carlo realizations is the probability of chance alignment or the probability that the candidate pair is a false positive, $P_{\rm f}$, for that candidate pair. The number of realizations sets the resolution of $P_{\rm f}$ at $10^{-5}$.

5. Finally, this was repeated for all candidate pairs that were found in Section 2.3.1. Figure 2.7 shows the distribution of $P_{\rm f}$ all of the candidate pairs; we further discuss this distribution is Section 2.3.3.

To conclude, the result of our Galactic model was a $30' \times 30'$ area of the sky, centered around the given CPM pair, with the surrounding stars following the Galactic spatial and kinematic distributions of the Milky Way. Each star in this model galaxy was described by its position ($\alpha$, $\delta$, and $d$) and proper motion ($\mu_\alpha$and $\mu_\delta$), same as is available for SDSS photometric catalog. Based on the above results, we concluded that the Galactic model sufficiently reproduced the five-dimensional (three spatial and two kinematic[6]) distribution of stars along typical LOSs in the Milky Way and, thus, allowed for the calculation of probability that a given CPM double is a chance alignment.

### 2.3.3 Fidelity

As described in the previous section, we have implemented a very stringent selection algorithm in identifying the CPM pairs. In addition to only including objects with the most robust photometry and proper motions, we also used a relatively high proper motion cut of $\mu \geq 40$ mas yr$^{-1}$ for the input sample, which considerably decreased the number of low-mass stars. As described above, an algorithm optimized to reject the most false positives, even at the expense of real pairs, was used in the statistical matching of angular separation, photometric distance, and proper motion components. Lastly, we used the Galactic model to quantify the probability of chance alignment, $P_{\rm f}$, for each of the 1558 candidate pairs.

Normally all candidate pairs with $P_{\rm f} \leq 0.5$, i.e. a higher chance of being a real rather than a fake pair, could be used to identify the binaries. However, to minimize the number of spurious pairs, we required

$$P_{\rm f} \leq 0.05. \tag{2.13}$$

for a pair to be classified as real. Here we note that $P_{\rm f}$ represents the false-alarm probability that a candidate pair identified by matching angular separation, photometric distance, and

[6]The model also predicts radial velocities. We have an observational program underway to obtain radial velocities of the binaries for further refinement of the sample.

proper motion components, as described by Eqs. (2.5) and (2.6), is a real pair; it is not the probability that a random low-mass star is part of a wide binary.

Making the above cut on $P_{\rm f}$ resulted in a catalog of 1342 pairs, with a maximum of 5% or 67 of the pairs expected to be false positives. However, as a large number of the pairs have extremely small $P_{\rm f}$ (see Figure 2.7), the number of false positives is likely to be much smaller. Adding up the $P_{\rm f}$ for the pairs included in the catalog gives an estimated 22 (1.65%) false positives. In other words, the overall fidelity of SLoWPoKES is 98.35%. This is a remarkably small proportion for a sample of very wide pairs, especially since they span a large range in heliocentric distances and is a testament to our selection criteria. For example, if the proper motion components were matched to within 2 $\sigma$, Eq. (2.13) would have rejected $\gtrsim 60\%$ of the candidates. Our choice of Eq. (2.13) is a matter of preference; if a more efficient (or larger) sample is needed, it can be changed to suit the purpose.

To get a first-order approximation of how many real binaries we are missing or rejecting, we applied our selection algorithm to the rNLTT CPM catalog with 1147 pairs (Chanamé & Gould 2004). Note that Chanamé & Gould (2004) did not match distances of the components, as they did not have reliable distance estimates available and matched total proper motions instead of a two-dimensional vector matching in our approach. Out of the 307 rNLTT pairs, which have $\Delta\theta \leq 180''$ and are within the SDSS footprint, we recover both components of 194 systems (63%) and one component of another 56 (18%) systems, within $2''$ of the rNLTT coordinates. Of the 194 pairs for which both components had SDSS counterparts, 59 (30%) pairs satisfied our criteria for proper motions, Eq. (2.6), while 19 (10%) pairs satisfied our criteria for both proper motions and distances, Eqs. (2.5) and (2.6). In other words with our selection criteria, we recovered only 10% of the rNLTT pairs, with SDSS counterparts, as real binaries. If we relax our selection criteria to match within 2-$\sigma$, the number of recovered pairs increases to 82 with matching proper motions and 37 with matching proper motions and distances. Of course, as the rNLTT is a nearby, high proper motion catalog, Chanamé & Gould (2004) had to allow for larger differences in proper motions due to the stars' orbital motion, which is not applicable to the SLoWPoKES sample (see Section 2.3.1). In conclusion, compared to previous catalogs of CPM doubles, we find a small fraction of previously identified very wide binaries. The reasons for the low recovery

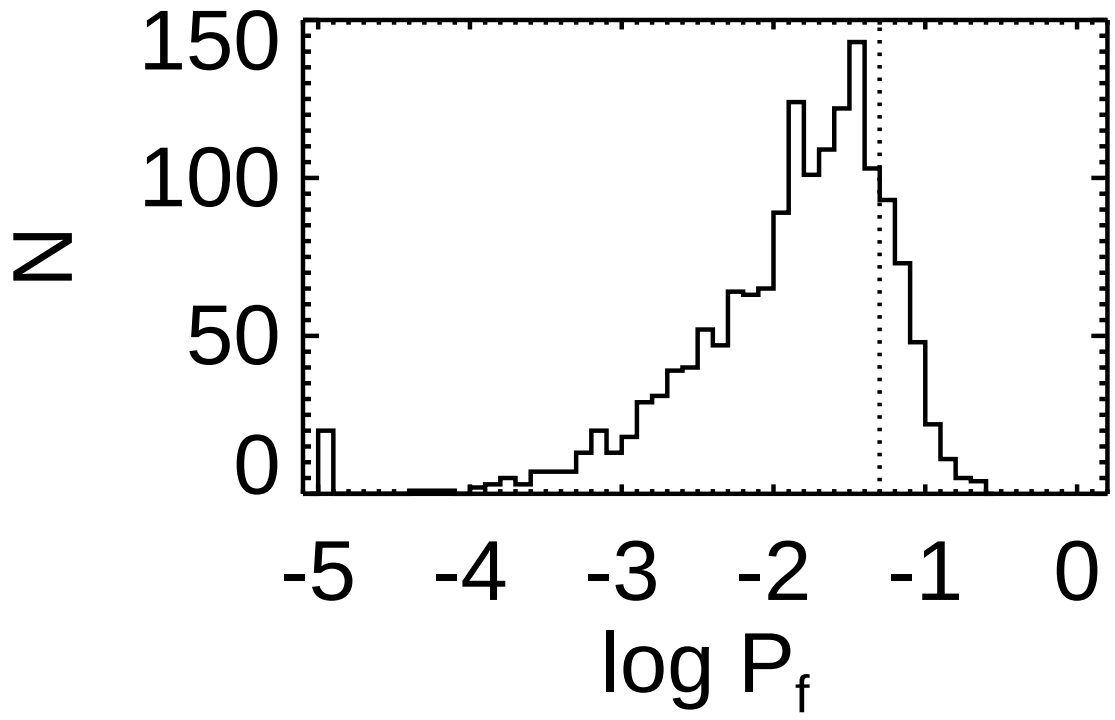


Figure 2.7: The probability of chance alignment ($P_{\rm f}$) for candidate SLoWPoKES pairs based on their positions and kinematics, as calculated by our Galactic model. We adopted $P_{\rm f} = 0.05$ (dotted line) as our threshold for inclusion in the SLoWPoKES catalog. The resolution of the Monte Carlo simulation is $10^{-5}$, which causes the peak at log $P_{\rm f} = 10^{-5}$.

rate are two-fold: (i) the restrictive nature of our matching algorithm that rejects the most false positives, even at the expense of real pairs and (ii) improvement in the identification method—e.g., matching proper motions in vector space and being able to use photometric distance as an additional criterion.

## 2.4 Characteristics of the SLoWPoKES catalog

Using statistical matching of angular separation, photometric distance, and proper motion components, we identified 1598 very wide, CPM double candidates from SDSS DR7. We built a Galactic model, based on empirical measurements of the stellar density profile and kinematics, to quantitatively evaluate the probability that each of those candidate

Table II.4. Properties of SLoWPoKES pairs (Part I)

| ID[a] | Position (J2000) | | | | Photometry[b] | | | | | |
|---|---|---|---|---|---|---|---|---|---|---|
| | $\alpha_A$ | $\delta_A$ | $\alpha_B$ | $\delta_B$ | $r_A$ | $i_A$ | $z_A$ | $r_B$ | $i_B$ | $z_B$ |
| SLW | (deg) | | | | (mag) | | | | | |
| J0002+29 | 0.515839 | 29.475183 | 0.514769 | 29.470617 | 16.79 (0.02) | 15.85 (0.02) | 15.33 (0.02) | 19.35 (0.02) | 17.91 (0.02) | 17.17 (0.02) |
| J0004−10 | 1.122441 | -10.324043 | 1.095927 | -10.296753 | 18.25 (0.02) | 17.08 (0.02) | 16.46 (0.02) | 18.66 (0.02) | 17.42 (0.02) | 16.70 (0.02) |
| J0004−05 | 1.223125 | -5.266612 | 1.249632 | -5.237299 | 14.85 (0.01) | 14.31 (0.01) | 14.02 (0.02) | 19.56 (0.02) | 18.10 (0.01) | 17.31 (0.02) |
| J0005−07 | 1.442631 | -7.569930 | 1.398478 | -7.569359 | 17.35 (0.02) | 16.25 (0.01) | 15.65 (0.01) | 18.78 (0.02) | 17.43 (0.02) | 16.69 (0.01) |
| J0005+27 | 1.464802 | 27.325805 | 1.422484 | 27.300282 | 18.91 (0.02) | 17.63 (0.02) | 16.94 (0.01) | 19.79 (0.02) | 18.29 (0.02) | 17.50 (0.02) |
| J0006−03 | 1.640868 | -3.928988 | 1.641011 | -3.926589 | 17.06 (0.01) | 16.01 (0.02) | 15.44 (0.01) | 17.88 (0.01) | 16.62 (0.02) | 15.93 (0.01) |
| J0006+08 | 1.670973 | 8.454040 | 1.690136 | 8.498541 | 19.48 (0.02) | 18.14 (0.02) | 17.45 (0.02) | 19.57 (0.02) | 18.15 (0.01) | 17.43 (0.02) |
| J0007−10 | 1.917002 | -10.340915 | 1.924510 | -10.338869 | 17.43 (0.01) | 16.50 (0.01) | 16.02 (0.03) | 18.33 (0.01) | 17.24 (0.01) | 16.66 (0.03) |
| J0008−07 | 2.135590 | -7.992694 | 2.133660 | -7.995245 | 17.33 (0.01) | 16.35 (0.02) | 15.86 (0.02) | 18.14 (0.01) | 16.98 (0.02) | 16.36 (0.02) |
| J0009+15 | 2.268841 | 15.069630 | 2.272453 | 15.066457 | 18.52 (0.02) | 17.00 (0.02) | 16.09 (0.01) | 18.39 (0.02) | 16.83 (0.02) | 15.95 (0.01) |

[a]The identifiers were generated using the standard *Jhhmm±dd* format using coordinates of the primary star and are prefaced with the string 'SLW'.

[b]All magnitudes are psfmag and have not been corrected for extinction. Their errors are listed in parenthesis. Note that we use extinction-corrected magnitudes in our analysis.

Note. — The first 10 pairs are listed here; the full version of the table is available online on the SLoWPoKES website (`http://www.vanderbilt.edu/astro/slowpokes/`) and *the Astronomical Journal* website (`http://iopscience.iop.org/1538-3881/139/6/2566/`).

Table II.5. Properties of SLoWPoKES pairs (Part II)

| ID[a] | Proper Motion | | | | Distance[b] | | Spectral Type[c] | | Binary Information | | | | | |
|---|---|---|---|---|---|---|---|---|---|---|---|---|---|---|
| | $\mu_{\alpha_A}$ | $\mu_{\delta_A}$ | $\mu_{\alpha_B}$ | $\mu_{\delta_B}$ | $d_A$ | $d_B$ | $A$ | $B$ | $\Delta\theta$ | $\Delta\mu$ | $\Delta d$ | BE | $P_{\rm f}$ | Class[d] |
| SLW | (mas yr$^{-1}$) | | | | (pc) | | | | ($''$) | (mas yr$^{-1}$) | (pc) | ($10^{40}$ ergs) | (%) | |
| J0002+29 | 198 (2) | 38 (2) | 197 (3) | 35 (3) | 341 | 301 | M1.7 | M3.6 | 16.8 | 2.9 | 39 | 58.08 | 0.000 | SD |
| J0004−10 | 43 (3) | -4 (3) | 36 (4) | -8 (4) | 362 | 338 | M2.7 | M3.1 | 135.9 | 7.5 | 23 | 3.94 | 0.036 | DD |
| J0004−05 | 101 (2) | 11 (2) | 99 (4) | 8 (4) | 301 | 333 | K7.1 | M3.8 | 142.0 | 3.1 | 31 | 13.45 | 0.006 | DD |
| J0005−07 | 30 (2) | -21 (2) | 30 (3) | -27 (3) | 296 | 273 | M2.4 | M3.4 | 157.6 | 6.0 | 23 | 4.90 | 0.015 | DD |
| J0005+27 | 10 (3) | -40 (3) | 5 (4) | -40 (4) | 357 | 380 | M3.1 | M3.9 | 163.6 | 5.5 | 22 | 2.26 | 0.037 | DD |
| J0006−03 | -40 (2) | -35 (2) | -40 (2) | -31 (2) | 242 | 270 | M2.2 | M3.1 | 8.7 | 3.9 | 27 | 112.47 | 0.005 | DD |
| J0006+08 | -48 (4) | -5 (4) | -41 (4) | -3 (4) | 417 | 476 | M3.3 | M3.5 | 174.1 | 7.5 | 58 | 1.59 | 0.033 | DD |
| J0007−10 | 37 (3) | 34 (3) | 42 (4) | 31 (4) | 429 | 445 | M1.5 | M2.3 | 27.6 | 5.6 | 16 | 27.74 | 0.034 | DD |
| J0008−07 | -9 (2) | -42 (2) | -7 (3) | -41 (3) | 344 | 379 | M1.7 | M2.7 | 11.5 | 2.3 | 34 | 74.69 | 0.017 | DD |
| J0009+15 | 36 (3) | -16 (3) | 37 (3) | -21 (3) | 150 | 161 | M4.2 | M4.2 | 17.0 | 4.8 | 11 | 21.02 | 0.004 | DD |

[a]The identifiers were generated using the standard *Jhhmm±dd* format using coordinates of the primary star and are prefaced with the string 'SLW'.

[b]The distances were calculated using photometric parallax relations and have 1 $\sigma$ errors of ∼14%. The absolute distances to subdwarfs (SDs) are overestimated (see Section 2.2.4.1).

[c]The spectral types were inferred from the $r-z$ colors (West et al. 2008; Covey et al. 2007) and are correct to ±1 subtype.

[d]Class denotes the various types of pairs in SLoWPoKES. See Table II.6.

Note. — The first 10 pairs are listed here; the full version of the table is available online on the SLoWPoKES website (`http://www.vanderbilt.edu/astro/slowpokes/`) and *the Astronomical Journal* website (`http://iopscience.iop.org/1538-3881/139/6/2566/`).

Table II.6. The SLoWPoKES binaries

| Class | Type | Number |
|---|---|---|
| DD | disk dwarf | 1245 |
| SD | subdwarf | 70 |
| WD | white dwarf–disk dwarf | 21 |
| T | triple | 4 |

doubles are real (Figure 2.7). Using Eq. (2.13), we classified 1342 pairs as real, associated pairs. In deference to their extremely slow movement around each other, we dubbed the resulting catalog SLoWPoKES for Sloan Low-mass Wide Pairs of Kinematically Equivalent Stars. Tables II.4 and II.5 lists the properties of the identified pairs. The full catalog is publicly available on the world wide web[7]. SLoWPoKES is intended to be a "live" catalog of wide, low-mass pairs, i.e., it will be updated as more pairs are identified and as follow-up photometric and spectroscopic data become available.

Figure 2.8 shows a collage of *gri* composite images, 50″ on a side, of a selection of representative SLoWPoKES systems; the images are from the SDSS database. In the collage high-mass ratio pairs (top row; mass ratio = $m_2/m_1 < 0.5$), equal-mass pairs (middle row; having masses within ∼5% of each other), white dwarf–disk dwarf pairs (bottom row, left), and halo subdwarf pairs (bottom row, right) are shown. Table II.6 summarizes the different types of systems in the catalog.

In the sections that follow, we summarize various aspects of the systems that constitute the SLoWPoKES catalog and briefly examine some of the follow-up science that can be pursued with SLoWPoKES. We wish to emphasize that the SLoWPoKES catalog is intended principally as a high-fidelity sample of CPM doubles that can be used for a variety of follow-up investigations where the reliability of each object in the catalog is more important than sample completeness. Thus, we have not attempted to fully account for all sources of incompleteness or bias; and we intentionally have not applied any form of statistical "corrections"

[7] `http://www.vanderbilt.edu/astro/slowpokes/`

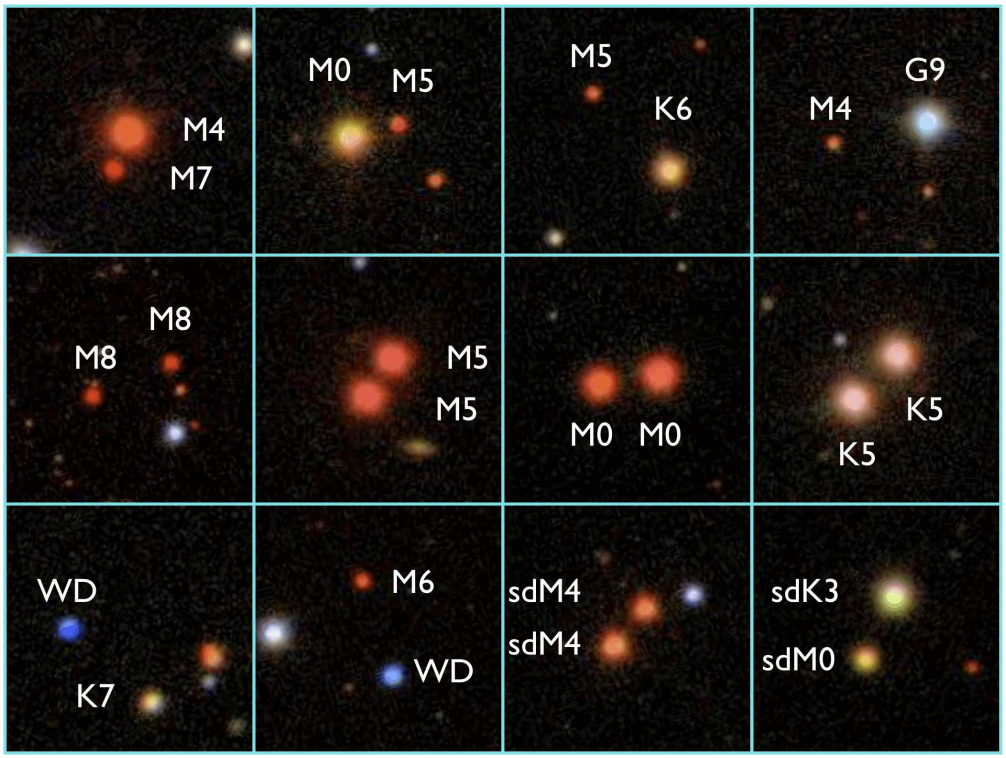


Figure 2.8: $50'' \times 50''$*gri* composite images of CPM pairs found in the SLoWPoKES survey. Pictured are high-mass ratio pairs (top row), identical twins (middle row), white dwarf–disk dwarf pairs (bottom row, left), and halo subdwarf pairs (bottom row, right). Spectral types, based on their $r - z$ colors are shown. Overall, 1342 wide, low-mass binaries were identified.

to the catalog.

We note that some of the most important sources of incompleteness in the present catalog could be at least partially overcome with follow-up observations. For example, the principal incompleteness in SLoWPoKES arises from the lack of proper motions for SDSS stars that were not detected in USNO-B. Proper motions either do not exist or are not reliable for stars (i) fainter than $r = 20$ or (ii) within $7''$ of a brighter star. The first criterion currently rules out most of the mid–late M dwarf companions, while the latter rejects close binaries and most hierarchical higher-order systems. However, as the SDSS photometric and astrometric data are available for these systems, their multiplicity could be verified with more rigorous analysis or through cross-matching with other catalogs. For example, by cross-matching SDSS with 2MASS, an M4.5–L5 binary (Radigan et al. 2008) and an M6–M7 binary (Radigan et al. 2009) have already been identified. At the other end of the spectrum, SDSS saturates at

$r \approx 14$, resulting in saturated or unreliable photometry for the brighter stars. We found that more than 1000 candidate pairs were rejected for this reason; with reliable follow-up photometry these could be added as additional genuine SLoWPoKES binaries.

Even so, a fully volume-complete sample is likely to be impossible to compile over the full ranges of spectral types and distances spanned by our catalog. For example, our magnitude limits of $14 \lesssim r \leq 20$ imply that while we are sensitive to K5 dwarfs at ∼250–3900 pc, we are sensitive to M5 dwarfs at ∼14–180 pc. This means (i) we are entirely insensitive to pairs with the most extreme mass ratios (i.e. a K5 paired with an M6 or M7) and (ii) we cannot directly compare the properties of K5 and M5 spectral subtypes in identical distance ranges. In addition, as illustrated in Figure 2.9, with our $7'' \leq \Delta\theta \leq 180''$ search radius we are sensitive to companions with separations of ∼700–18000 AU at 100 pc but ∼7000–180000 AU at 1000 pc. Thus, it is important with the current catalog that statistical determinations of ensemble system properties be performed within narrowly defined slices of separation and distance. We do so in the following subsections as appropriate; but we emphasize again that our intent here is primarily to *characterize* the SLoWPoKES sample and will proffer any interpretive conclusions only tentatively.

Finally, as is evident from Table II.6, the current SLoWPoKES catalog is clearly not well suited for study of higher-order multiples (i.e. triples, quadruples, etc.). Identifying CPM higher-order multiple systems in SDSS is very challenging due to the lack of reliable proper motions in the SDSS/USNO-B matched catalog at $\Delta\theta < 7''$ and $r > 20$. Unless all components are widely separated and are all bright, they will be rejected in our search. In addition, we are currently rejecting hierarchical triples consisting of a close pair that is unresolved in SDSS and a wide, CPM tertiary. If the mass ratio of the close, unresolved pair is near unity, it will appear as an over-luminous single star that will then be misinterpreted by our algorithm as having a discrepant photometric distance from its wide tertiary companion. The available SDSS photometry and astrometry shows evidence of a substantial number of such multiple systems, and we plan to make these the subject of a future study. Already, four CPM triples are identified in our search (Table II.6). Moreover, the current SLoWPoKES catalog is likely to contain quadruple systems in which the two components of the identified wide binary are themselves in fact spatially unresolved binaries with near-equal mass com-

ponents. We have initiated an adaptive optics program to identify such higher-order systems in the SLoWPoKES catalog.

### 2.4.1 Kinematic Populations

Luyten (1922) devised the reduced proper motion (RPM) diagram to be used in the stead of the H-R diagram when distances to the objects are not available, as is the case in large imaging surveys. The RPM of an object is defined as

$$\mathrm{H} \equiv m + 5\ \log \mu + 5 = M + 5\ \log v_{\mathrm{t}} - 3.25 \tag{2.14}$$

where $v_{\mathrm{t}}$ is the heliocentric tangential velocity in km s$^{-1}$ given by $v_{\mathrm{t}} = 4.74\ \mu\ d$ and $\mu$ is the proper motion in arcseconds yr$^{-1}$. Just as in a H-R diagram, the RPM diagram effectively segregates the various luminosity or kinematic classes from each other (e.g., Chanamé & Gould (2004); Harris et al. (2006); Lépine & Bongiorno (2007); Sesar et al. (2008)).

WDs, in addition to being relatively very blue, are less luminous than either the DDs or the SDs; hence, the observed WDs tend to be nearby disk WDs with high tangential velocities. Specifically, spectroscopic follow-up has shown that the disk WDs with $v_{\mathrm{t}} = 25$–$150$ km s$^{-1}$ (Figure 2.10, black dashed lines) can be effectively identified from the $g$-band RPM diagram, when complemented by photometric parallax relations (Kilic et al. 2006). However, we note that spectroscopic follow-up is needed to confirm that the identified objects are actually WDs. The available SDSS spectra confirm that 9 of the 21 WD primaries, identified in SLoWPoKES, are indeed WDs. As the WDs were identified from the $g$-band, they scatter toward the SD and DD locus in the $r$-band RPM diagram.

Subdwarfs are low-metallicity halo counterparts of the main-sequence dwarfs found in the Galactic disk. Hence, they have bluer colors at a given absolute magnitude (however, the $g - r$ colors for M subdwarfs are redder; West et al. 2004; Lépine & Scholz 2008) and have higher velocity dispersions. As a result, the subdwarfs lie below the disk dwarfs in the RPM diagram[8]. To segregate the SDs from the DDs, we used the DD photometric parallax

[8]Sesar et al. (2008) showed that the RPM diagram becomes degenerate at $Z > 2$–$3$ kpc due to the decrease in rotational velocity. This does not affect our sample.

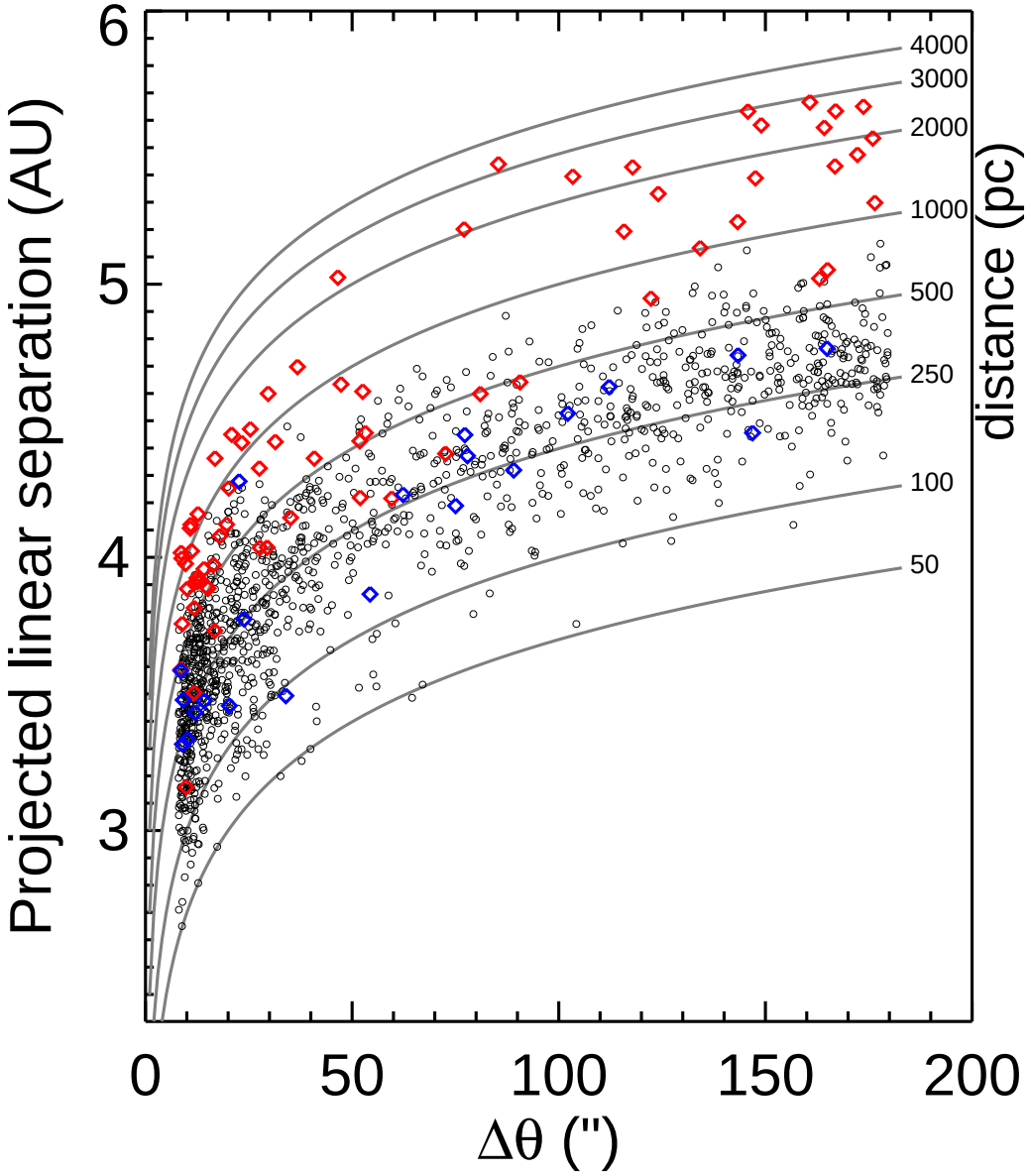


Figure 2.9: The projected linear separation of SLoWPoKES pairs are plotted as a function of angular separation, with the iso-distance lines plotted across the grid. DD (black), SD (red), and WD–DD pairs (blue) are shown. Systematically larger distances for the SDs is clearly seen, which is expected as photometric DD photometric parallax relations were used to calculate the SD distances as well. Hence, SDs are excluded in all analysis involving their distances.

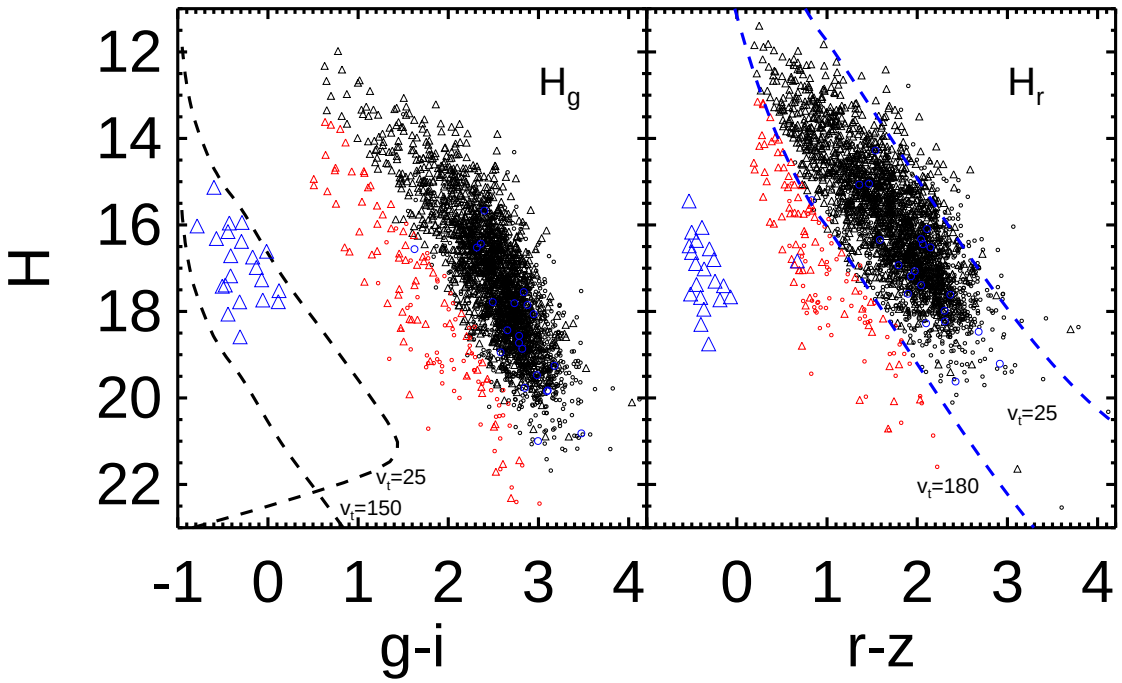


Figure 2.10: SLoWPoKES pairs plotted in the $H_g$ vs. $g-i$ (left) and $H_r$ vs. $r-z$ RPM diagrams; primaries (triangles) and secondaries (circles) of DD (black), SD (red), and WD–DD (blue) pairs are shown. The WDs are identified from the $g$-band RPM diagram, complemented by $M_g(g-i)$ for WDs, as having $25 < v_t < 150$ km s$^{-1}$ (black dashed lines) and are all expected to be part of the disk population. SDs are segregated from the DDs using the $r$-band RPM diagram, assuming SDs have $v_t > 180$ km s$^{-1}$ (blue dashed line) and the DD photometric parallax relations.

relations complemented by the mean tangential velocity of halo stars, $v_t = 180$ km s$^{-1}$. This relation is shown in blue dashed lines in the $r$-band RPM diagram in Figure 2.10. As the mean halo velocity was used, SDs can scatter above the line; but DDs would not be expected to be below the blue line. For comparison, $v_t = 25$ km s$^{-1}$, the mean tangential velocity of disk stars, is also shown. Note that DDs in SLoWPoKES have tangential velocities larger than the mean velocity of the disk, which is expected as we rejected all stars with $\mu <$ 40 mas yr$^{-1}$.

Figure 2.10 shows the $H_g$ vs. $g-i$ and $H_r$ vs. $r-z$ RPM diagrams with both the primary (triangle) and the secondary component (circle) for the 21 WD–DD (blue), 70 SD–SD (red), and 1245 DD–DD (black) pairs that were identified in SLoWPoKES. The properties of the

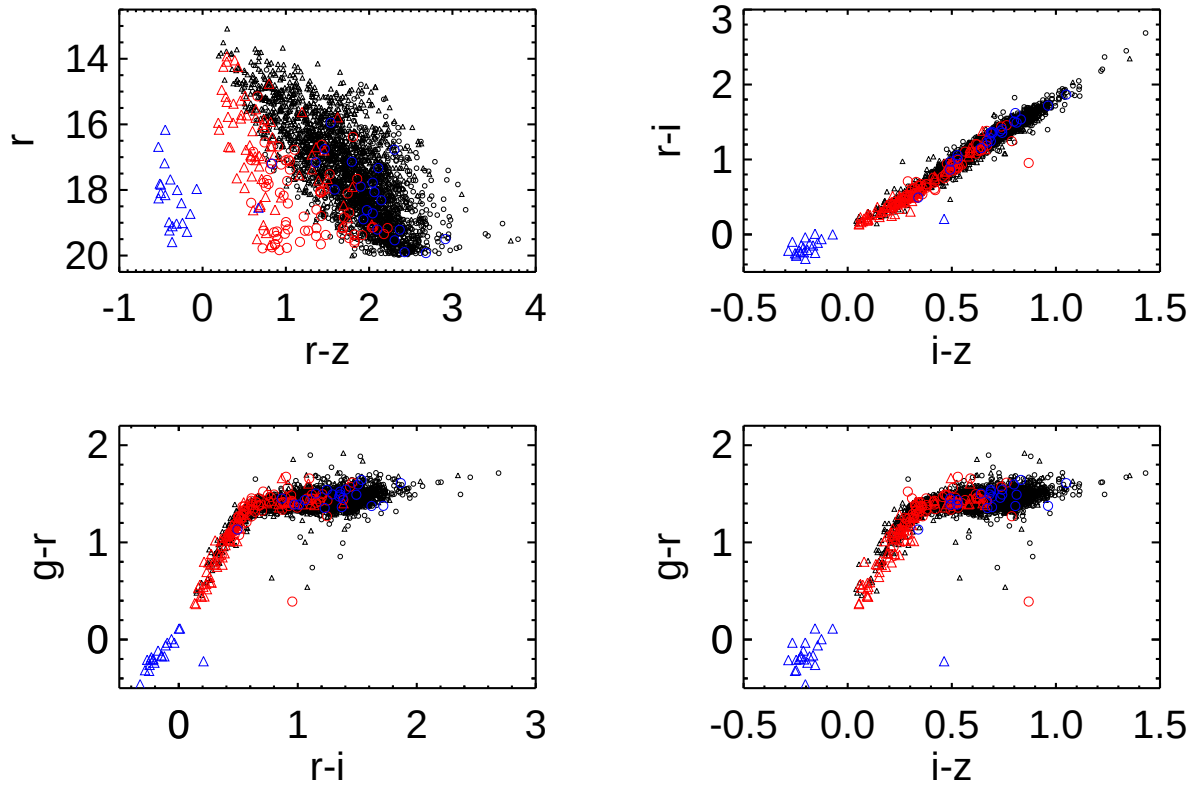


Figure 2.11: $r$ vs. $r-z$ Hess diagram and color-color plots for the SLoWPoKES catalog; shown are the primary (triangles) and secondaries (circles) for DD (black), SD (red), and WD–DD pairs (blue). The subdwarfs are mostly of K spectral type and do not show redder $g-r$ colors at given $r-i$ or $i-z$ colors, as seen in M subdwarfs (West et al. 2004; Lépine & Scholz 2008).

DDs, SDs, and WDs in various color-magnitude and color-color planes are compared in Figure 2.11. The identified SDs are either K or early-M spectral types, as our magnitude and color limits exclude the M subdwarf locus. The overestimation in the distances to SDs is clearly evident in Figure 2.9, as they are at systematically larger distances relative to the DDs. As a result, the calculated physical separations for the SDs are also systematically larger. At present a substantial number of subdwarf candidates are rejected from SLoWPoKES because the overestimated distances result in $\Delta d > 100$ pc.

RPM diagrams have been used to confirm the binarity of CPM pairs in the past (e.g., Chanamé & Gould 2004). As components of a binary system most probably formed from the same material and at the same time, they should be members of the same luminosity

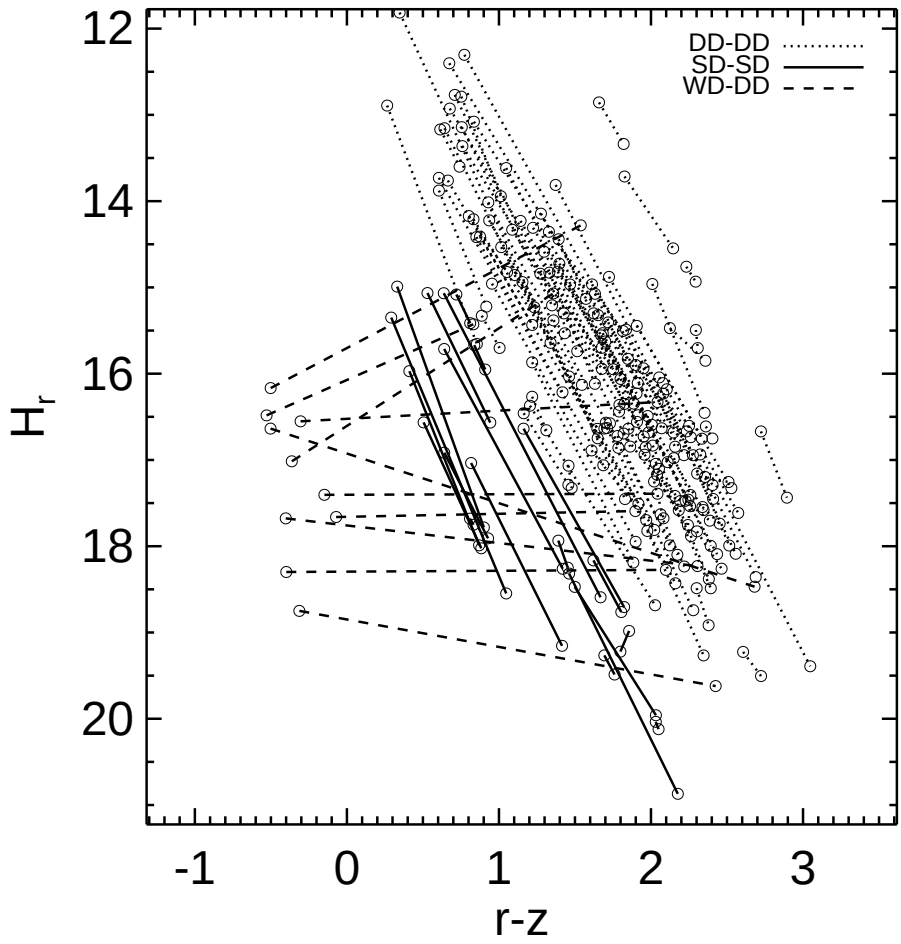


Figure 2.12: A randomly selected sample of SLoWPoKES pairs plotted on the RPM diagram; components of DD (dotted), SD (solid), and WD–DD (dashed) pairs are connected. As binaries are expected to be part of the same kinematic populations, they are expected to lie parallel to the dwarf/subdwarf tracks with the obvious exception of WD–DD pairs or when the two components lie within the error bars of each other.

class (with the obvious exception of WD–DD pairs) and the line joining the components should be parallel to the track in which the systems reside. In the case of WD–DD dwarf systems or systems that have separations comparable to the error bars in the RPM diagram, the line need not be parallel. The $r$-band RPM diagram, in Figure 2.12, confirms that the SLoWPoKES systems are associated pairs.

### 2.4.2 Separation

Despite the large number of optical companions found at larger angular separations, the final distribution of the identified pairs is mostly of pairs with small angular separations. This is shown in Figure 2.13 where, after a narrow peak at $\Delta\theta \sim 15''$, the distribution tapers off and rises gently after $\Delta\theta \gtrsim 70''$. To convert the angular separations into physical separations, we need to account for the projection effects of the binary orbit. As that information for each CPM pair is not available, we apply the statistical correction between projected separation ($s$) and true separation ($a$) determined by Fischer & Marcy (1992) from Monte Carlo simulations over a full suite of binary parameters. They found that

$$a \approx 1.26\ s = 1.26\ \Delta\theta\ d, \tag{2.15}$$

where the calculated $a$ is the physical separation including corrections for both inclination angle and eccentricity of the binary orbit and is the actual semi-major axis. We emphasize, however, that these $a$ values are valid only for ensemble comparisons and should not be taken as an accurate measure of $a$ for any individual system. In addition, the above equation implies that, at the extrema of angular separations probed, we are biased towards systems that are favorably oriented, either because of $\sin i$ projection effects or eccentricity effects that lead to a changing physical separation as a function of orbital position. For example, at $\Delta\theta \cong 7''$, pairs at their maximal apparent separation are more likely to be identified while we are biased towards pairs with smaller apparent separations at $\Delta\theta \cong 180''$.

The distribution of $a$ is plotted for the SLoWPoKES sample in Figure 2.13 (right). The semi-major axes for the identified pairs range from $\sim 10^3 - 10^5$ AU ($\sim$0.005–0.5 pc), with sharp cutoffs at both ends of the distribution, and with a clear bimodal structure in between. The cutoff at small separations is observational, resulting from our bias against angular separations $\Delta\theta < 7''$. Indeed, the range of physical separations probed by SLoWPoKES is at the tail-end of the log-normal distribution ($\langle a \rangle = 30$ AU, $\sigma_{\log a} = 1.5$) proposed by DM91 and Fischer & Marcy (1992). The cutoff we observe at the other end of the distribution, $a \sim 10^5$ AU, is likely physical. With the mean radii of prestellar cores observed to be around 0.35 pc or $10^{4.9}$ AU (Benson & Myers 1989; Clemens et al. 1991; Jessop & Ward-Thompson

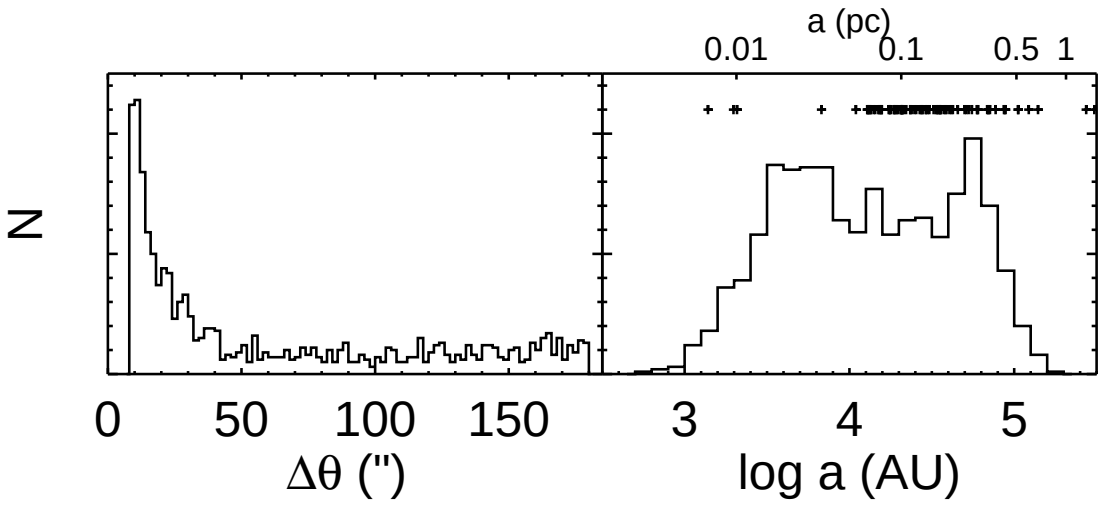


Figure 2.13: The projected angular separation (left) and the semi-major axes (right; corrected using $a = 1.26\ \theta\ d$, Fischer & Marcy 1992) for the CPM doubles identified in SLoWPoKES. The upper x-axis in the right panel shows the semi-major axis in parsecs; the widest CPM pairs known in the literature (see Table II.7) are shown as pluses at their semi-major axis values at the top of the panel. SDs were excluded from the right panel. The distribution of physical separations is clearly bimodal with a break at ∼0.1 pc.

2000), SLoWPoKES represents some of the widest binaries that can be formed. However, other studies have found binary systems at similar separations; plotted in pluses are the wide CPM pairs compiled from the literature and listed in Table II.7.

Between the cutoffs at $\sim 10^3$ AU and at $\sim 10^5$ AU, we observe a distinct bimodality in the distribution of physical separations at $a \sim 10^{4.2}$ AU (∼0.1 pc) that has no correlation with the distance to the observed system (see Section 2.5 below). We have high confidence that this bimodality is not due to some sort of bias in our sample. As discussed above, the most important observational bias affecting the distribution is the bias against pairs with $a \lesssim 10^3$ AU, because we are not sensitive to systems with $\Delta\theta < 7''$ nor to very nearby systems. In addition, given the care with which we have eliminated false positives in the sample, we have high confidence that the bimodal structure is not due to a large contamination of very wide chance pairs. Instead, it is likely that this bimodality reveals two distinct populations of wide binaries in SLoWPoKES, possibly representing systems that form and/or dissipate through differing mechanisms. We discuss the bimodality in the context of models of binary

Table II.7. A sub-sample of previously known wide binaries with the projected separation, $s$, $\gtrsim 10^4$ AU ($\sim$0.05 pc)

| ID[a] | | $\Delta\theta$ | $s$ | Spectral Type[b] | | BE[c] | References |
|---|---|---|---|---|---|---|---|
| Primary | Secondary | ($''$) | (AU) | Primary | Secondary | ($10^{40}$ ergs) | |
| HIP 38602 | LSPM J0753+5845 | 109.90 | 10175 | G8.1 | M5.1 | 132.18 | 1 |
| HIP 25278 | HIP 25220 | 707.10 | 10249 | F1.8 | K5.8 | 307.44 | 1 |
| HIP 52469 | HIP 52498 | 288.00 | 10285 | A8.9 | F9.3 | 379.74 | 1 |
| HIP 86036 | HIP 86087 | 737.90 | 10400 | F8.4 | M2.6 | 184.33 | 1 |
| HIP 58939 | LSPM J1205+1931 | 117.20 | 10558 | K0.5 | M4.7 | 107.44 | 1 |
| HIP 51669 | LSPM J1033+4722 | 164.30 | 10668 | K7.3 | M5.7 | 52.10 | 1 |
| HIP 81023 | LSPM J1633+0311N | 252.00 | 10723 | K3.2 | M3.8 | 81.51 | 1 |
| HIP 50802 | LSPM J1022+1204 | 311.90 | 11139 | K5.9 | M3.1 | 56.44 | 1 |
| HIP 78128 | LSPM J1557+0745 | 144.60 | 11385 | G7.1 | M5.0 | 123.01 | 1 |
| HIP 116106 | 2MASS J2331-04AB | 451.00 | 11900 | F8 | ··· | 161.10 | 2 |
| $\alpha$ Cen AB | NLTT 37460 | 9302.00 | 12000 | G2+K1 | M6 | 430.21 | 3 |

[a]We have tried to use HIP and NLTT identifiers, whenever they exist, for consistency.

[b]Spectral types are from the referenced papers, SIMBAD, or inferred from their $V - J$ colors using Kenyon & Hartmann (1995).

[c]Binding energies are calculated using estimated masses as a function of spectral type (Kraus & Hillenbrand 2007). When spectral type for the secondary was not available, it was assumed to be an equal-mass binary.

References. — (1) Lépine & Bongiorno (2007); (2) Caballero (2007); (3) Caballero (2009); (4) Caballero (2009); (5) Bahcall & Soneira (1981); (6) Latham et al. (1984); (7) Makarov et al. (2008); (8) Zapatero Osorio & Martín (2004); (9) Faherty et al. (2010); (10) Chanamé & Gould (2004); (11) Quinn et al. (2009); (12) Poveda et al. (2009); (13) Allen et al. (2000).

Note. — The first 10 pairs are listed here; the full version of the table is available online.

formation and kinematic evolution in Section 2.5.

### 2.4.3 Mass Distribution

Figure 2.14 (left panel) shows the $r - z$ color distributions of the primary and secondary components of SLoWPoKES pairs, where the primary is defined as the component with the bluer $r - z$ color (and, thus, presumably more massive). As the SLoWPoKES sample is dominated by dwarfs, the $r - z$ color distribution should correspond directly to the mass distribution. Both the primary and secondary distributions show a peak at the early–mid M spectral types (as inferred from their colors; Section 2.2.4.2), probably due to, at least in part, the input sample being mostly M0–M4 dwarfs. However, apart from the saturation at $r \lesssim 14$, there is no bias against finding higher-mass companions. Hence, it is notable that more than half of the primaries have inferred spectral types of M0 or later, with the distribution

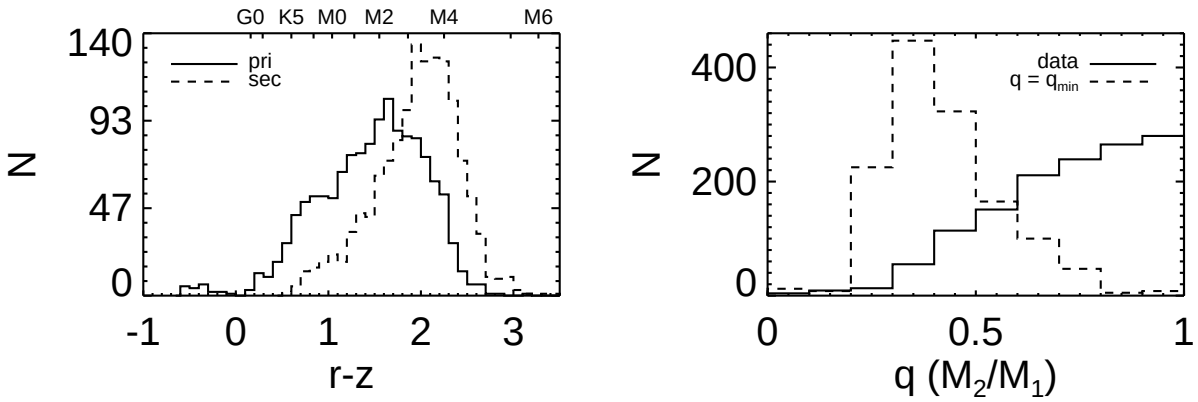


Figure 2.14: *Left*: The $r-z$ color for the primaries (solid) and secondaries (dashed). The upper x-axis, in the left panel, shows the spectral types inferred from their $r-z$ colors (Covey et al. 2007; West et al. 2008). Both distributions exhibit bimodality and are, similar to each other. *Right*: The mass ratio, $q \equiv M_2/M_1$ for SLoWPoKES pairs (solid histogram) indicates that most are in equal- or near-equal-mass systems. Within the observational limits of SDSS, we should have been able to see much more extreme mass ratio systems (dashed histogram). The lack of such systems indicates that the observed distribution is not dominated by observational biases and is probably real.

of the secondaries even more strongly skewed to later spectral types (by definition).

As discussed above, selection biases in SLoWPoKES are in general a function of distance because of the large range of distances probed (see Sec. 2.4.1; Figures 2.3 and 2.9). Thus, in Figure 2.15 we show the box-and-whisker plot of the distribution of the $r-z$ colors of the primary (blue) and secondary (red) components as a function of distance in 100 pc bins. The bar inside the box is the median of the distribution; the boxes show the inter-quartile range (defined as the range between $25^{\rm th}$ and $75^{\rm th}$ percentiles); the whiskers extend to either the 1.5 times the inter-quartile range or the maximum or the minimum value of the data, whichever is larger; and the open circles show the outliers of the distribution. The black dashed lines show the bright and faint limits of our sample ($14 \lesssim r \leq 20$). As the figure indicates the primary and secondary distributions are bluer at increasing distances, as would be expected due to the bright and faint limits; but the secondary distribution does not change as compared to the primary distribution as a function of distance. However, this is likely to be a strict function of the faintness limit of our catalog: the stellar mass function peaks around M4 spectral type (Bochanski et al. 2010) while we cannot see M4 or later stars

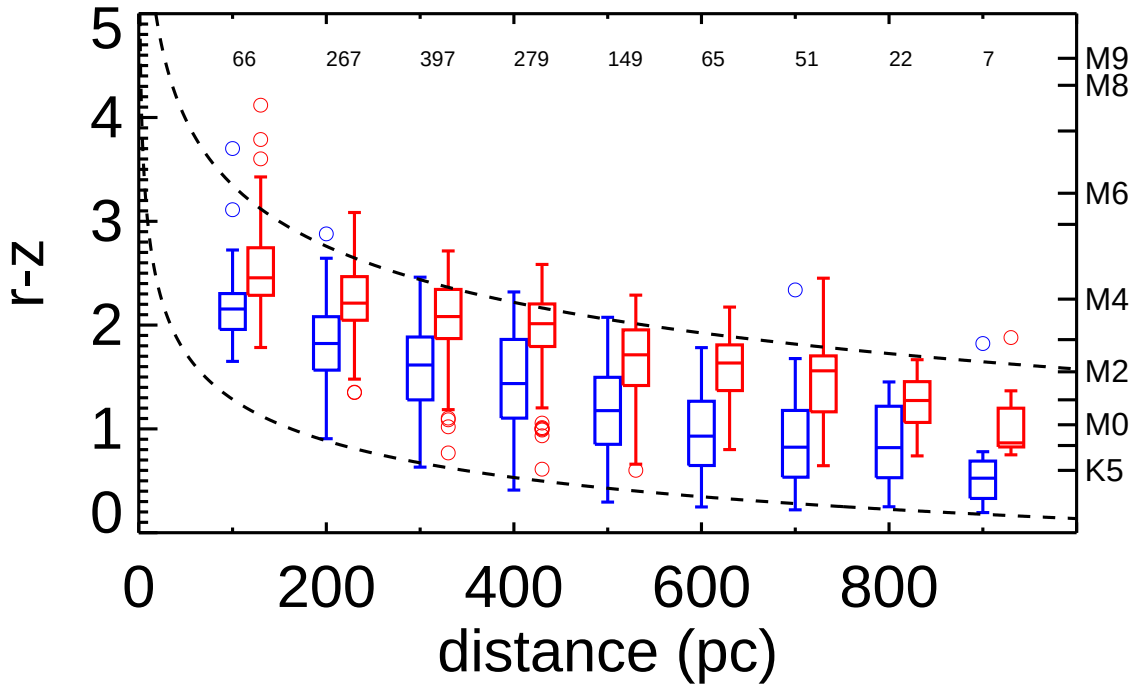


Figure 2.15: The color distribution for the primary (blue) and secondary (red) components of SLoWPoKES pairs as a function of distance, in 100 pc bins shown in a box-and-whisker plot; the number of pairs in each bin is printed along the top. The bar inside the boxes show the median of the distribution; the boxes show the inter-quartile range; the whiskers extend to either 1.5 times the inter-quartile range or the maximum or the minimum value of the data, whichever is larger; and the open circles show the outliers. The dashed lines show the magnitude limits of this catalog ($14 \lesssim r \leq 20$). The secondary distribution tracks the primary distribution at all distances.

beyond ∼400 pc. Hence, with our current sample, we cannot discern whether the tendency for the secondary distribution to follow the primary distribution is a tendency toward $q \sim 1$ or a tendency for the secondary distribution to be drawn from the field mass function.

We can also examine the distribution of the secondary masses relative to their primaries, i.e. the mass ratio distribution, which is an important parameter in the study of binary star formation and evolution. As shown in Figure 2.14 (right panel, solid histogram), the distribution of mass ratios, $q \equiv M_2/M_1$, is strongly skewed toward equal-mass pairs: 20.9%, 58.5%, 85.5% of pairs have masses within 10%, 30%, and 50%, respectively, of each other. To determine whether this is strictly due to the magnitude limits in SLoWPoKES, we calculated

the mass ratios for hypothetical pairs with the observed primary and the faintest observable secondary. The resulting distribution (dashed histogram) is considerably different from what is observed and shows that we could have identified pairs with much lower mass ratios, within the $r \leq 20$ faintness limit. The same result is obtained when we pair the observed secondaries with the brightest possible primary. Hence, we conclude that the observed distribution peaked toward equal-masses among wide, low-mass stars is real and not a result of observational biases.

### 2.4.4 Wide Binary Frequency

To measure the frequency of wide binaries among low-mass stars, we defined the wide binary frequency (WBF) as

$$\text{WBF} = \frac{\text{number of CPM pairs found}}{\text{number of stars searched around}}. \tag{2.16}$$

With 1342 CPM doubles among the 577,459 stars that we searched around, the raw WBF is 0.23%. However, given the observational biases and our restrictive selection criteria, 0.23% is a lower limit. Figure 2.16 shows the WBF distribution as a function of $r - z$ color with the primary (solid histogram), secondary (dashed histogram), and total (solid dots with binomial error bars) WBF plotted; the total number of pairs found in each bin are also shown along the top. The WBF rises from $\sim$0.23% at the bluest $r - z$ color ($\sim$K7) to $\sim$0.57% at $r - z = 1.6$ ($\sim$M2), where it plateaus. This trend is probably due at least in part to our better sensitivity to companions around nearby early–mid M dwarfs as compared to the more distant mid-K dwarfs or to the much fainter mid–late M dwarfs. To get a first-order measure of the effects of the observational biases, we can look at the WBF in specific distance ranges where all stars of the given $r - z$ colors can be seen and the biases are similar for all colors, assuming the range of observable magnitude are $r = 14$–20. In particular, it would be useful to look at $r - z = 0.7$–1.5 where the WBF increases and $r - z = 1.5$–2.5 where the WBF plateaus in Figure 2.16. Figure 2.17 shows the WBF in the two regimes for $d = 247$–1209 pc and 76–283 pc, respectively, where all companions of the given color range are expected to be detected at those distances. In the restricted ranges, the WBF

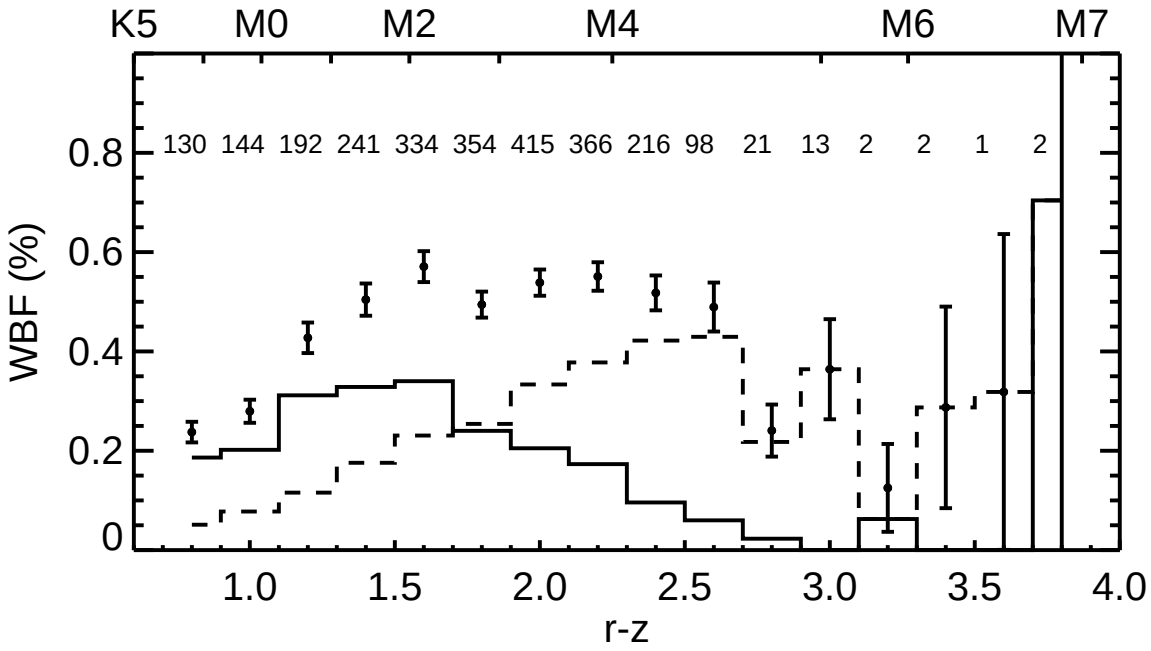


Figure 2.16: The wide binary fraction (WBF) of low-mass stars that are the primary (solid histogram) and secondary (dashed histogram) companions in wide pairs shown as a function of their $r-z$ colors, with spectral types shown along the top x-axis. The total WBF of low-mass stars in wide pairs , shown in black circles along with the binomial errors, shows a peak of $\sim 0.57\%$ for $r-z=1.6$ ($\sim$M2). The low WBF is expected due to the severe observational biases, as well as a reflection of our restrictive binary selection algorithm. The total number of CPM pairs in each bin are printed along the top.

is generally higher for a given color than in Figure 2.16, ranging between 0.44–1.1%. More importantly, neither panel reproduces the trend in WBF seen for the same color range in Figure 2.16, indicating that observational biases and incompleteness play a significant role in the observed WBF. As these two samples are pulled from two different distance ranges, some of the differences in the value of WBF as well as the observed trend in WBF as a function of $r-z$ might be due to Galactic structure or age of the sampled pairs. Hence, even the maximum observed WBF of 1.1% in SLoWPoKES is likely a lower limit on the true WBF.

SLoWPoKES should be useful for studying the WBF as a function of Galactic height ($Z$), which can be taken as a proxy for age. Figure 2.18 shows the WBF vs. $Z$, in $r-z$ color bins. Again, to keep the observational biases similar across color bins, we selected distances ranges such that CPM companions with $r-z$ colors within $\pm$ 0.3 could be seen in SDSS; for example, in the first bin ($r-z=0.7$–1.0) all companions with $r-z=0.4$–1.3 are expected

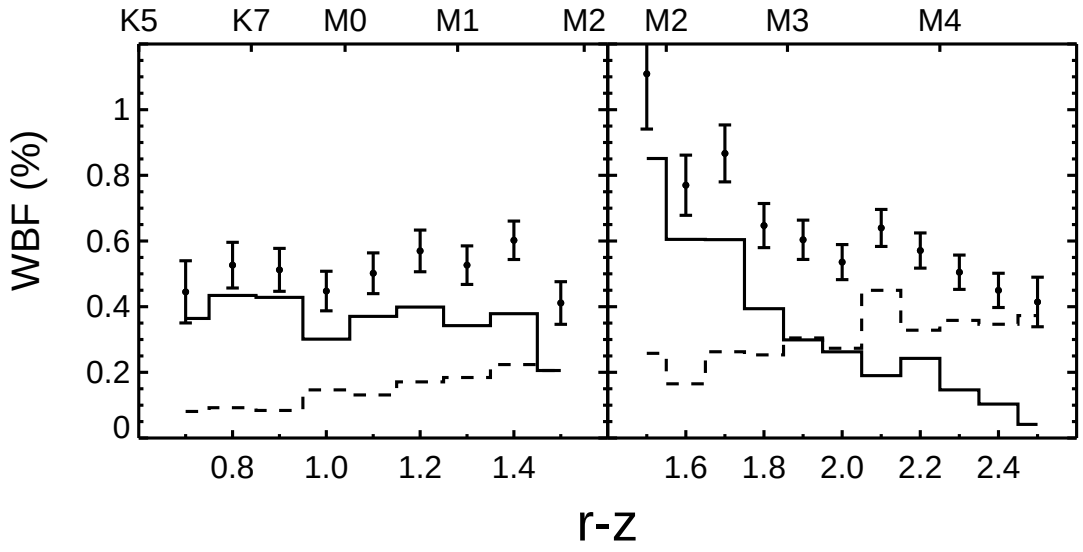


Figure 2.17: Same as Figure 2.16; but to explore the effect of biases in the WBF, we compare two color ranges: $r-z = 0.7$–$1.5$ where the WBF rises and $r-z = 1.5$–$2.6$ where it plateaus in Figure 2.16. To make the selection effects similar throughout the selected color range, we restricted the distance of the stars such that all secondaries of the given color range can be seen throughout the distance range. The WBF seen here (i) is higher than in Figure 2.16 for a given color bin and (ii) as a function of $r-z$ does not reproduce the same trend as in Figure 2.16. Since the two samples were chosen from two different distance ranges, they might also reflect differences due to the age of the sampled pairs and/or the Galactic structure at that position. These differences indicate significant observational biases and incompleteness affect our WBF determination.

to be seen. Note that this approach is biased towards equal-mass pairs, with high mass-ratio pairs never counted. Consequently, the WBF is lower than in the Figures 2.16 and 2.17, with maximum at $\sim$0.35% for $r-z = 1.3$–$1.9$; the WBF peaks at around the same color range in all three figures. However, our method ensures that we are sensitive to *all* similar mass pairs across all of the distance bins. Figure 2.18 suggests that the WBF decreases with increasing Z. As this trend appears for both primary and secondary components for almost all spectral types (colors) probed, it is likely not an artifact of observational biases and is strong evidence for the time evolution of the WBF. Wide binaries are expected to be perturbed by inhomogeneities in the Galactic potential, giant molecular clouds, and other stars and, as a result, to dissipate over time. As pairs at larger Galactic heights are older as

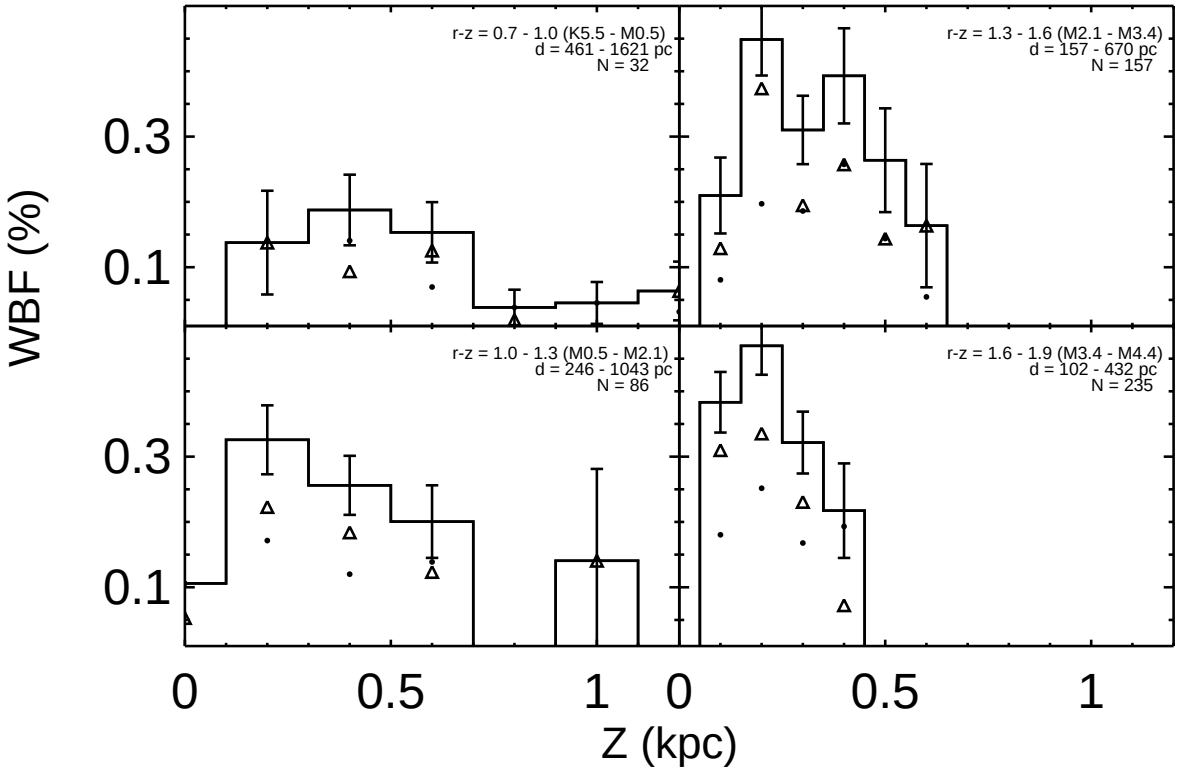


Figure 2.18: WBF, with binomial errors, decreases with Galactic height at all $r-z$ color bins for the primaries (circle), secondaries (triangle), and the total (solid histogram). In order to keep biases similar in a color bin, we selected a distance range such that all stars with $r-z$ colors within $\pm 0.3$ dex of the bin could be seen throughout the distance range. This decrease in WBF with increasing $Z$ suggests dynamical destruction of (older) pairs at larger Galactic heights.

an ensemble, it is expected that a larger fraction of pairs at larger $Z$, which are older, have dissipated.

## 2.5 Discussion

As discussed above, Sesar et al. (2008) recently conducted a search of CPM pairs in the SDSS DR and found ∼22000 wide pairs, of all spectral types, with the probability of being a real binary of ∼67% at angular separations of 5–30″. This search was done for all stars in the DR6 photometry with $\mu \geq 15$ mas yr$^{-1}$ and matched both components of proper motions within 5 mas yr$^{-1}$. As Sesar et al. (2008) note, the sample is not very efficient for

follow-up studies due to the likely large number of chance alignments (i.e. false positives). Our analysis in this chapter indicates that their low proper-motion cutoff is chief culprit for the contamination; with a higher proper-motion cutoff similar to ours, the Sesar et al. (2008) sample could in principle be sifted of many false positives. Sesar et al. (2008) used a statistical subtraction to correct the ensemble for the chance alignments, which suffices for the purpose of their work. While SLoWPoKES is intended to serve a very different purpose—namely to provide a "pure" catalog of high-fidelity systems suitable for targeted follow-up studies—it is useful to compare some of our tentative findings and interpretations with those of Sesar et al. (2008) based on their more complete sample.

For example, the upper limit of the WBF in SLoWPoKES (∼1.1%; e.g., Figures 2.17) is consistent with the 0.9% at $Z = 500$ pc from Sesar et al. (2008). This suggests that, for specific color and distance ranges, the selection biases in SLoWPoKES may not significantly affect the ability of this sample to characterize the WBF among late-type stars at the widest separations. Kraus & Hillenbrand (2009b) similarly find a WBF of at most a few percent for masses 0.012–2.5 $M_\odot$ at separations of 500–5000 AU in their study of the Taurus and Upper Sco star-forming regions. Moreover, they find that the distribution of binary separations in their sample remains flat out to the limits of their survey (∼5000 AU) for all but the lowest mass systems with $M_{tot} < 0.3$ $M_\odot$. At the same time, all of these studies fall well below the WBF (for $s > 1000$ AU) of ∼9.5% determined for solar-type *Hipparcos* stars (Lépine & Bongiorno 2007) and the 10% suggested by Longhitano & Binggeli (2010) for G5 or later stars in the solar neighborhood from SDSS DR6. Similarly, integrating the Gaussian distribution of DM91 suggests a WBF of ∼9.2% for 1000 AU $\leq a \leq 0.5$ pc and ∼0.64% for $a > 0.5$ pc for solar-type stars. Even accounting for the lower multiplicity seen in M dwarfs by Fischer & Marcy (1992), this is much higher than our result. Similarly, the decrease of WBF with increasing $Z$ in SLoWPoKES (Figure 2.18) was noted by Sesar et al. (2008) in their sample as well.

Sesar et al. (2008) had noted that the companions of red stars, unlike the bluer stars, seemed to be drawn randomly from the field stellar mass function. We do not find evidence to support that finding, but our results are probably limited by the faintness limit. With respect to the distribution of mass ratios (Figure 2.15), Reid & Gizis (1997) observed, as

we do, a strong skew towards equal-mass pairs with a peak at $q \geq 0.8$ in their 8 pc sample. However, Fischer & Marcy (1992) found a flat distribution in their sample of dMs within 20 pc. More recently, Kraus & Hillenbrand (2009b) also found that a bias towards equal-masses in their study of 0.012–2.5 $M_{\odot}$ wide binaries (500–5000 AU separations) in the Taurus and Upper-Sco star-forming regions. In contrast, solar-type field stars exhibit a definitive peak at $q \sim 0.3$ (DM91, Halbwachs et al. 2003). With the field mass function peaking around ∼M4 spectral type (Bochanski et al. 2010), a peak at $q \sim 0.3$ for solar-type stars and at $q \sim 1$ for M dwarfs are both consistent with the secondary mass function being a subset of the field mass function.

With some systems wider than ∼1 pc, SLoWPoKES provides the largest sample to date of the widest CPM doubles. However, these are not the only systems known at this separation regime; Table II.7 lists 84 systems with projected physical separations greater 0.05 pc ($\sim 10^4$ AU). This sample is biased towards pairs with at least one *Hipparcos* star, with about half of them from the CPM catalog of Lépine & Bongiorno (2007). This is not a comprehensive list of all known wide binaries; for example, the existing CPM catalogs of Luyten (1979a, 1988), Bahcall & Soneira (1981), Halbwachs (1986), and Chanamé & Gould (2004) likely contain at least a few hundred pairs in this separation range. Even among the brown dwarfs, where most known pairs have separations smaller than 15 AU, two very-wide systems—the 5100 AU 2MASS J0126555-502239 (Artigau et al. 2007, 2009) and the 6700 AU 2MASS J12583501+40130 (Radigan et al. 2009)—have already been identified. All of these wide pairs and other low-binding energy VLM systems from the VLM binary archive [9] are shown, when relevant, in Figures 2.13 and 2.20 for comparison with the SLoWPoKES distribution. Most of the CPM doubles in Table II.7 were found in nearby, high proper motion catalogs. Due to the depth of SDSS imaging and the larger distances probed, SLoWPoKES significantly increases CPM pairs with large physical separations. For the same reason, the existence of pairs as wide as $\gtrsim$ 1 pc in SLoWPoKES (Figure 2.13) should perhaps not be surprising.

At the same time, the question of how such wide, weakly bound systems survive over time and how they form in the first place is a very interesting issue that the SLoWPoKES

[9] `http://vlmbinaries.org`

sample will be well suited to address. The initial distribution of separations of wide binaries is not static over time but is modified by interactions with other stars, molecular clouds, and variations in the Galactic potential. Over the lifetime of a binary, the small and dissipative, but numerous, encounters that it undergoes with other stars is much more efficient at disrupting the system than single catastrophic encounters, which are very rare (Weinberg et al. 1987). Using the Fokker-Planck coefficients to describe the advection and diffusion of the orbital binding energy due to such small encounters over time, Weinberg et al. (1987) calculated that the average lifetime of a binary is given by:

$$t_\star(a) \approx 18 \text{ Gyr} \left(\frac{n_\star}{0.05 \text{ pc}^{-3}}\right)^{-1} \left(\frac{M_\star}{M_\odot}\right)^{-2} \left(\frac{M_{\rm tot}}{M_\odot}\right) \left(\frac{V_{\rm rel}}{20 \text{ km s}^{-1}}\right) \left(\frac{a}{0.1\text{pc}}\right)^{-1} (\ln \Lambda)^{-1} \tag{2.17}$$

where $n_\star$ and $M_\star$ are the number density and average mass of the perturbers, $V_{\rm rel}$ is the relative velocity between the binary system and the perturber, $\rm M_{tot}$ and $a$ are the total mass and semi-major axis of the binary, and $\Lambda$ is the Coulomb logarithm. Using the average Galactic disk mass density of 0.11 $\rm M_\odot$ $\rm pc^{-3}$, an average perturber mass of 0.7 $\rm M_\odot$, $V_{\rm rel}$ = 20km $\rm s^{-1}$, and $\Lambda = 1$ (see also Close et al. 2007), we can rewrite the above equation as:

$$a \simeq 1.212 \ \frac{M_{\rm tot}}{t_\star} \text{pc} \tag{2.18}$$

for $M$ in $\rm M_\odot$ and $t_\star$ in Gyrs. This describes, statistically, the widest binary that is surviving at a given age. For example, at 1 Gyr 1 $\rm M_\odot$ binaries as wide as 1.2 pc are likely to be bound, but by 10 Gyr, all systems wider than 0.12 pc will likely have been disrupted. Hence, the combination of Eq. (2.18) and the distribution of binary separation at birth may describe the current binary population of the Galaxy. Figure 2.19 shows the physical separation vs. total mass for SLoWPoKES pairs and the other known wide CPM pairs from the literature (see above); characteristic disruption timescales of 1, 2, and 10 Gyr for Eq. (2.18) are overplotted. From this, most SLoWPoKES pairs can be expected not to dissipate before 1–2 Gyr, with approximately half of the population stable enough to last longer than 10 Gyr.

Interestingly, the widest SLoWPoKES systems appear to violate previously proposed

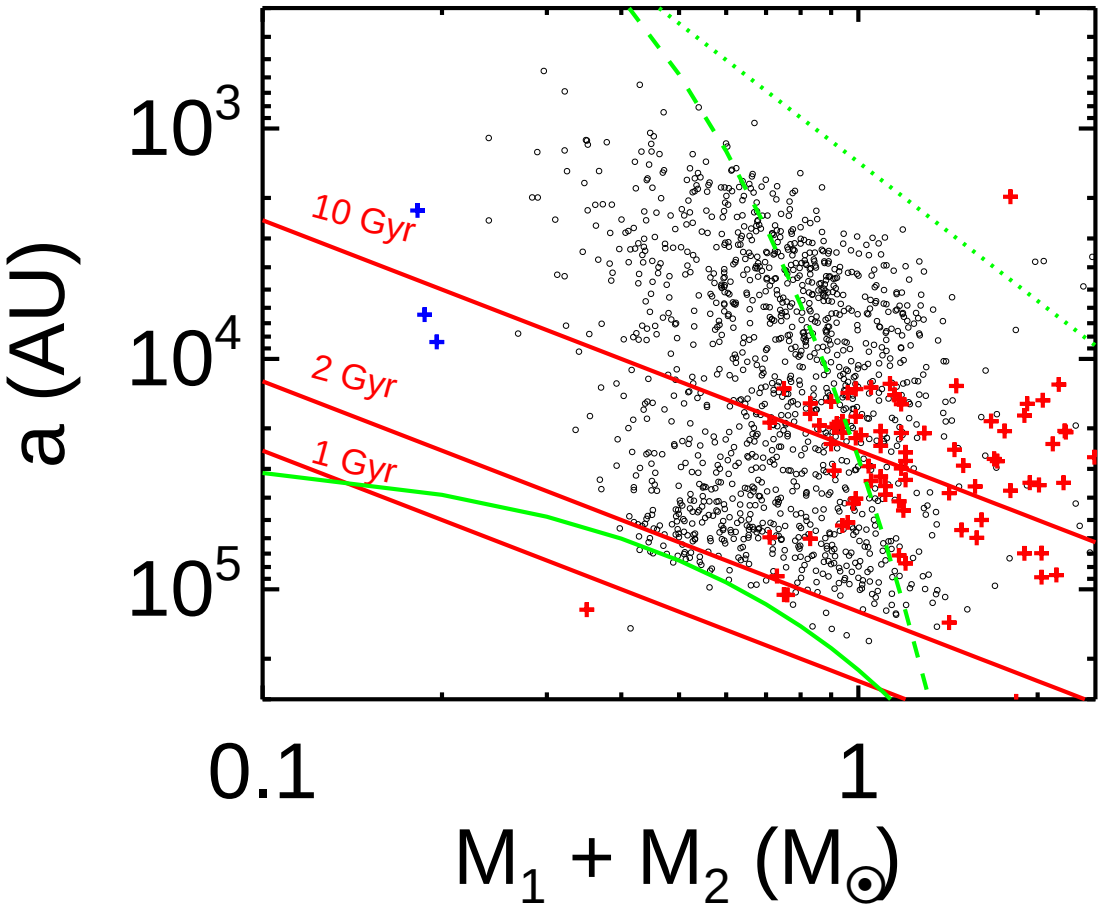


Figure 2.19: The physical separation of SLoWPoKES pairs (black circles) and previously known wide CPM doubles (red pluses; Table II.7) and VLM binaries (blue pluses) as a function of the total mass of the system, as inferred from their $r - z$ colors. Previous studies by Reid et al. (2001b) (green dashed line) and Burgasser et al. (2003b) (green dotted line) have also suggested empirical limits for stability. As neither of those describe the SLoWPoKES envelope, we have followed these previous authors and fit a log-normal (solid green line). Numerical simulations by Weinberg et al. (1987) suggest that the lifetime of wide pairs is a function of age as well; the "isochrones" show the expected $a$ vs. $M_{tot}$ relationships for dissipation times of 1, 2, and 10 Gyrs (solid red lines), as defined by Eq. (2.18). While some very wide SLoWPoKES pairs are expected to dissipate on timescales of 1–2 Gyr, most should be stable for $\gtrsim$ 10 Gyrs. All SDs are excluded from this figure.

empirical limits on maximum separations (dashed and dotted green lines in Figure 2.19; Reid et al. 2001b; Burgasser et al. 2003b). Similarly, previously proposed empirical limits based on binding energies, $10^{41}$ ergs for stellar and and $10^{42.5}$ ergs very low-mass regimes (Close et al. 2003, 2007; Burgasser et al. 2007c), are also violated by SLoWPoKES pairs as well as other known CPM doubles. This is clearly evident in Figure 2.20, where we see that the most weakly bound SLoWPoKES systems have binding energies of only $\sim 10^{40}$ ergs, comparable to the binding energy of Neptune about the Sun[10]. Faherty et al. (2010) have also noted such transgressions in their sample of wide, very low-mass CPM doubles.

It seems that previously proposed empirical limits were too restrictive as the widest and the VLM pairs that clearly violate them were not available at the time. We can follow the approach of Reid et al. (2001b) and Burgasser et al. (2003b) to fit a log-normal that forms an empirical envelope around the SLoWPoKES pairs (Figure 2.19, green solid lines). Although this new fit is not likely to define the absolute stability limit for wide pairs, the fit is notable for how well it describes the envelope.

We note that Eq. (2.18) as well as most previously proposed empirical limits have used the total mass of the system and do not take into account the mass ratio of the components. This creates a degeneracy as the binding energy is dependent on the product of masses. Instead, it may be more physical to consider the wide, low-mass pairs as a function of the product of the masses of their components—i.e., the binding energy (BE) of the system. Figure 2.20 (left panels) present the $a$ and BE vs. $M_1 \times M_2$ for the SLoWPoKES pairs. That the distribution of $a$ as a function of either sum or product of the component masses appears qualitatively similar is a manifestation of the fact that SLoWPoKES pairs tend to be equal mass (see Figure 2.14); for high-$q$ pairs there would be a more noticeable difference in these distributions.

Perhaps, of particular interest to the issue of wide binary stability, formation, and evolution is our observation of a distinctly bimodal distribution of binary separations, seen in Figure 2.20, which equates to a bimodal distribution of system binding energies as well. The break in the bimodal distribution at binding energy $\sim 10^{41.3}$ ergs is remarkable for how well

[10]SLoWPoKES systems are much more likely than the Sun–Neptune system to be disrupted by passing stars due to the binaries' larger cross-section of interaction.

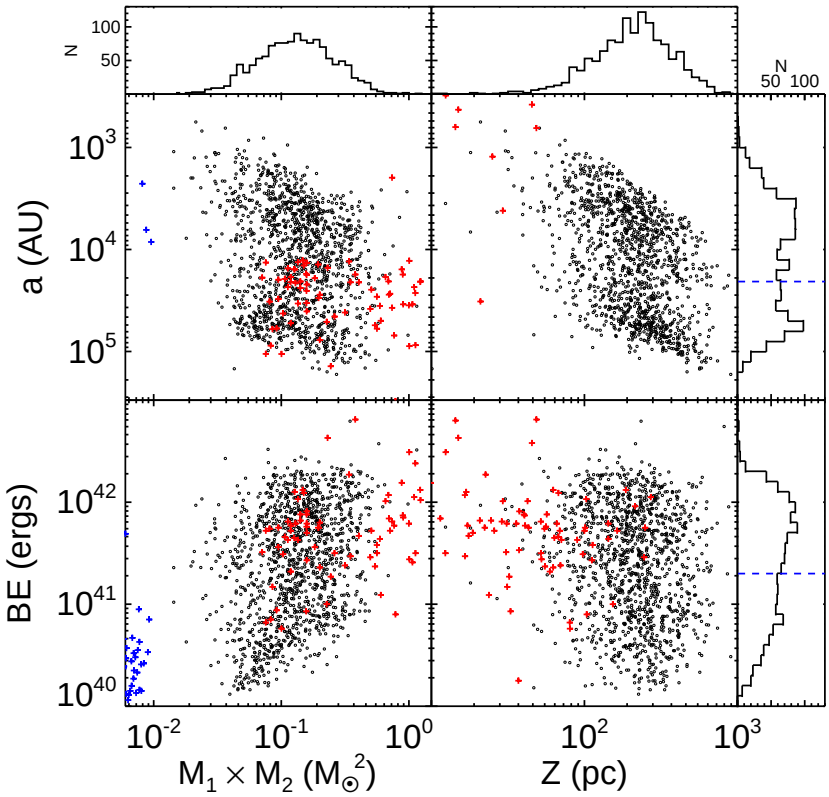


Figure 2.20: The physical separations and binding energies of SLoWPoKES pairs as a function of the product of their masses (left) or the Galactic height (right), with the histograms of the distributions shown along the top and the right. For comparison, other CPM pairs (red pluses; Table II.7) and VLM binaries (blue pluses; VLM binary archive) from the literature are shown. The bimodality in physical separation (at ∼0.1 pc) seen in Figures 2.13 and 2.19 and along the top panels in this figure is evident in binding energy as well (at $\sim 10^{41.3}$ ergs); these are marked with blue dashed lines in the histograms. As the binding energy is not dependent on $Z$, any selection effects or biases that depend directly or indirectly on $Z$ are not likely to be the cause of the bimodality. Previously suggested minimum binding energy for stellar ($10^{42.5}$ ergs) and substellar ($10^{40}$ ergs) binaries (Close et al. 2003) are violated by most SLoWPoKES as well as other CPM and VLM pairs. All SDs are excluded from this figure.

it agrees with the previously proposed empirical limit in binding energy for stellar binaries to be dynamically stable (Close et al. 2003, 2007; Burgasser et al. 2007c). In addition, as can be seen in Figure 2.19, the 10 Gyr disruption "isochrone" of Weinberg et al. (1987) nicely traces the observed break in the distribution over nearly a full decade of total system mass. The trend of the break in the distribution with mass is also important because it makes it very unlikely that the bimodality is the result of observational biases in the SLoWPoKES sample. Similarly, there is no effect of the heliocentric distances or the Galactic heights (Figure 2.20, right panels) of the pairs on the physical separation or binding energy. As discussed earlier, the principal observational biases in SLoWPoKES affect only (i) the smallest separations most severely because of the strict cut-off at $7''$ and (ii) to a lesser extent the largest separations as we limit our search to $180''$.

Thus, the bimodal distribution of binary separations suggests two populations of binaries, perhaps representing (i) systems of stars that formed with sufficient binding energy to survive for the age of the Galaxy and (ii) relatively young systems that formed within the past 1–2 Gyr but that will likely not survive much longer. Figure 2.21 shows that the dispersion in the tangential velocity is indeed smaller for the "young" population, relative to the "old" population that has had more time to get kinematically heated.[11] Quantitatively, the median absolute deviations for the two populations are 46.1 km s$^{-1}$ and 32.7 km s$^{-1}$. Curiously, the separations of the binaries in the second group (up to 1 pc; Figure 2.13, right panel) is larger than the typical sizes of prestellar cores ($\sim$0.35 pc), suggesting that these systems may not have formed via the "standard" collapse and fragmentation of individual cloud cores.

Recent N-body simulations predict bimodal distributions of wide binary separations and may provide important theoretical insight for understanding the formation and evolution of wide pairs. Although the specific simulations predict bimodality on different scales than seen in our observations, some of the resulting predicted physical properties of pairs are similar to those found in SLoWPoKES. For example, Kouwenhoven et al. (2010) find that

[11] One might expect lower mass stars to move with higher velocities relative to higher mass stars if equipartition of kinetic energy holds. However, observations have shown that the equipartition of kinetic energy does not hold and that kinematic heating is purely a function of age for field stars. Unlike in clusters, individual stars can be thought of as small, point masses when compared to the much larger Galactic potential or the giant molecular clouds that cause dynamical heating (Bochanski et al. 2007a; Schmidt et al. 2010).

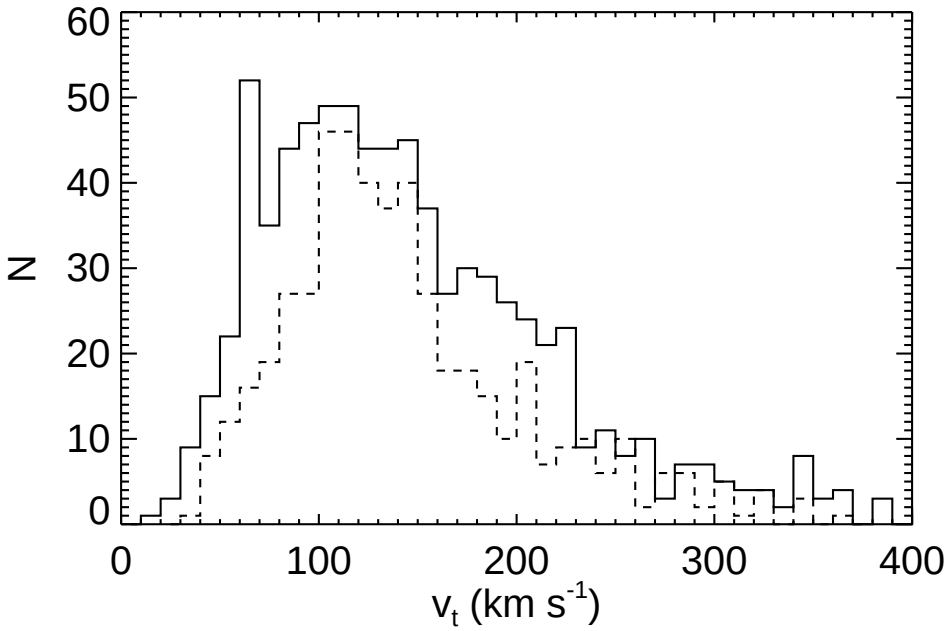


Figure 2.21: The tangential velocity ($v_t = 4.74\ \mu\ d$) distribution for the low-binding energy population (dashed histogram) and high-binding energy distribution (solid histogram), with the segregation at binding energy of $10^{41.3}$ ergs that was noticed in Figure 2.20. A smaller dispersion in the tangential velocity supports our suggestion that the low-binding energy distribution is of a younger population.

the distribution of binary semi-major axes will in general be bimodal on the size scale of star-forming clusters (i.e. $\sim 0.1$ pc), with a group of tight systems formed primarily via dynamical interactions near the cluster center and a second group of loosely bound systems formed through random pairing during the slow dissolution of the cluster. In their simulations, up to $\sim 30\%$ of the resulting binaries will be in the latter "dissolution peak", with separations of $\sim 0.1$ pc. They predict that the mass ratios of these systems will reflect random pairing. Alternatively, Jiang & Tremaine (2010) have found that a bimodal distribution arises due to the slow (as opposed to instantaneous), diffusive disruption of systems on timescales of several Gyrs, and that the details of the resulting bimodality is mostly independent of the initial distribution of separations arising from the formation process. Their simulations predict that the bimodal break in the distribution occurs at a few Jacobi radii, which corresponds to a separation of $\sim 2$ pc for a total system of 1 $M_\odot$. Perhaps the diffusive dissipation mechanism is more efficient than predicted by Jiang & Tremaine (2010), or perhaps the "tidal-tail peak"

of dissolving systems has not yet been observed. In the future, the SLoWPoKES catalog can be extended to even larger physical separations to probe this possibility.

## 2.6 Conclusions

We have created the SLoWPoKES catalog, comprising 1342 CPM binary pairs, identified through statistical matching of angular separation, photometric distances, and proper motion components. We have sifted the sample of chance alignments using a Galactic model based on empirical observations of stellar spatial and kinematic distributions. With the objective that each pair can be confidently used to investigate various science questions regarding low-mass stars, we have adopted a very restrictive set of selection criteria. This approach clearly underestimates the number of binary systems. Moreover, the sample includes several biases, the most important of which are a lack of systems with physical separations smaller than $\sim$ 1000 AU (arising from a strict bias against angular separations smaller than $7''$), and the exclusion of certain types of higher-order multiples (e.g., triples) due to the strict photometric distance matching. However, as a consequence the catalog should contain very few false positives, making follow-up studies efficient.

We built a Monte Carlo-based six-dimensional Galactic model that is able to replicate the positional and kinematic properties of the stars in the Milky Way. In its current incarnation, we used it to calculate the the number of stars within a certain spatial volume in the Galaxy and the likelihood that those stars have common kinematics (proper motions) by chance. One of the things this model underscores is how difficult it is to find two physically unassociated stars close together in space: along a typical SDSS LOS, there are expected to be only 0.52 chance alignments within $15''$ and a minuscule 0.03 chance alignments if the volume is considered. The additional matching of proper motions gives each of the accepted SLoWPoKES binaries a very low probability of being a false positive.

Due to their intrinsic faintness and the resulting small numbers, binarity studies of low-mass stars have been limited in scope. However, with the advent of large-scale deep surveys, detailed and statistically significant studies of M (and L) dwarfs are being done. SLoWPoKES is now the largest sample to date of very wide, low-mass binaries. In particular, SLoWPoKES provides a large sample of systems with physical separations up to $a \sim 1$ pc

that will be useful for putting firm constraints on the maximum size of physically associated systems. How the widest of these systems form, and how long they survive, is in particular an interesting question that SLoWPoKES is well suited to address. While numerical calculations suggest that approximately half of SLoWPoKES systems can remain bound for at least 10 Gyr (Weinberg et al. 1987), previously proposed empirical limits are violated by many SLoWPoKES systems.

Indeed, the distribution of SLoWPoKES binary separations is distinctly bimodal, suggesting the presence of (i) a population of tightly bound systems formed with sufficient binding energy to remain intact for the age of the Galaxy and (ii) a population of weakly bound systems that recently formed and that are unlikely to survive past 1–2 Gyr. Recent N-body simulations (e.g., Kouwenhoven et al. 2010; Jiang & Tremaine 2010) in fact predict a bimodal distribution of binary separations on the scales probed by the widest SLoWPoKES systems.

We observed a wide binary frequency of $\sim$1.1%, which is likely to be a minimum given the nature of our sample. While this is consistent with the results from Sesar et al. (2008) who found 0.9% of stars at $Z = 500$ pc had wide companions., it is significantly lower than $\sim$9.5% of nearby solar-type *Hipparcos* stars having wide companions (Lépine & Bongiorno 2007). While the incompleteness involved in the searching for companions at large distances probably causes some of this, both this study and Sesar et al. (2008) saw a decrease in binary fraction as a function of Galactic height, evidence of dynamical destruction of older systems. Hence, the wide binary fraction around our initial sample of low-mass stars might actually be significantly lower than the *Hipparcos* stars.

Besides the importance of SLoWPoKES for constraining models of formation and evolution of binary stars, SLoWPoKES systems are coeval laboratories—sharing an identical formation and evolutionary history without affecting each other—making them ideal for measuring and calibrating empirical relationships between rotation, activity, metallicity, age, etc. We have started programs to test and calibrate the age–activity relationship measured by West et al. (2008) and to explore whether gyrochronology (Barnes 2003, 2007) can be applied in the fully-convective regime. As coeval laboratories allow for the removal of one or more of the three fundamental parameters (mass, age, and metallicity), much more science can be

done with a large sample of such systems.

Future astrometric missions, such as SIM, should provide exquisite astrometry, perhaps enabling us to trace the orbits of some of the SLoWPoKES systems. While tracing orbits with periods $\gtrsim 10^{4-6}$ years sounds ambitious, with SIM's microarcsecond level (or better) astrometry (Shao & Nemati 2009) combined with SDSS, DSS, and/or other epochs, it is not unrealistic. Similarly, the "identical" twins in SLoWPoKES would be ideal sites to probe for the presence and differences in the formation mechanism of planets. As each identical twin in a CPM double provides similar environment for the formation and evolution of planets, these systems can be ideal sites to study planetary statistics. Due to their large separations the stars are not expected to influence each others evolution but have similar mass, age, and metallicity, as we noted earlier in Section 2.1.

The SLoWPoKES catalog, as the name suggests, only contains systems for which kinematic information is available. We can, however, use the results from the Galactic model to identify pairs at the small separations ($\Delta\theta < 7''$), albeit with a larger uncertainty, for which no kinematic information is available. Similarly companions which are fainter than $r = 20$ can also be identified as the SDSS photometry is complete to $r = 22.5$. The latter systems are likely to be skewed towards late-type dMs and unequal-mass pairs. A follow-up paper will study such systems and will add a large proportion of wide systems.

CHAPTER III

# RESOLVED SPECTROSCOPY OF M DWARF/L DWARF BINARIES. IV. DISCOVERY OF AN M9+L6 BINARY SEPARATED BY OVER 100 AU

The bulk of this chapter was published in the *The Astronomical Journal* as Dhital, Burgasser, Looper, & Stassun (2011, 141:7); the American Astronomical Society holds the copyright for the article.

This chapter reports the discovery of a faint L6±1 companion to the previously known M9 dwarf, 2MASS J01303563−4445411, at a projected physical separation of 130±50 AU, making it one of the widest VLM field multiples containing a brown dwarf companion. 2MASS J0130−4445 is only one of ten wide VLM pairs and only one of six in the field. The model-dependent masses and binding energies suggest that this system is unlikely to have formed via dynamical ejection, which is believed to the dominant mode of brown dwarf formation. Instead, 2MASS J0130−4445 and other such wide binaries are likely to have formed from their own molecular clouds. Such wide systems are very important in identifying and constraining different modes of VLM star formation and evolution. Moreover, the age, composition, and separation of the 2MASS J01303563−4445411 system make it useful for tests of condensate cloud formation in L dwarfs.

## 3.1 Introduction

The processes by which very low-mass (VLM; M $\lesssim$0.1 $M_\odot$, Burgasser et al. 2007c) stars and brown dwarfs (BD) form, and whether these processes are similar to those of higher-mass stars, is an open question. The VLMs/BDs exhibit significant differences in the distribution of binary/multiple systems when compared to their more massive brethren. The resolved binary fraction of ∼20–30% in VLMs/BDs (Basri & Reiners 2006; Joergens 2008) is significantly lower than in F and G dwarfs (∼60%; DM91) and modestly lower than M dwarfs (∼27–42%; Fischer & Marcy 1992; Reid & Gizis 1997). The typical orbital separation of ∼4–5 AU in VLMs/BDs is much smaller compared to ∼30 AU for F, G, and M dwarf bi-

naries (DM91; Fischer & Marcy 1992). In addition, while stellar binaries are known to have separations in excess of ∼1 pc (e.g., Lépine & Bongiorno 2007; Dhital et al. 2010), no VLM system has a separation greater than 6700 AU. Indeed, only 15 of the known 99 VLM systems have projected physical separations larger than 20 AU and only nine systems are wider than 100 AU[1]. Energetically, the VLM binaries seem to stand apart as well: based on empirical data, Close et al. (2003) suggested minimum binding energies of $10^{42.5}$ erg for field VLM systems, ∼300 times higher than the $10^{40}$ erg limit for stellar binary systems. Lastly, most VLM binaries are close to equal-mass. All of these differences indicate that the same formation process(es) may not be responsible for the two populations.

It is now generally believed that most stars form in multiple systems via fragmentation of the protostellar cloud, with single stars being the result of decay of unstable multiples (e.g., Kroupa 1995). The most favored process is gravoturbulence where the fragmentation is the result of a combination of turbulent gas flows and gravity. Hydrodynamical simulations have shown that when turbulent gas flows in protostellar clouds collide, they form clumps that are gravitationally unstable and, hence, collapse forming multiple stellar embryos (e.g., Caselli et al. 2002; Goodwin et al. 2004a,b; Bate 2009). Within a few freefall times, most of these embryos are ejected due to mutual dynamical interactions, preferentially the ones with lower masses.

To then explain the observed distributions of VLM binaries separations, two explanations have been proffered. The first so-called "ejection hypothesis" suggests that most VLM binaries, unlike the more-massive stellar systems, are the result of the ejected embryos (Reipurth & Clarke 2001). The wider systems get disrupted, explaining the overall rarity of VLM and BD binaries. The second is preferential accretion within the first 0.1 Myr (∼1 freefall time), making VLM systems tighter and more equal-mass. As a result, even VLM distributions that initially may have looked similar to that of higher mass stars are transformed and look like the observed VLM distributions (Bate 2009). However, neither hypothesis explains why ∼10% of observed VLM binaries are wider than 100 AU. Two other theories on VLM/BD formation, disk fragmentation (e.g., Watkins et al. 1998a,b) and photoablation (Whitworth & Zinnecker 2004), require massive stars to trigger the process and cannot explain the ex-

[1]VLM Binaries Archive (`http://vlmbinaries.org/`) and references therein.

istence of VLM binaries in the field. To resolve the differences between observational and numerical results and to distinguish between the various formation scenarios, a larger sample of VLM binaries—especially very wide systems that are most susceptible to dynamical effects—is needed.

In this chapter, we report the discovery of a wide VLM binary 2MASS J01303563−4445411 (hereafter 2MASS J0130−4445) separated by 130 AU, 3.″3. The brighter primary component of 2MASS J0130−4445 was identified by Reid et al. (2008) in the Two Micron All Sky Survey (2MASS; Skrutskie et al. 2006) and classified as an M9 dwarf on the Kirkpatrick et al. (1999) red optical scheme, indicating a spectrophotometric distance of 33.1±2.2 pc. Neither H$\alpha$ nor Li 1, activity and age indicators, respectively, were evident in the optical spectrum. The primary has a proper motion of (120±14, -25±20) mas yr$^{-1}$and a tangential velocity of 19±3 km s$^{-1}$(Faherty et al. 2009). The system is unresolved in 2MASS, and there have been no reports of a faint companion to this source in either optical survey data or follow-up observations (Reid et al. 2008; Faherty et al. 2009).

In our own follow-up observations of 2MASS J0130−4445, we have identified a well-separated, faint L dwarf companion, indicating that this is a wide VLM binary system with a probable BD component. In Sections 3.2 and 3.3, we describe our imaging and spectroscopic observations, respectively, and discuss the properties of the components of the resolved binary system. We discuss the physical association, mass, and age of the binary 2MASS J0130−4445AB in Section 3.4 and its implications on VLM formation and evolution scenarios in Section 3.5. The conclusions are presented in Section 3.6.

## 3.2 Near-Infrared Imaging

### 3.2.1 Observations and Data Reduction

2MASS J0130−4445 was imaged with the 3m NASA Infrared Telescope Facility (IRTF) SpeX spectrograph (Rayner et al. 2003) on December 7, 2009 (UT), as part of a program to identify unresolved M/L dwarf plus T dwarf spectral binaries (e.g., Burgasser et al. 2008). Conditions were clear but with poor seeing, 1.″2 at $K$-band, due in part to the large airmass of the observation (2.34–2.37). These images revealed a faint point source due east of the

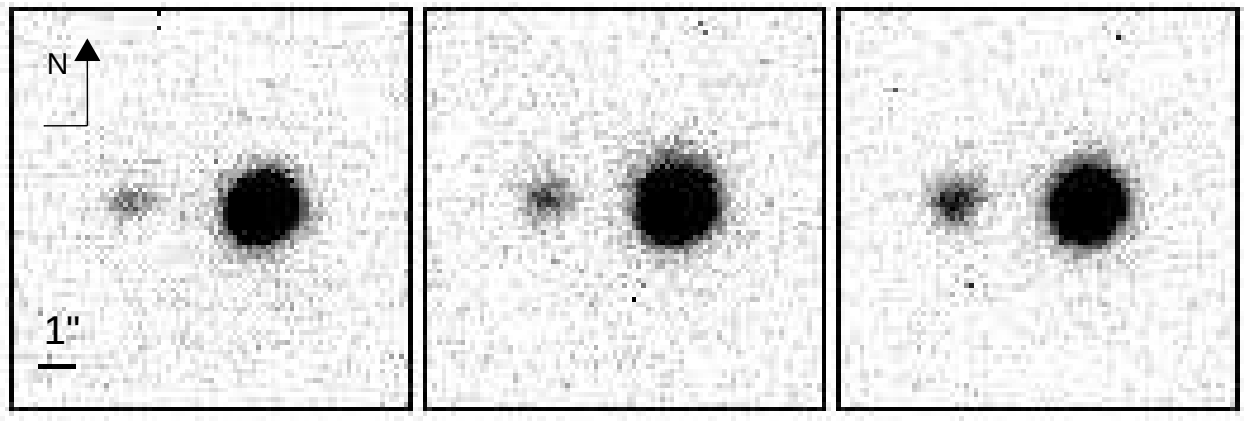


Figure 3.1: Combined SpeX images of 2MASS J0130−4445AB in the $J$-, $H$- and $K$-bands (left to right), showing the $10''\times10''$ (83×83 pixel) region around both sources. Images are aligned with north up and east to the left.

primary target at a separation of roughly $3''$. Four dithered exposures were obtained of the pair in each of the MKO[2] $J$, $H$, and $K$ filters, with individual exposure times of 45s, 30s, and 30s, respectively. The field rotator was aligned at a position angle of 0°; i.e., north up and east to the left.

Imaging data were reduced in a standard manner using custom IDL routines. Raw images were mirror-flipped about the y-axis to reproduce the sky orientation and pair-wise subtracted to remove sky contributions. The difference images were divided by normalized flat field frames, constructed by median-combining the imaging data for each filter after masking out the sources. Subsections of each image, $10''$ (83 pixels) on a side and centered on the target source, were extracted from these calibrated frames. A final image for each filter/target pair (Figure 3.1) was produced by averaging the registered subframes together, rejecting $5\sigma$ pixel outliers. The two sources of 2MASS J0130−4445 are well resolved along a nearly east-west axis. The brighter western component is hereafter referred to as 2MASS J0130−4445A and the eastern component as 2MASS J0130−4445B.

[2]Mauna Kea Observatory filter system; see Tokunaga et al. (2002) and Simons & Tokunaga (2002).

### 3.2.2 Analysis

Component magnitudes and the angular separation of the 2MASS J0130−4445 pair were determined through point spread function (PSF) fits to the reduced imaging data, following the prescription described in McElwain & Burgasser (2006). The PSF models were derived from Gaussian fits to the primary component in the individual subimage frames. For each filter, four distinct PSF models were produced, each of which were fit to the individual images, resulting in a total of 16 independent measures of the relative component magnitudes and 48 independent measures of the separation and orientation of the pair, in each of the $JHK$ filters. However, as the secondary was undetected in one of the four $J$-band images, four measures of the relative $J$-band flux and separation were discarded before computing mean values and standard deviations. Separation measurements were converted from pixels to arcseconds assuming a plate scale of $0\farcs120\pm0\farcs002$ pixel$^{-1}$ (J. Rayner, 2005, private communication) and no distortion. The position angle (set at 0°) was assumed to be accurate to within $0\fdg25$ (ibid.).

Results are listed in Table III.1. The angular separation of the pair was measured to be $3\farcs282\pm0\farcs047$ at a position angle of $87\fdg3\pm0\fdg9$; i.e., along an east-west line. The secondary is both considerably fainter and significantly redder than the primary. We derived relative magnitudes of $\Delta J = 3.11\pm0.06$ and $\Delta K = 2.34\pm0.04$. Using the combined-light 2MASS photometry for the system[3], this translates into $J - K_s$ colors of 1.13±0.04 and 1.94±0.08 for the primary and secondary, respectively.

## 3.3 Near-Infrared Spectroscopy

### 3.3.1 Observations and Data Reduction

The two components of 2MASS J0130−4445 were observed on separate nights with the prism-dispersed mode of SpeX, the primary on December 7, 2009 (the same night as the imaging observations) and the secondary on December 28, 2009 (UT). Conditions on the latter night were clear with a stable seeing of $0\farcs6$ at $K$-band. The SpeX prism mode pro-

[3]We included small corrections to the relative magnitudes in converting from the MKO to 2MASS photometric systems: 0.009, -0.006, and -0.003 mag in the $J$, $H$, and $K/K_s$ bands, respectively, calculated directly from the spectral data.

Table III.1. Results of PSF Fitting

| Parameter | Value |
|---|---|
| $\Delta\alpha \cos\delta$ ($''$)[a] | 3.28±0.05 |
| $\Delta\delta$ ($''$)[a] | 0.15±0.06 |
| Apparent Separation ($''$) | 3.28±0.05 |
| Position Angle ($^\circ$)[a] | 87.3±0.9 |
| $\Delta J$ (mag) | 3.11±0.06 |
| $\Delta H$ (mag) | 2.68±0.11 |
| $\Delta K$ (mag) | 2.34±0.04 |

[a]Measured from the brighter primary to the fainter secondary.

vides 0.75–2.5 $\mu$m continuous spectroscopy with resolution $\lambda/\Delta\lambda \approx 120$ for the $0\farcs5$ slit employed (dispersion across the chip is 20–30 Å pixel$^{-1}$). Both components were observed separately, with the slit oriented north-south, roughly aligned with the parallactic angle and perpendicular to the separation axis. For the primary, eight exposures of 90s each were obtained at an average airmass of 2.33, while guiding on spillover light from the slit. For the secondary, eight exposures of 150s each were obtained at an average airmass of 2.34, while guiding on the primary off-slit. For both sources, the A0 V star HD 8977 was observed immediately before the target for telluric and flux calibration while the quartz and Ar arc lamps were observed for flat field and wavelength calibration, respectively. Data were reduced using the SpeXtool package, version 3.4 (Vacca et al. 2003; Cushing et al. 2004) using standard settings; see Burgasser et al. (2007b) for details.

### 3.3.2 Analysis

Figure 3.2 shows the spectra of the two components of 2MASS J0130−4445AB; signal-to-noise at the $JHK$ flux peaks was 100–150 and 25–35 for the A and B components, respectively. Both spectra show the characteristic near-infrared (NIR) features of late-type

M and L dwarfs (e.g., Reid et al. 2001a; McLean et al. 2003; Cushing et al. 2005): steep red optical slopes (0.8–1.0 $\mu$m) from the pressure broadened wing of the 0.77 $\mu$m K 1 doublet; molecular absorption bands arising from $H_2O$ (1.4 and 1.9 $\mu$m), CO (2.3 $\mu$m), and FeH (0.99 $\mu$m); and an overall red spectral energy distribution (SED), consistent with the photometric colors. 2MASS J0130−4445A also exhibits additional absorption features in the 0.8–1.2 $\mu$m region arising from TiO, VO, FeH, and unresolved K 1 and Na 1 lines, all typical for a late-type M dwarf. The corresponding region in the spectrum of 2MASS J0130−4445B is considerably smoother, albeit more noisy, suggesting that many of these gaseous species have condensed out (e.g., Tsuji et al. 1998; Ackerman & Marley 2001). The appearance of weak $H_2O$ absorption at 1.15 $\mu$m and the very red SED of the NIR spectrum all indicate that 2MASS J0130−4445B is a mid- to late-type L dwarf with relatively thick condensate clouds at the photosphere.

To determine spectral types we compared our NIR spectra of 2MASS J0130−4445AB with 463 spectra of 439 M7 or later dwarfs from the SpeX Prism Spectral Libraries[4]. All templates wre chosen to have median S/N > 10 and could not be binaries, giants, subdwarfs, or spectral classifications that were peculiar or uncertain. Best matches were determined by finding the minimum $\chi^2$ deviation between component spectra and templates in the 0.95–1.35, 1.45–1.80, and 2.00–2.35 $\mu$m regions (i.e., avoiding telluric bands), following the procedure of Cushing et al. (2008) with no pixel weighting. The two best matching templates to both components of 2MASS J0130−4445AB are shown in Figure 3.3. For 2MASS J0130−4445A, these are the optically classified M8 dwarf 2MASS J05173729−3348593 (Cruz et al. 2003) and L0 dwarf DENIS–P J0652197−253450 (Phan-Bao et al. 2008); for 2MASS J0130−4445B these are the optically classified L5 dwarf 2MASSW J1326201−272937 (Gizis 2002) and L7 dwarf 2MASS J03185403−3421292 (Kirkpatrick et al. 2008). Note that despite the differences in optical type, these spectra provide equivalently good fits—the two fits were different only by 1.7$\sigma$ for the primary and 1.1$\sigma$ for the secondary based on the F-test which gauges whether two different fits to data are significantly distinct based on the ratio of $\chi^2$ values and degrees of freedom (Burgasser et al. 2010)—to the components of 2MASS J0130−4445AB, a reflection of the discrepancies between optical and NIR spectral morphologies for late-type

[4]`http://browndwarfs.org/spexprism/`

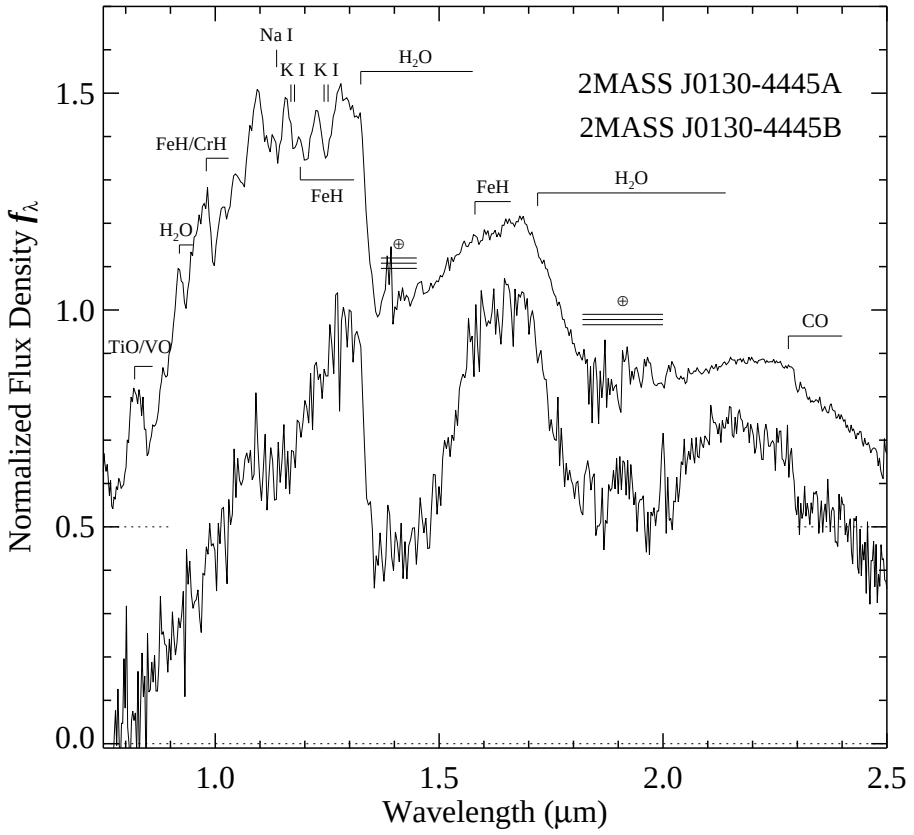


Figure 3.2: NIR spectra of 2MASS J0130−4445A (top) and 2MASS J0130−4445B (bottom) obtained with IRTF/SpeX. Data are normalized at the peak of each spectra, and the spectrum for 2MASS J0130−4445A is vertically offset by 0.5 dex for clarity (dotted lines). NIR spectral features are labeled.

M and L dwarfs (e.g., Geballe et al. 2002; Kirkpatrick 2005). A $\chi^2$ weighted mean of all the SpeX templates (e.g., Burgasser et al. 2010) indicates component types of M9.0±0.5 for 2MASS J0130−4445A and L6±1 for 2MASS J0130−4445B.

We also derived classifications using a suite of spectral indices and spectral index/spectral type relations from Tokunaga & Kobayashi (1999), Reid et al. (2001a), Geballe et al. (2002), Burgasser et al. (2006), and Burgasser (2007). Table III.2 shows the measured values and the inferred spectral subtypes of 2MASS J0130−4445A and 2MASS J0130−4445B for each of the indices. The mean and scatter from these indices yields classifications of L0.5±1.0 for 2MASS J0130−4445A and L7.0±1.5 for 2MASS J0130−4445B. These are consistent with,

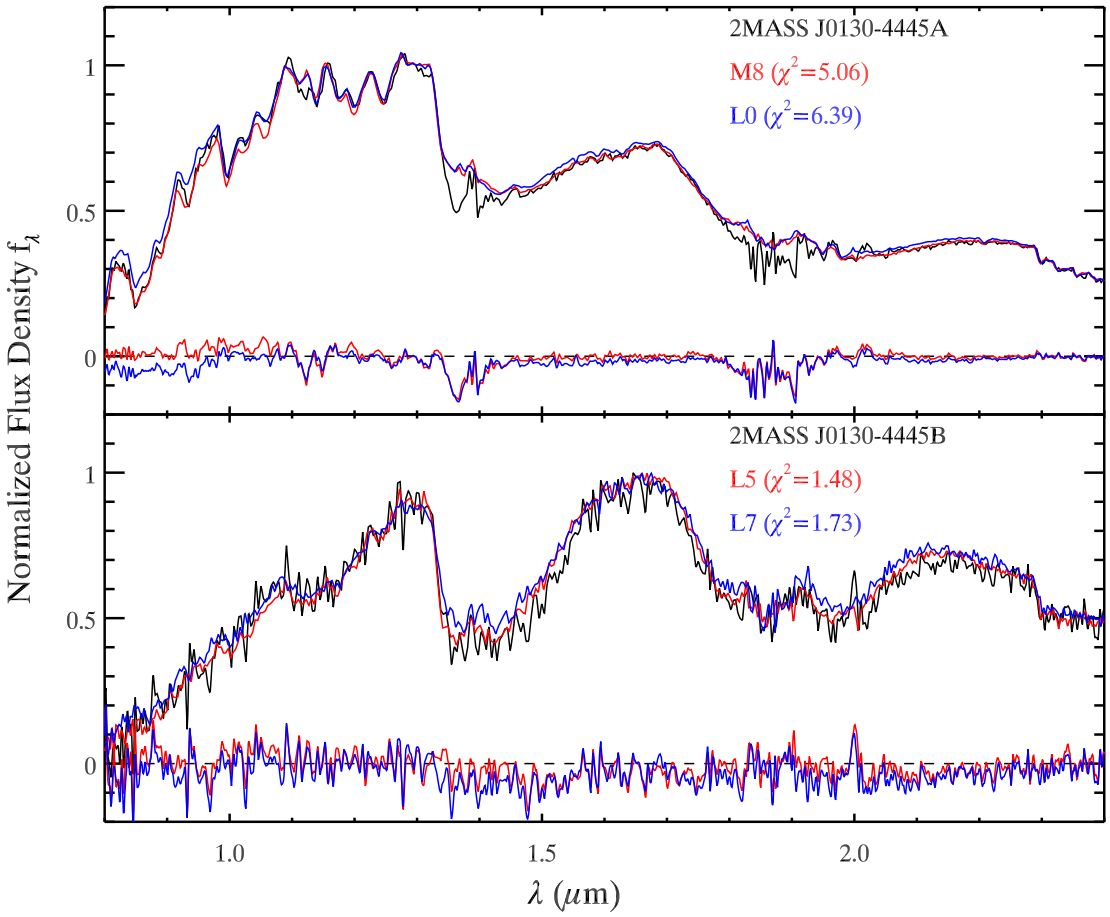


Figure 3.3: The spectral types for 2MASS J0130−4445AB as determined by matching their spectra with templates from the SpeX Prism Spectral Libraries. The best matches for 2MASS J0130−4445A were 2MASS J05173729−3348593 (optically classified M8; Cruz et al. 2003; Schmidt et al. 2007) and DENIS−P J0652197−253450 (optically classified L0; Phan-Bao et al. 2008) while 2MASSW J1326201−272937 (optically classified L5; Gizis 2002) and 2MASS J03185403−3421292 (optically classified L7; Kirkpatrick et al. 2008) were the best matches for 2MASS J0130−4445B. SpeX data for the templates are from Burgasser et al. (2010) and A. J. Burgasser et al. (in preparation). A $\chi^2$ weighted mean of all the best fit templates gives spectral types of M9.0±0.5 and L6±1 for the two components, respectively. The residuals of the comparison (target − spectral type templates) are shown at the bottom of each panel.

but less precise than, the types inferred from spectral template matching, so we adopt the latter for our subsequent analysis.

Table III.2. Near-Infrared Spectral Indices

| Index | 2MASS J0130−4445A | | 2MASS J0130−4445B | | Reference |
|---|---|---|---|---|---|
| | Value | SpT | Value | SpT | |
| $H_2O$-J | 0.954 | L0.3 | 0.706 | L7.1 | 1, 2 |
| $H_2O$-H | 0.876 | M9.6 | 0.649 | L8.3 | 1, 2 |
| $H_2O$-A | 0.686 | L1.4 | 0.602 | L4.1 | 3 |
| $H_2O$-B | 0.818 | L0.3 | 0.517 | L7.8 | 3 |
| $H_2O$-1.5 $\mu$m[a] | 1.216 | M9.8 | 1.882 | L9.0 | 4 |
| $CH_4$-K | 1.056 | L2.1 | 0.968 | L5.5 | 1, 2 |
| $CH_4$-2.2 $\mu$m[b] | ··· | ··· | 1.033 | L5.7 | 4 |
| K1[c] | 0.069 | M8.7 | ··· | ··· | 3, 5 |
| Average SpT | | L0.5±1.0 | | L7.0±1.5 | |

References. — (1) Burgasser et al. (2006); (2) Burgasser (2007); (3) Reid et al. (2001a); (4) Geballe et al. (2002); (5) Tokunaga & Kobayashi (1999)

[a]The index $H_2O$-1.5 $\mu$m is well-defined only for spectral types L0 or later.

[b]The index $CH_4$-2.2 $\mu$m is well-defined only for spectral types L3 or later.

[c]The index K1 is well-defined only up to spectral types earlier than L6.

## 3.4 System Properties

### 3.4.1 Is 2MASS J0130−4445 A Physical Binary?

To assess whether two stars comprise a physical binary or are just a chance alignment of random stars, the most reliable method used is to check for a common systemic velocity. However, 2MASS J0130−4445B is very faint, even in the infrared, and has not been detected in any earlier epoch; hence, we do not have proper motions for the secondary nor radial velocities for either component. In the absence of kinematic information, we employed two other tests to examine whether 2MASS J0130−4445AB is a physical pair: (1) the

heliocentric distances of the two components and (2) the probability that the sources are a chance alignment based on the surface distribution of stars on the sky.

The spectrophotometric distances to each component of 2MASS J0130−4445AB were derived using the $M_J$/spectral type relations from Cruz et al. (2003) based on the combined-light 2MASS photometry and our relative SpeX photometry (Table III.3). The derived distances are 34.5±3.2 pc for the primary and 45.8±13.6 pc for the secondary, where the errors are from the uncertainties in the NIR spectral types (see Sec. 3.3.2). These distances are consistent with each other within their associated errors.

Next, we calculated the probability that 2MASS J0130−4445AB is a random chance alignment along our line-of-sight based on its three-dimensional position in the Galaxy. We followed Dhital et al. (2010), constructing a three-component Galactic model with the thin disk, thick disk, and halo, constrained with empirical stellar density profiles (Jurić et al. 2008; Bochanski et al. 2010). The model recreates a $30' \times 30'$ region in the sky, centered around the coordinates of the given binary system, and out to heliocentric distances of 2500 pc. As all the simulated stars are single and non-associated, any visual binary is a random chance alignment. In $10^7$ Monte Carlo realizations, we found, on average, 0.0285 chance alignments per realization on the sky, within the $3\farcs3$ angular separation of 2MASS J0130−4445AB. More importantly, none of these chance alignments were within the range of spectrophotometric distances (40±14 pc) estimated for 2MASS J0130−4445AB. As such, we conservatively infer a $\lesssim 10^{-7}$ probability of positional coincidence. We therefore conclude that 2MASS J0130−4445AB is a physically-bound binary and not a chance alignment of two unassociated stars.

### 3.4.2 Age & Mass Estimates for 2MASS J0130−4445AB

The NIR spectral types of 2MASS J0130−4445A and 2MASS J0130−4445B correspond to effective temperatures, $T_{eff}$, of 2400±110 K and 1450±100 K, respectively, based on the $T_{eff}$/spectral type relation of Stephens et al. (2009). Uncertainties include scatter in the $T_{eff}$ relation and uncertainties in the classifications (Sec. 3.3.2) added in quadrature. Figure 3.4 shows the Burrows et al. (1993, 1997) evolutionary models, displaying $T_{eff}$ as a function of mass and age; the Burrows mass tracks and the observed $T_{eff}$ ranges are shown as dotted and

Table III.3. Properties of 2MASS J01303563−4445411AB

| Parameter | 2MASS J0130-4445A | 2MASS J0130-4445B | Reference |
|---|---|---|---|
| Optical Spectral Type | M9 | ··· | 1 |
| NIR Spectral Type | M9.0±0.5 | L6±1 | 2 |
| $J$ (mag)[a] | 14.12±0.03 | 17.28±0.06 | 2,3 |
| $H$ (mag)[a] | 13.48±0.03 | 16.13±0.10 | 2,3 |
| $K_s$ (mag)[a] | 12.99±0.03 | 15.34±0.05 | 2,3 |
| $J - K_s$ [a] | 1.13±0.04 | 1.94±0.08 | 2,3 |
| Est. $T_{eff}$ (K)[b] | 2400±110 | 1450±100 | 4 |
| Est. Distance (pc) [c] | 35±3 | 46±14 | 2,5 |
| Projected Separation (AU) [d] | 130±50 | | 1,2 |
| $V_{tan}$ (km s$^{-1}$)[d] | 23±6 | | 2,6 |

[a]Calculated using our relative magnitudes and the combined-light 2MASS photometry for the system.

[b]Reported uncertainties include scatter in the $T_{eff}$/spectral type relation of Looper et al. (2008a) relation and uncertainties in the component classifications (±0.5 subtypes).

[c]Based on the $M_J$/spectral type relation of Cruz et al. (2003); uncertainties include photometric uncertainties and scatter in the Cruz et al. relation.

[d]Based on the average distance of 40±14 pc.

References. — (1) Reid et al. (2008); (2) This study; (3) 2MASS (Cutri et al. 2003); (4) Stephens et al. (2009); (5) Cruz et al. (2003); (6) Faherty et al. (2009).

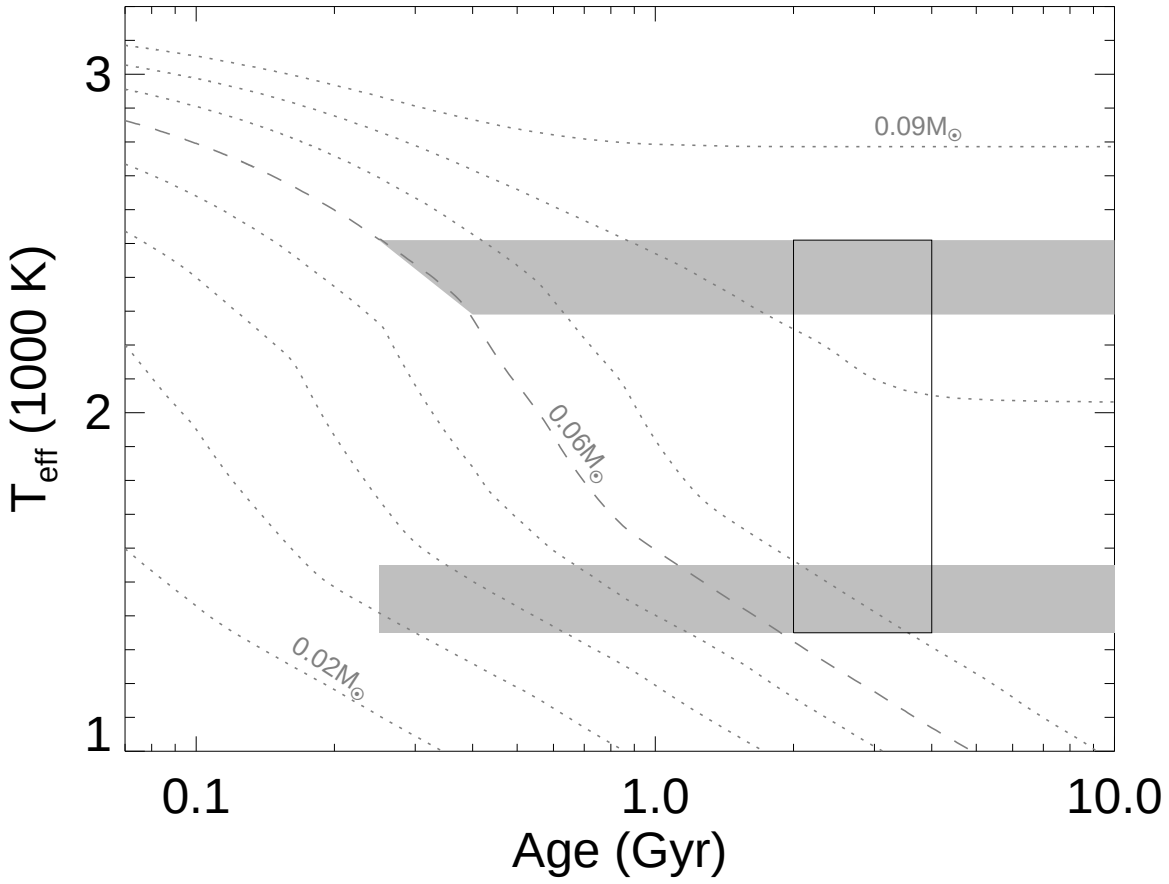


Figure 3.4: $T_{eff}$ versus age for VLM stars and BDs based on the evolutionary models of Burrows et al. (1997). Tracks for masses of 0.02–0.09 $M_\odot$ in 0.01 $M_\odot$ steps are shown as dotted lines while the LDB limit of 0.06 $M_\odot$ is shown as a dashed line. The locus defined by this lower limit on age and $T_{eff}$ derived from their spectral types is shown in gray for both components. The solid rectangle shows the age estimate of 2–4 Gyr based on the kinematics of Faherty et al. (2009). Note that the broad range of possible ages for this system allow a wide range of mass ratios, from 0.6 to 0.9.

dashed lines and gray boxes, respectively. As the masses of the two components vary quite a bit with assumed age, it is imperative to constrain the age of 2MASS J0130−4445AB.

The absence of Li 1 in 2MASS J0130−4445A indicates that it is more massive than the predicted lithium depletion boundary (LDB) mass, ∼0.06 $M_\odot$ (Chabrier et al. 1996; Burrows et al. 2001) for field stars of solar metallicity. Using the $T_{eff}$ for the primary based on its spectral type (including uncertainties) and assuming a mass $\gtrsim$0.06 $M_\odot$, the evolutionary models of Burrows et al. (1997) indicate an age $\gtrsim$250 Myr (Figure 3.4). We note that recent

work by Baraffe & Chabrier (2010) has suggested that episodic accretion during the PMS stages causes central temperature of a star to increase up to 1 dex, with a sharp dependence on the frequency and magnitude of the episodic accretion. This serves to deplete Li 1 earlier than in non-accreting stars of the same mass and effectively reduces the inferred LDB mass and, thus, the minimum allowable age. Here, we have not taken episodic accretion into account. While we do not have an optical spectrum of the secondary, the presence (absence) of Li 1 in the spectrum would set a upper (lower) limit on the mass and, hence, the age of the system, in this case $\lesssim$1.8 Gyr ($\gtrsim$1.1 Gyr). The likely proximity of the mass of the secondary to the LDB is motivation to obtain an optical spectrum of this component.

The absence of H$\alpha$ emission in the optical spectrum of 2MASS J0130−4445A and lack of UV or X-ray flux—the system is not detected in the GALEX (Martin et al. 2005) or the ROSAT (Voges et al. 1999) All-Sky Surveys—indicates that the system is not particularly active and, hence, not likely to be a very young system. This absence indicates that 2MASS J0130−4445AB is probably older than 1–100 Myr, as such emission has been detected in brown dwarfs in the Orion Nebula Cluster (isochronal age ∼1 Myr; Peterson et al. 2008), Taurus (∼3 Myr; Guieu et al. 2006), $\sigma$ Orionis (2–7 Myr; Zapatero Osorio et al. 2002), $\alpha$ Persei (∼80 Myr; Stauffer et al. 1999), Pleiades (∼100 Myr; Stauffer et al. 1998; Martín et al. 2000), and Blanco 1 (∼100 Myr; P. A. Cargile et al., in prep.). However, activity signatures might not be reliable age indicators in the VLM regime. Both H$\alpha$ and X-ray emission drop precipitously across the M dwarf/L dwarf transition (e.g., Kirkpatrick et al. 2000; Gizis et al. 2000; West et al. 2004; Stelzer et al. 2006), likely the result of reduced magnetic field coupling with increasingly neutral photospheres (e.g., Gelino et al. 2002; Mohanty et al. 2002).

Extreme youth can also be ruled out based on the the NIR spectra of these sources, which do not exhibit the triangular H-band peaks seen in ∼100 Myr Pleiades M and L dwarfs (Bihain et al. 2010) and young field L dwarfs (e.g., Kirkpatrick et al. 2006). It is notable that 2MASS J0130−4445B is somewhat red compared to typical L6 dwarfs ($\langle J - K_s \rangle$ = 1.82±0.07; Schmidt et al. 2010), as red sources have been shown to exhibit smaller velocity dispersions and, hence, younger ages (Faherty et al. 2009; Schmidt et al. 2010). However, 2MASS J0130−4445A is not unusually red for its spectral type ($\langle J - K_s \rangle$ = 1.12±0.10);

and the red color of the secondary may reflect an unusually dusty atmosphere (e.g., Looper et al. 2008b). Also, neither NIR spectra nor the optical spectrum of 2MASS J0130−4445A show high gravity signatures, i.e., unusually blue colors form enhanced $H_2$, or evidence of the system being metal-poor, making it unlikely that the system is as old as ∼10 Gyr (Burgasser et al. 2003a; Reid et al. 2007).

Considering the kinematics of the system, the tangential velocity of 2MASS J0130−4445A, 19±3 km $s^{-1}$ is similar to the median velocities of the L dwarfs in the SDSS sample (28±25 km $s^{-1}$; Schmidt et al. 2010), the M9 dwarfs in the BDKP sample (23±23 km $s^{-1}$; Faherty et al. 2009), and the M7–L8 dwarfs in the 2MASS sample (25±21 km $s^{-1}$; Schmidt et al. 2007), with the quoted errors being the $1\sigma$ dispersions. The low tangential velocity suggests that 2MASS J0130−4445AB is part of the thin disk, although we note that we cannot rule out a higher space velocity for the binary system. Kinematic studies have found that late-M and L dwarfs with average kinematics are typically ∼2–4 Gyr old (Wielen 1977; Faherty et al. 2009).

In conclusion, based on the absence of Li 1 in the primary, we can place a (model-dependent) hard limit on the minimum age of 2MASS J0130−4445AB to be ∼250 Myr while its kinematics indicate a preferred age of ∼2–4 Gyr. Spectral features for both components are in agreement with these ages. For the ages of 0.25–10 Gyr, based on the Burrows et al. (1993) and Burrows et al. (1997) models, the estimated masses for 2MASS J0130−4445A and 2MASS J0130−4445B are 0.055–0.083 and 0.032–0.076 $M_\odot$, respectively, and the mass ratio is 0.57–0.92. For kinematics-based age limits of 2–4 Gyr, the estimated masses for 2MASS J0130−4445A and 2MASS J0130−4445B are 0.082–0.083 and 0.066–0.073 $M_\odot$, respectively, and the mass ratio is 0.81–0.89 (Table III.4). Hence, the components straddle the hydrogen-burning mass limit; and this system is likely composed of a very low mass star and (massive) brown dwarf pair.

Table III.4. Model-dependent Properties of 2MASS J0130−4445AB

| Parameter | Age (Gyr) | | | |
|---|---|---|---|---|
| | 0.25 | 2 | 4 | 10 |
| Primary Mass ($M_\odot$) | 0.055 | 0.082 | 0.083 | 0.083 |
| Secondary Mass ($M_\odot$) | 0.032 | 0.066 | 0.073 | 0.076 |
| Mass Ratio | 0.57 | 0.81 | 0.89 | 0.92 |
| Log Binding Energy (erg) | 41.61 | 41.96 | 41.97 | 41.97 |
| Period (yr) | 5030 | 3860 | 3760 | 3720 |

## 3.5 Discussion

### 3.5.1 Formation of Wide VLM Binaries in the Field

With a projected separation of 130±50 AU, 2MASS J0130−4445AB is one of only ten VLM systems wider than 100 AU, with six of them in the field. All of these systems have been identified relatively recently; prior to their discovery, it was believed that VLM field systems were nearly all tight, a possible consequence of dynamic ejection early on. Based on this idea and the VLM binary population known at the time, two relations to define the largest possible separation of VLM binaries were proposed. First, Burgasser et al. (2003b) suggested that the maximum separation of a system was dependent on its mass: $a_{\rm max}$ (AU) = 1400 $(M_{\rm tot}/M_\odot)^2$. Second, Close et al. (2003) proposed that the stability of binary systems was contingent on their binding energy—a criterion based on the product rather than the sum of component masses; thus, only systems with binding energy $\geq 10^{42.5}$ erg would exist in the field[5]. For the (age-dependent) estimated mass of 2MASS J0130−4445AB, the Burgasser et al. (2003b) relation equates to maximum physical separations of only 9.2 AU and 35.4 AU for ages of 0.25 and 10 Gyr, respectively, which are both much smaller than the physical separation we have measured for 2MASS J0130−4445AB. Similarly, the binding energies for the system are $10^{41.61}$ and $10^{41.97}$ erg for the same ages (see Table III.4). Both the Burgasser et al. (2003b)

[5]We note that for the small separations and a mass ratio highly skewed toward one, which was the case for the VLM binaries known at the time, the Burgasser et al. (2003b) and Close et al. (2003) limits are essentially equivalent.

and Close et al. (2003) relations are definitively violated by 2MASS J0130−4445AB, for all ages and mass ratios. Assuming these limits emerge from dynamical scattering processes, this binary seems unlikely to have formed via the ejection of protostellar embryos.

More recently, Zuckerman & Song (2009) have argued that fragmentation, rather than dynamical, processes are more likely to describe the boundary for the lowest binding energy systems. A protostellar cloud can only fragment if it is more massive than the minimum Jeans mass ($\sim$7 $M_J$; Low & Lynden-Bell 1976). Assuming fiducial separations of 300 AU for the fragments, they derived a cut-off for binding energy as a function of total systemic mass. Finding that this disfavors the formation of very wide and/or high mass ratio binaries, Faherty et al. (2010) used the Jeans length, instead of the fiducial separation, and mass ratio of the system. For 2MASS J0130−4445AB at 0.25 Gyr ($M_{tot}\approx$0.1 $M_\odot$), Zuckerman & Song (2009) and Faherty et al. (2010) relations suggest minimum binding energies of $10^{40.5}$ and $10^{39}$ erg, respectively; if the system were older, they would be even more stable due to the higher masses. 2MASS J0130−4445AB is well within the bounds of both Zuckerman & Song (2009) and Faherty et al. (2010) formation criteria for all ages and mass ratios. Hence, the observed wide, low binding energy VLM binaries could have formed from small protostellar clouds, with masess close to the local Jeans mass.

Current numerical simulations have suggested an alternative mechanism to form wide binaries: N-body dynamics in small clusters disrupt the VLM pairs wider than $\sim$60 AU, and very wide systems ($> 10^4 - 10^5$ AU) can then be formed when stars are ejected into the field in the same direction (Moeckel & Bate 2010; Kouwenhoven et al. 2010). While this provides a mechanism to create the most fragile VLM pairs identified to date, it does not aid in the formation of 100–1000 AU pairs like 2MASS J0130−4445AB. Two other VLM systems in this separation range are known: 2MASSJ 1623361−240221 (220 AU; Billères et al. 2005) and SDSS J141623.94+134826.3 (100 AU; Burningham et al. 2010; Scholz 2010).

### 3.5.2 2MASS J0130−4445AB as a Probe of the M Dwarf/L Dwarf Transition

The components of 2MASS J0130−4445AB straddle a spectral type range that is particularly interesting for three reasons. First, condensate clouds become an important source of photospheric opacity and thermal evolution starting at the end of the M dwarf sequence

and peaking in influence in the middle of the L dwarf sequence (Ackerman & Marley 2001; Kirkpatrick et al. 2008; Saumon & Marley 2008). With a component on either end of this regime, 2MASS J0130−4445AB is a particularly useful coeval laboratory for studying the emergence and dispersal of these clouds. Second, both components straddle the hydrogen-burning mass limit; and the secondary is very near the LDB. Detection of Li 1 in the optical spectrum of the secondary could provide a relatively precise constraint on the age of this system (0.25–1.8 Gyr) and thereby make it a useful benchmark for studies of brown dwarf thermal evolution and atmospheric models (e.g., Pinfield et al. 2006). Third, the M dwarf/L dwarf transition exhibits a steep decline in magnetic activity metrics, including H$\alpha$, UV, and X-ray emission (e.g., Gizis et al. 2000; West et al. 2004) but notably not radio emission (e.g., Berger 2006; Berger et al. 2010). This is believed to be due to the decoupling of magnetic fields from an increasingly neutral photosphere (Gelino et al. 2002; Mohanty et al. 2002) but does not rule out the presence of significant magnetic fields (Reiners & Basri 2007). While H$\alpha$ is absent in the spectrum of 2MASS J0130−4445A, examination of field strengths and radio emission in this coeval pair may facilitate understanding of how magnetic fields evolve across the stellar/brown dwarf transition. As one of only three binaries spanning the M dwarf/L dwarf transition whose components are easily resolvable from ground-based facilities (the other two are the 1.″2 L1.5+L4.5 2MASSJ 1520022−442242 and the 1.″0 M9+L3 2MASSJ 1707234−055824; Burgasser 2004; Burgasser et al. 2007a; Folkes et al. 2007), 2MASS J0130−4445AB is an important laboratory for studying how condensate clouds, lithium burning, and magnetic activity trends vary across this transition.

## 3.6 Conclusions

We have identified a binary companion to 2MASS J01303563−4445411A based on NIR imaging and spectroscopic observations. The secondary is well-separated ($\Delta\theta = 3.''2$) and much fainter ($\Delta K \approx 2.35$ mags). Based on template matching and spectral indices, we have calculated the NIR spectral types to be M9.0±0.5 and L6±1 for the two components. The optical spectrum of 2MASS J0130−4445A shows no evidence of either H$\alpha$ or Li 1 indicating a minimum age of 0.25 Gyr, while the kinematics suggest an age of 2–4 Gyr. However, we would like to stress that 0.25–10 Gyr, with the lower bound set by LDB and activity, is the

more secure age for the system. 2MASS J0130−4445AB is likely a "grown-up" wide binary that has survived ejections and/or dynamical interactions. More importantly, the system definitively violates the binary stability limits based on the ejection hypothesis (Burgasser et al. 2003b; Close et al. 2003) and satisfies the limits based on the idea that wide VLM binaries are formed from approximately Jeans mass-sized protostellar clouds (Zuckerman & Song 2009; Faherty et al. 2010). This suggests that observed wide VLM binaries may have formed differently than single VLMs and/or tighter binaries. As one of ten VLM systems with separations $\gtrsim$100 AU, 2MASS J0130−4445AB provides a stringent test for theoretical studies of VLM binary formation, as well as a well-resolved, coeval laboratory for studying empirical trends across the M dwarf/L dwarf and stellar/brown dwarf transitions.

CHAPTER IV

# REFINED METALLICITY INDICES FOR M DWARFS USING THE SLoWPoKES CATALOG OF WIDE, LOW-MASS BINARIES

The bulk of this chapter was published in the *The Astronomical Journal* as Dhital, West, Stassun, Bochanski, Massey, & Bastien (2012, 143:67); the American Astronomical Society holds the copyright for the article.

In this chapter, we report the results from spectroscopic observations of 113 SLoWPoKES systems identified in Chapter II. Radial velocities of each binary member are used to confirm that they are co-moving and, consequently, to further validate the high fidelity of the SLoWPoKES catalog. We use the observed pairs as coeval laboratories to test the relative metallicity index $\zeta_{\rm TiO/CaH}$ and find that it does trace the iso-metallicity loci for most of our sample of M dwarfs. However, we find a small systematic bias in $\zeta_{\rm TiO/CaH}$, especially in the early-type M dwarfs. Assuming iso-metallicity for the observed pairs, We use recalibrate the definition of $\zeta_{\rm TiO/CaH}$. While representing a small change in the definition, the new $\zeta_{\rm TiO/CaH}$ is a significantly better predictor of iso-metallicity for the higher mass M dwarfs. We also use the pairs to look at magnetic activity and find that 81% of the pairs have similar H$\alpha$ levels. The difference in H$\alpha$ equivalent width amongst components with similar masses was smaller than the range of H variability for individual objects.

## 4.1 Introduction

Low-mass stars, generally defined as the regime bracketed by the hydrogen-burning limit ($\sim$0.08 $M_\odot$) and the onset of molecular lines in the photosphere ($\sim$0.8 $M_\odot$), make up $\sim$ 70% of the Milky Way's stars (Bochanski et al. 2010) and are, perhaps, the best tracers of the structure, dynamics, and evolutionary history of the Galaxy. However, their intrinsic faintness has historically limited the construction of large samples. In addition, the ubiquitous molecular features in their photospheres and the resulting incomplete line lists has restricted the accuracy and usefulness of theoretical atmospheric models. Large surveys, such as SDSS

(York et al. 2000) and 2MASS (Skrutskie et al. 2006), have played a large role in advancing our understanding of low-mass stars. With a photometric catalog of more than 33 million (Bochanski et al. 2010) and a spectroscopic catalog of more than 70,000 (West et al. 2011) M dwarfs, SDSS has enabled studies of the spatial (Bochanski et al. 2010) and kinematic distributions (Bochanski et al. 2007b; Fuchs et al. 2009) in the Milky Way; the mass and luminosity functions (Covey et al. 2008; Bochanski et al. 2010); and magnetic activity (e.g., West et al. 2008, 2011; Kruse et al. 2010; Kowalski et al. 2009; Hilton et al. 2010) of low-mass stars.

The metallicity of low-mass stars remains an elusive parameter to measure. Given the large number of M dwarfs in the Milky Way, an absolute metallicity scale tied to an easily observable spectral index would allow for the tracing of the formation history and the chemical evolution of the Galaxy (e.g., West et al. 2008), the dependence of the fundamental mass–radius relation on metallicity at the bottom of the main sequence (e.g., López-Morales 2007), and the relationship between metallicity and the presence of planets (e.g., Laws et al. 2003; Valenti & Fischer 2008). While spectral modeling has allowed for metallicity determinations and well-defined metallicity indices for warmer stars, such efforts in the late-K and M spectral type regimes (e.g., Hauschildt, Allard, & Baron 1999; Witte et al. 2011) have met with notable problems due to the onset of broad molecular lines at $\lesssim$4300 K and due to incomplete molecular line lists. Some authors have tried to use photometric indices to infer the metallicity (Bonfils et al. 2005; Johnson & Apps 2009; Schlaufman & Laughlin 2010), but these techniques rely on trigonometric parallax measurements which are uncommon for M dwarfs.

Some useful spectral features that correlate with metallicity have been identified. In the near-infrared, Rojas-Ayala et al. (2010) developed a metallicity indicator based on the strength of the Na 1 doublet, the Ca 1 triplet, and a temperature-sensitive water index. This technique has so far only been calibrated over a limited range but delivers the greatest precision among current techniques. Meanwhile, much effort has gone into optical spectra. As the TiO band in the optical spectrum becomes weaker with decreasing metallicity (Bessell 1982), the ratio of CaH and TiO molecular bands has been used to distinguish M dwarfs from M subdwarfs (Kirkpatrick, Henry, & McCarthy 1991; Reid, Hawley, & Gizis 1995;

Gizis 1997; Lépine, Rich, & Shara 2003; Burgasser & Kirkpatrick 2006). Building on these studies, LRS07 defined the metallicity-dependent quantity $\zeta_{\rm TiO/CaH}$ using the Reid et al. (1995) CaH2, CaH3, and TiO5 molecular band heads; this allowed for the segregation of low-mass dwarfs into four classes: dwarfs (dMs), subdwarfs (sdMs), extreme subdwarfs (esdMs), and ultra subdwarfs (usdMs). These classes may also trace the Galactic populations to which these stars belong: dMs were formed in the thin disk, sdMs in the thick disk, and esdMs/usdMs in the halo. LRS07 calibrated the definition of $\zeta_{\rm TiO/CaH}$ using the visual binary pairs known at the time, including four sdM and two esdM pairs. Woolf, Lépine, & Wallerstein (2009) mapped the $\zeta_{\rm TiO/CaH}$ index to an absolute metallicity scale using dM binaries with a FGK companion of measurable absolute metallicity; but it suffers from significant scatter ($\sim$0.3 dex).

Wide binary (or multiple) systems are ideal, coeval laboratories to constrain and calibrate the observable properties of stars as the components were presumably formed at the same time and from the same primordial material but have evolved independently. In Chapter II, we identified the Sloan Low-mass Wide Pairs of Kinematically Equivalent Stars (SLoWPoKES) catalog consisting of 1342 ultra-wide, low-mass common proper motion (CPM) binary systems from the SDSS Data Release 7 (DR7; Abazajian et al. 2009) by matching angular separations, photometric distances, and proper motions. The binary systems in the catalog have at least one low-mass (spectral subtype K5 or later) component, projected physical separations of $\sim10^3$–$10^5$ AU, and distances of $\sim$50–800 pc. While most SLoWPoKES pairs are disk dwarfs, 70 low-metallicity sdM and 21 white dwarf–dM pairs were identified based on their reduced proper motions. A Galactic model—based on empirical constraints on the stellar number density (Bochanski et al. 2010; Jurić et al. 2008) and velocity (Bochanski et al. 2007a) distributions in the Milky Way—was used to assess the probability that the candidates were a chance alignment of random stars; only pairs with such probabilities $\leq 5\%$ were published in the SLoWPoKES catalog. The overall fidelity of the catalog is expected to be $\sim$98%. Hence, the SLoWPoKES catalog is a very clean and diverse source of CPM binary systems to be used in follow-up studies. As the SLoWPoKES catalog spans a wide range in mass and a smaller, but still considerable, range in metallicity, it is an ideal sample to constrain the $\zeta_{\rm TiO/CaH}$ index as well as to eventually map it to an absolute metallicity

space.

Magnetic activity has been shown to decline with age, with activity lifetimes of ∼1–2 Gyr for M0–M3 and ∼7–8 Gyr for M5–M7 dwarfs (West et al. 2006, 2008, 2011). This monotonic decline of activity with age is a signature of stellar spin-down and suggestive of a gyrochronology-like age–rotation–activity relationship in M dwarfs (Skumanich 1972; Barnes 2003, 2007; Delorme et al. 2010). Leveraging the coevality of components of the SLoWPoKES pairs is a good way of testing this relationship.

We have carried out a spectroscopic follow-up study of 113 CPM pairs from the SLoWPoKES catalog. Section 4.2 details our observations and the data reduction procedures. In Section 4.3 we use our radial velocities to assess the fidelity of the observed SLoWPoKES pairs, use them to redefine the $\zeta_{\rm TiO/CaH}$ index, and examine the magnetic activity properties of the SLoWPoKES pairs. The conclusions are presented in Section 4.4.

## 4.2 Observations & Data Reduction

The spectroscopic targets were selected from the SLoWPoKES catalog based on their brightnesses, colors, and inferred mass ratios. Both components were required to be brighter than $r \sim 17$ so as to obtain the desired S/N within a reasonable integration time. Efforts were made to obtain (i) an even distribution in $r-z$ space for both the primary and secondary components and (ii) a roughly equal number of equal-mass (within 5% of each other) and unequal-mass ($\gtrsim$ 5% of each other) systems. We estimated masses from the $r-z$ colors based on Kraus & Hillenbrand (2007).

Observations were carried out with the GoldCam spectrograph on the KPNO 2.1m telescope on two separate observing runs on January 11–16, 2009 UT and March 26–31, 2010 UT. For both runs, the #36 grating (1200 lines mm$^{-1}$) in the first order, blazed at 7500 Å, along with the OG 550 order-blocking filter were used resulting in a wavelength coverage of ∼6200–8200 Å with a dispersion of 0.62 Å pixel$^{-1}$. A slit width of 2″ was used to maximize the number of photons collected yielding an effective resolution of 1.8 Å and a resolving power of 3500. Both components of a binary were observed at the same time by rotating the slit to align with the position angle of the binary. While the rotation had to be done manually and required ∼10 min of overhead time, it was more efficient than observing each

component separately.

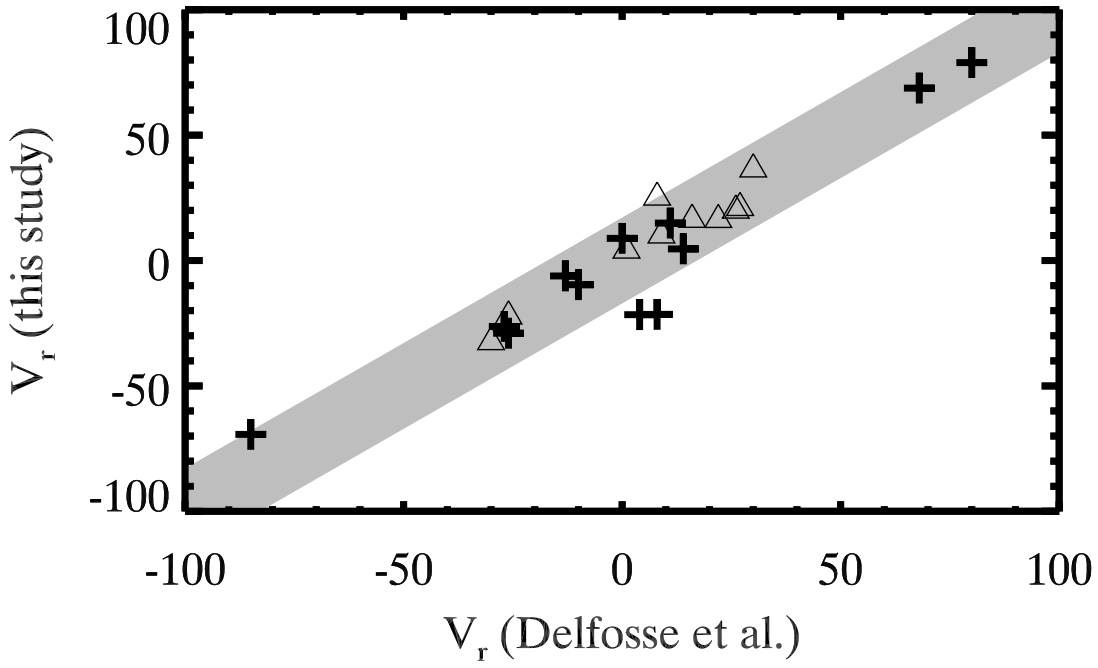


Figure 4.1: Comparison of the radial velocities for the standard stars from the 2009 (triangles) and 2010 (pluses) observation runs selected from Delfosse et al. (1998) shows no systematic trends. The m.a.d. of the difference between the Delfosse et al. (1998) and the measured $V_r$ was 5.7 km $s^{-1}$; we adopt this value as the error in our radial velocity measurements. The 3 m.a.d. regime is shaded in gray.

Each night quartz flats and biases were taken before the targets were observed; when the first half of the night was lost due to weather, the flats and biases were taken in the morning. For wavelength calibration, HeNeAr comparison arcs, along with the BG 38 order-blocking filter, were generally taken after each target or when the CCD orientation was rotated. A suite of radial velocity standards from Delfosse et al. (1998) were observed, which we used to assess our radial velocity precision (see below). Similarly, a flux standard—HZ 44, a bright sdO star—was observed each night during the second run. Both observing runs were conducted in bright time, often during non-photometric seeing. A combination of clouds and high winds caused the loss of 3–4 nights between the two runs.

Table IV.1. Radial Velocity Standards from (Delfosse et al. 1998)

| Name | Spectral Type | $V_r$ (km $s^{-1}$) |
|---|---|---|
| GJ 1057 | M4 | 27 |
| GJ 1093a | M4 | −30 |
| GJ 1111 | M8 | 9 |
| GJ 1156 | M5 | 4 |
| Gl 70 | M2 | −26 |
| Gl 105b | M3 | 26 |
| Gl 109 | M2 | 30 |
| G 165−08 | M4 | 8 |
| Gl 205 | M0 | 8 |
| Gl 251 | M2 | 22 |
| Gl 338 | M0 | 11 |
| Gl 380 | K5 | −26 |
| Gl 411 | M2 | −85 |
| Gl 412B | M5 | 68 |
| Gl 450 | M1 | 0 |
| Gl 514 | M0 | 14 |
| Gl 581 | M2 | −10 |
| Gl 623 | M2 | −27 |
| Gl 625 | M1 | −13 |
| LHS 1805 | M4 | 1 |
| LHS 2520 | M3 | 80 |
| LHS 1885 | M4 | 16 |

All spectra were bias-subtracted, flat-fielded, extracted, co-added, wavelength-calibrated, and flux-calibrated[1] using standard IRAF[2] procedures, following the prescription detailed in Massey et al. (1992). Eighteen pairs where one of the components (usually the fainter secondary) was not well-calibrated or had low S/N were removed from the sample. The stars were then manually spectral typed with the HAMMER pipeline (Covey et al. 2007); the error in the process is expected to be smaller than one sub-type, as discussed by West

[1]As flux-calibrations were not taken for the first run, we used a subset of radial velocity standards, which had absolute flux measurements as part of the Palomar-Michigan State Survey (Reid et al. 1995), as flux standards.

[2]IRAF is distributed by the National Optical Astronomy Observatory, which is operated by the Association of Universities for Research in Astronomy (AURA) under cooperative agreement with the National Science Foundation.

et al. (2011).

The radial velocities ($V_r$) of the stars were measured by cross-correlating the spectra using IDL routine XCORL.PRO (Mohanty & Basri 2003; West & Basri 2009) with the appropriate spectral type templates from Bochanski et al. (2007b), which are in the heliocentric rest frame. The cross-correlation was performed in the wavelength range of 6600–7550 Å. Since templates are only available for M0–L0 dwarfs, M0 templates were used for K7 dwarfs. However, as each spectral type spans a range in mass and temperature, the spectral features in stars of the same subtype can differ significantly. This is probably the largest source of error in measuring $V_r$ with the cross-correlation techniques. However, cross-correlation with templates typically yields $V_r$ with $\lesssim 10$ km s$^{-1}$ precision for SDSS spectra (Bochanski et al. 2007a) Other sources of error include difference in resolution between the template and object spectra and the accuracy of wavelength calibration, which was $\lesssim 0.04$ Å/pixel rms (1.4 km s$^{-1}$) for all but a few of the objects.

To assess the errors in our radial velocities, we cross-correlated the observed radial velocity standards (Delfosse et al. 1998) with appropriate templates from Bochanski et al. (2007b). Figure 4.1 shows the comparison between our measured values and the Delfosse et al. (1998) values, which were measured from high-resolution spectra. Apart from three outliers from the 2010 seasons, our values compare well with the Delfosse et al. (1998). The median absolute deviation (m.a.d.) of the difference was 5.7 km s$^{-1}$; we adopt 6 km s$^{-1}$ as the typical error in our measurement of $V_r$.

The spectra were then corrected for the measured radial velocities to be in the heliocentric rest frame and fed back into the HAMMER pipeline to measure the equivalent width of H$\alpha$; the molecular band strengths of CaH2, CaH3, and TiO features; and the S/N of the spectra, which was measured in the region spanning 6500–6550 Å.

## 4.3 Results

Figure 4.2 shows the spectral type and $r - z$ color distributions of the primary and the secondary components of the 113 SLoWPoKES pairs that were observed (Tables IV.2 and IV.3 ); the number of pairs in each bin is also shown. The observed sample, excluding pairs that were rejected for low S/N or other reasons, spans the K7–M4 spectral types ($r - z =$

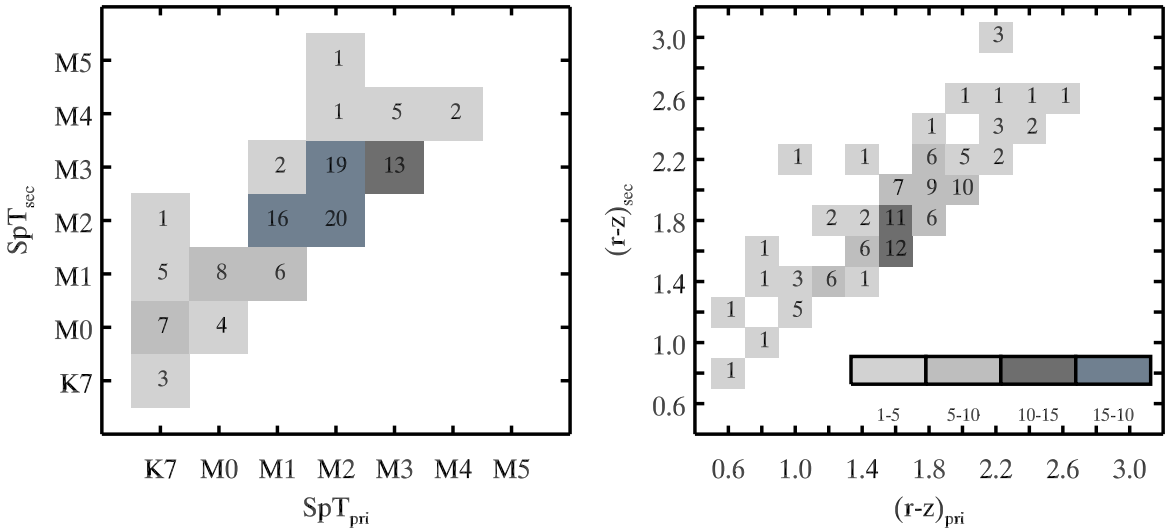


Figure 4.2: The distribution of measured spectral types and $r-z$ colors for both the primary and secondary components of the 113 SLoWPoKES pairs observed in our KPNO run. The spectral types are shown in 1 subtype bins while the colors are in 0.2 mag bins. The background colors indicated the density in each bin, with the individual numbers printed as well. By definition, the primary always has a earlier spectral type and a bluer color than the secondary.

0.66–2.52) for the primary and K7–M5 ($r-z = 0.77$–$3.08$) for the secondary. Even though our observed sample was limited to $r \sim 17$ and, thus, a dearth of late-type M dwarfs was to be expected, there are nonetheless 11 pairs with at least one component later than M4 and only two pairs with both components later than M4.

### 4.3.1 Spectroscopic Binaries

As discussed in Section 4.2, the radial velocities were measured by cross-correlating the program spectra with the appropriate SDSS template spectra (Bochanski et al. 2007b). The cross-correlation function (CCF) is used to determine the best match between the templates and program spectra. Presence of multiple turning points in the CCF as well as unusual broadening of the spectrum can indicate the presence of a spectroscopic binary (SB; Matijevič et al. 2010). While such a detection is unambiguous only in high-resolution spectra, we found possible evidence of SBs in our low-resolution spectra. Alternatively, the wide CCF could

Table IV.2. Properties of observed SLoWPoKES binaries–Part I

| ID | Right Ascension | | Declination | | distance | | $\mu_\alpha$ | | $\mu_\delta$ | | $V_r$ | |
|---|---|---|---|---|---|---|---|---|---|---|---|---|
| | A | B | A | B | A | B | A | B | A | B | A | B |
| SLW J2000 | (hh mm ss.s) | | (dd mm ss.ss) | | (pc) | | (mas yr$^{-1}$) | | (mas yr$^{-1}$) | | (km s$^{-1}$) | |
| 1512+20 | 15 12 22.52 | 15 12 25.41 | +20 28 20.6 | +20 28 12.3 | 63 | 58 | -49 | -48 | 4 | 7 | -84.8 | -77.8 |
| 0831+36 | 08 31 23.12 | 08 31 23.16 | +36 54 41.8 | +36 54 17.2 | 70 | 83 | 49 | 46 | -54 | -57 | -30.8 | -25.9 |
| 0741+19 | 07 41 55.34 | 07 41 57.06 | +19 55 45.8 | +19 55 33.3 | 66 | 78 | -36 | -35 | -27 | -27 | 31.2 | 47.8 |
| 0957+37 | 09 57 57.18 | 09 57 55.63 | +37 56 02.4 | +37 55 52.8 | 87 | 75 | -23 | -23 | -60 | -59 | -23.6 | -31.2 |
| 1120+20 | 11 20 03.38 | 11 20 05.26 | +20 46 53.2 | +20 46 54.9 | 96 | 101 | -37 | -41 | -2 | 0 | -7.6 | -40.6 |
| 0858+09 | 08 58 57.80 | 08 58 54.73 | +09 36 59.1 | +09 37 23.7 | 65 | 63 | -111 | -107 | 6 | 6 | 23.5 | 32.7 |
| 1527+49 | 15 27 52.04 | 15 27 50.57 | +49 08 54.2 | +49 09 47.4 | 70 | 65 | -60 | -63 | 50 | 53 | -89.7 | -90.2 |
| 0734+28 | 07 34 50.75 | 07 34 49.23 | +28 17 39.7 | +28 18 15.8 | 62 | 75 | -27 | -29 | -28 | -29 | -2.3 | -36.7 |
| 1318+47 | 13 18 15.49 | 13 18 15.00 | +47 30 29.4 | +47 31 33.7 | 47 | 47 | -104 | -103 | 33 | 35 | -60.1 | -71.6 |
| 1508+06 | 15 08 44.07 | 15 08 43.72 | +06 46 25.9 | +06 46 35.5 | 110 | 108 | -42 | -44 | 0 | 0 | -80.4 | -51.3 |

Note. — The first 10 pairs are listed here; the full version of the table is available online on the SLoWPoKES website (`http://www.vanderbilt.edu/astro/slowpokes/`) and *the Astronomical Journal* website (`http://iopscience.iop.org/1538-3881/143/3/67`).

Table IV.3. Properties of observed SLoWPoKES binaries–Part II

| ID | $r$ | | $r-z$ | | Spectral Type | | EW (H$\alpha$) | | CaH2 | | CaH3 | | TiO5 | |
|---|---|---|---|---|---|---|---|---|---|---|---|---|---|---|
| | A | B | A | B | A | B | A | B | A | B | A | B | A | B |
| SLW J2000 | (mag) | | | | | | (Å) | | | | | | | |
| 1512+20 | 15.01 | 16.87 | 2.02 | 2.56 | M3 | M4 | -0.18 | 0.00 | 0.45 | 0.36 | 0.72 | 0.63 | 0.44 | 0.34 |
| 0831+36 | 16.13 | 16.51 | 2.12 | 2.36 | M3 | M4 | 2.36 | 7.93 | 0.42 | 0.38 | 0.69 | 0.62 | 0.43 | 0.37 |
| 0741+19 | 16.29 | 16.67 | 2.22 | 2.46 | M3 | M4 | 3.06 | 7.18 | 0.43 | 0.41 | 0.69 | 0.67 | 0.42 | 0.38 |
| 0957+37 | 17.28 | 17.34 | 2.45 | 2.57 | M3 | M4 | 4.11 | 7.16 | 0.39 | 0.39 | 0.65 | 0.64 | 0.38 | 0.34 |
| 1120+20 | 16.62 | 17.09 | 2.13 | 2.32 | M3 | M3 | 7.16 | 0.99 | 0.46 | 0.44 | 0.72 | 0.70 | 0.45 | 0.45 |
| 0858+09 | 15.58 | 15.76 | 2.12 | 2.20 | M3 | M3 | 5.12 | 2.57 | 0.42 | 0.42 | 0.65 | 0.67 | 0.39 | 0.43 |
| 1527+49 | 16.00 | 17.01 | 2.19 | 2.57 | M3 | M4 | 4.83 | 1.08 | 0.32 | 0.41 | 0.59 | 0.68 | 0.31 | 0.41 |
| 0734+28 | 14.40 | 14.78 | 1.65 | 1.90 | M2 | M2 | 4.64 | 0.00 | 0.46 | 0.53 | 0.69 | 0.76 | 0.49 | 0.55 |
| 1318+47 | 15.19 | 17.40 | 2.20 | 2.95 | M2 | M5 | 1.95 | 3.94 | 0.41 | 0.33 | 0.68 | 0.62 | 0.42 | 0.27 |
| 1508+06 | 15.66 | 17.04 | 1.78 | 2.23 | M2 | M2 | 3.53 | 0.64 | 0.42 | 0.49 | 0.67 | 0.75 | 0.43 | 0.52 |

Note. — The first 10 pairs are listed here; the full version of the table is available online on the SLoWPoKES website (`http://www.vanderbilt.edu/astro/slowpokes/`) and *the Astronomical Journal* website (`http://iopscience.iop.org/1538-3881/143/3/67`).

correspond to fast rotators, although our $v \sin i$ resolution of 35 km s$^{-1}$ means they would have to be rotating at very high speeds. Figure 4.3 shows the CCF for the ten SB candidates (Table IV.4). All ten candidates have a relatively high S/N ratio, so the CCF is not a product of noisy spectral features. For comparison, the CCF for the radial velocity standards, which are presumably single stars, of the corresponding spectral types are shown in red, dashed lines. High-resolution spectra are required to confirm these SBs.

Previous studies have found that components of wide binaries are more likely to have a companion as compared to single field stars. This enhanced binarity has been ascribed to the ease of transfer of angular momentum that facilitates the formation of close pairs (Tokovinin 1997; Bate et al. 2002; Burgasser et al. 2005; Connelley et al. 2009) and/or the stability of wide pairs in the field (Law et al. 2010). Among very low-mass wide binaries, the frequency of tight companions is (50±11)% (Faherty et al. 2010). In a sample of nearby SLoWPoKES pairs, Law et al. (2010) found that the bias-corrected higher-order multiplicity was $45^{+18}_{-16}$%. While only 10 of 113 pairs (8.8%) in this study have been identified as hierarchical, we were probing a different kind of hierarchical systems than those found by Law et al. 2010. Here we probed the extremely close pairs (spectroscopic binaries) whereas Law et al. 2010 probed systems with separations larger than 8–10 AU. In fact, our results are consistent with the Law et al. 2010 findings but limited to the extremely close pairs.

### 4.3.2 Fidelity of SLoWPoKES Pairs

The observed pairs were identified in Chapter II based on a matching of their position, distance, and proper motions. The third velocity component, $V_r$, can be used to test the fidelity of the observed pairs and, by extrapolation, of the SLoWPoKES catalog.

Figure 4.4 shows the radial velocities of the primary component against that of the secondary in the left panel and the distribution of their differences in the right panel. The identified candidate SBs are shown as concentric circles. Excluding the ten candidate SBs, 90 of the remaining 103 pairs (i.e., 87.4%) have $\Delta V_r$ within 3 $\sigma$ of the mean; the 3 $\sigma$ region is shown in gray in the left panel. Overall, the $\Delta V_r$ distribution is well-fit by a Gaussian with $\mu = -0.97 \pm 0.80$ km s$^{-1}$ and $\sigma = 12.04 \pm 0.80$ km s$^{-1}$, shown as the dashed line though

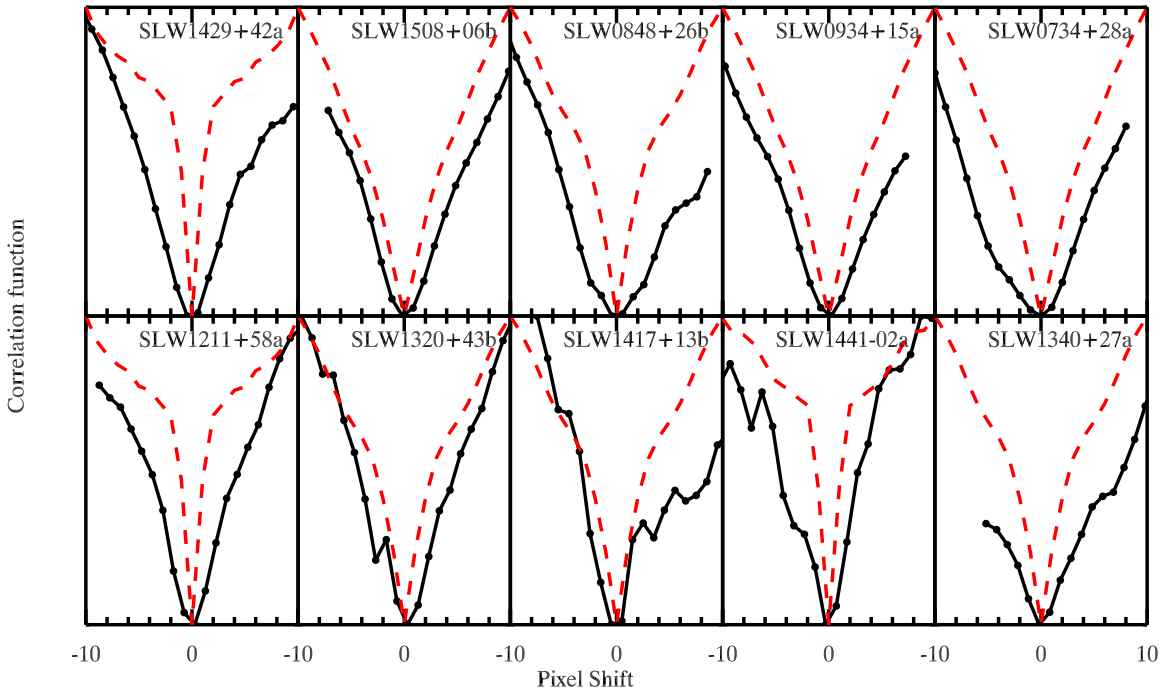


Figure 4.3: Broad cross-correlation functions (solid lines) and/or split spectral features indicate the presence of a tight companion in the ten of the observed systems. For reference, the auto-correlation function of our radial velocity standards are also shown (dashed lines). High-resolution spectra are needed to confirm the spectroscopic binaries. All spectra were corrected to the heliocentric rest frame.

there are more outliers than expected (see below). As $\sigma$ ≈1.4826 m.a.d for large normally distributed populations, $\sigma_{\Delta V_r}$ ( $= \sqrt{2} \times \sigma_{V_r} = \sqrt{2} \times 1.4826 \times$ 5.7 km s$^{-1}$ = 11.95 km s$^{-1}$) is in excellent agreement with the m.a.d. we measured for our radial velocity standards.

We checked that the $\Delta V_r$ distribution of our binaries is indeed distinct from physically unassociated stars. We used the Galactic model from Chapter II that gives the expected 3-d velocity distribution for any position in the Galaxy or, if desired, a randomly chosen velocity from that distribution. We compared with a sample that has been selected in a similar manner to the pairs in our observed sample. Hence, at the Galactic positions of each of the observed pairs, we generated pairs of 3-d velocities until a pair with matching proper motions was found. The proper motion matching criteria was the same as that in Chapter II. For statistical robustness, we conducted $10^6$ realizations of this simulation; the

Table IV.4. Candidate Spectroscopic Binaries

| Name | Spectral Type | Note |
|---|---|---|
| SLW 1211+58a | M0 | ··· |
| SLW 1320+43b | M1 | wide CCF |
| SLW 1417+13b | M1 | wide CCF |
| SLW 1441-02a | K7 | ··· |
| SLW 1340+27a | M1 | wide lines; wide CCF |
| SLW 1429+42a | M0 | double peak |
| SLW 1508+06b | M2 | wide CCF |
| SLW 0848+26b | M1 | wide CCF |
| SLW 0934+15a | M2 | line splitting; double peak |
| SLW 0734+28a | M | line splitting, wide CCF |

normalized histogram of the resultant distribution is shown in dotted lines in the right panel of Figure 4.4. For a quantitative assessment of the difference between the simulated and observed $\Delta V_r$ distributions, we performed the Kolmogorov-Smirnov test (Press et al. 1992) and found a 0.93% probability that the two were drawn from the same parent population. We conclude the $\Delta V_r$ distribution of our observed binaries is much narrower than the scatter expected of two unassociated stars.

Thirteen (12.6%) of the pairs have $V_r$ that disagree at $>3\sigma$. The SLoWPoKES catalog only contains pairs with probability of chance alignment, $P_f$, less than 5%, meaning fewer than five of 103 pairs were expected to be false positives. In fact, $P_f$ was tabulated for each pair in Chapter II; the cumulative sum of chance alignments was only 0.3%, implying <1 pair was expected to be false positives. As shown in the left panel of Figure 4.5, there is no trend in $\Delta V_r$ as a function of the $P_f$. There are discrepant pairs at all values of $P_f$. However, as can be seen in the right panel of Figure 4.5, there is a significant trend of $\Delta V_r$ with the S/N in the spectra. The pairs with the largest $\Delta V_r$ values are at low S/N while there are no discrepant pairs at high S/N. This suggests that the cross-correlation process and the measurements of $V_r$ might have been adversely affected by the noise, yielding noisier radial velocities. In addition, given the large higher-order multiplicity fraction seen in SLoWPoKES (45%; Law et al. 2010), the presence of more SBs in our observed sample cannot be ruled

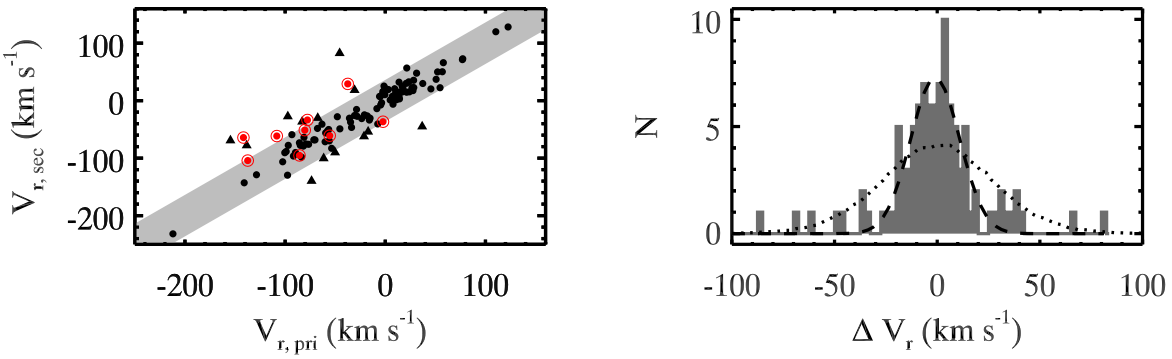


Figure 4.4: *Left*: The radial velocity of the primary and the secondary components: the pairs with $\Delta V_r > 3\sigma$ are shown as triangles while the candidate spectroscopic binaries, shown as red concentric circles, have larger $\Delta V_r$. *Right*: The distribution of difference in radial velocities between components of SLoWPoKES pairs observed in this program, with the Gaussian fit shown in dashed lines. 85% of the sample has $\Delta V_r \leq 3\sigma$. All pairs with $\Delta V_r$>50 km s$^{-1}$ have relatively low S/N.. The expected intrinsic scatter in $\Delta V_r$ for two unassociated stars in the same 3-d position in the Galaxy and have matching proper motions, as calculated using the Galactic model from Chapter II is shown with dotted lines; it is a much larger dispersion compared to our observed sample of CPM pairs.

out by our low-resolution spectra.

In summary, the vast majority of the sample pairs show agreement in their radial velocities, as expected for physical binaries. Pairs with discrepant $V_r$s have spectra with low observed S/N or are (candidate) hierarchical systems with a spectroscopic binary.

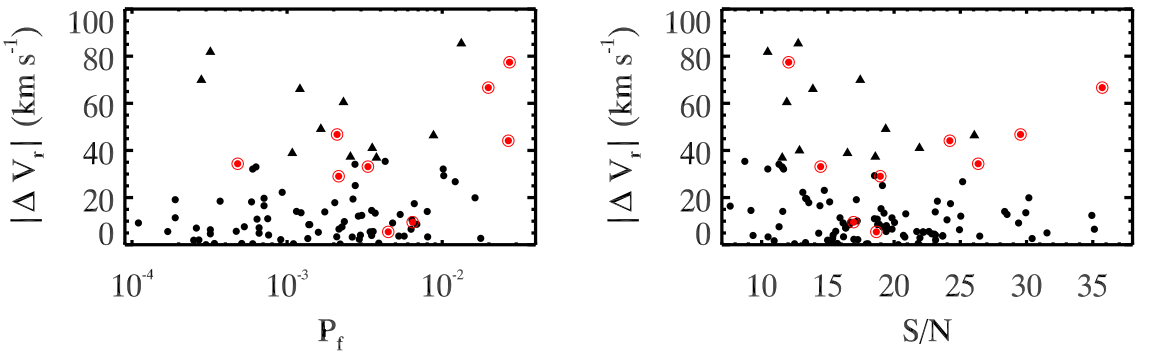


Figure 4.5: *Left:* The probability of chance alignment ($P_f$) calculated using the Galactic model by Chapter II vs. the difference in radial velocity between components for 113 SLoWPoKES CPM pairs observed in this program. *Right*: Systems with a lower S/N (red) have a higher dispersion in $\Delta V_r$, suggesting the observed discrepancy might be due to the lower S/N. Candidate SBs are shown as red, concentric circles while pairs with $\Delta V_r > 3\sigma$ are shown as triangles.

### 4.3.3 Metallicity Index Calibration

Figure 4.6 shows the observed SLoWPoKES pairs, with the components of each pair connected with a solid line, in the CaH–TiO space with the dotted lines showing the iso-$\zeta_{\rm TiO/CaH}$ lines for $\zeta_{\rm TiO/CaH}$ = 0.1–1.5 in steps of 0.1. The solid lines delineate the boundary between the dM/sdM/esdM/usdM classes ($\zeta_{\rm TiO/CaH}$ = 0.825, 0.500, and 0.200, respectively); the single-star spectral standards for the sdM (diamonds), esdM (triangles), and usdM (squares) classes are also shown (LRS07). For clarity, only pairs whose error bars, in both CaH and TiO5 of both pairs, are smaller than the median error are plotted. Most of the observed pairs are dMs, i.e., part of the thin disk with roughly solar metallicity. This is not surprising for a bright sample located within ∼200–300 pc of the Sun as the local neighborhood is largely dominated by thin disk stars (Bochanski et al. 2010).

Most of the binary pairs lie parallel to the iso-$\zeta_{\rm TiO/CaH}$ lines, within the error bars. The inset in Figure 4.6 shows the distribution of $\Delta\zeta$, which is centered around zero but has substantial scatter. Quantitatively, the median and median absolute deviation (m.a.d.) are -0.005 and 0.066, respectively, indicating that for the vast majority of the observed pairs, $\zeta_{\rm TiO/CaH}$ is a correctly infers a common metallicity for the two stars in each pair.

To test whether the observed $\Delta\zeta$ distribution was merely the intrinsic scatter in $\Delta\zeta$, we randomly selected 113 pairs of disk stars ($\zeta_{\rm TiO/CaH}$ = 0.825–1.100) in the similar brightness range as the SLoWPoKES sample ($r < 20$) and with high proper motions ($\mu \geq 40$ mas yr$^{-1}$) from the SDSS spectroscopic catalog (West et al. 2011) and calculated the $\Delta\zeta$ distribution. There were 8030 stars in the DR7 spectroscopic sample that met these criteria; 113 pairs were randomly selected from this sample and their $\Delta\zeta$ distribution calculated. We performed this simulation $10^5$ times; the resultant distribution is plotted in red in the inset of Figure 4.6. The simulated $\Delta\zeta$ distribution is less centrally peaked, and much broader, compared to our observed distribution. The Kolmogorov-Smirnov test (Press et al. 1992) finds a probability of $3.3\times10^{-25}$ that the two distributions were drawn from the same parent population. We conclude that the metallicity of components of SLoWPoKES binaries observed in this program are more similar to each other than that of two randomly paired thin disk stars. As components of a binary system are expected to have formed of the same material, this further serves to confirm the physical association of the pairs. Furthermore, it strengthens

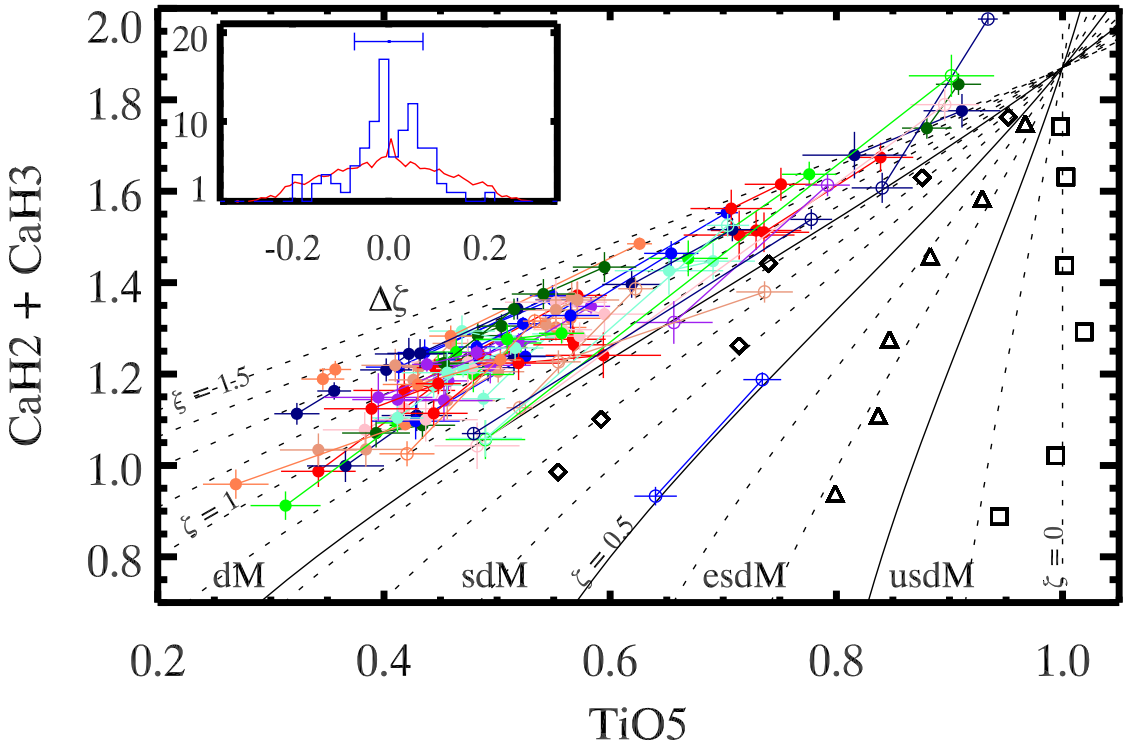


Figure 4.6: Distribution of the observed M dwarf binaries, with components of a system connected by solid lines, in the CaH/TiO space confirms the iso-$\zeta_{\rm TiO/CaH}$ contours with $\zeta_{\rm TiO/CaH}$ = 0.0, 0.1, 0.2, ..., 1.5 (dotted lines), albeit with some deviation at the highest values (towards top right). The distribution of $\Delta\zeta$ (blue histogram; inset) peaks at ∼0 and is significantly different from a distribution for two randomly paired dMs (red solid line). However, the scatter in $\Delta\zeta$ is large; the bar at the middle-top of the inset shows the scatter in the error of $\Delta\zeta$ ($\sigma_{\Delta\zeta}$). The solid contours demarcate the boundary between the dM/sdM/esdM/usdM classes while the K7–M5 spectral standards for the sdM (diamonds), esdM (triangles), and usdM (squares) classes are shown (LRS07). Early-type M stars are at the upper right, late-types at the lower left.

the argument that $\zeta_{\rm TiO/CaH}$ is a reliable proxy for relative metallicity.

However, Figure 4.6 also demonstrates some deficiencies in the definition of $\zeta_{\rm TiO/CaH}$. First, $\Delta\zeta$ is more than three m.a.d. away from zero for ∼18% of the pairs, versus the ∼5% expected for a normal distribution. They are discrepant especially at large values of TiO5 and CaH2+CaH3, i.e., for higher-mass M dwarfs, perhaps suggesting a break in the $\zeta_{\rm TiO/CaH}$ relation. Large errors in this regime further complicate the issue, as the discrepant $\zeta_{\rm TiO/CaH}$ values could result from the difficulty of measuring the shallower TiO5, CaH2, and CaH3 band heads in late-K and early-M dwarfs. It is also evident how the iso-$\zeta_{\rm TiO/CaH}$ contours converge at the higher masses as pointed out out by LRS07. On the other hand, the

Table IV.5. Coefficients, $a_N$, for Eq (4.2)

| Coefficients | LRS07 | This study |
|---|---|---|
| $a_0$ | − 0.050 | − 0.047 |
| $a_1$ | − 0.118 | − 0.127 |
| $a_2$ | + 0.670 | + 0.694 |
| $a_3$ | − 0.164 | − 0.183 |
| $a_4$ | ··· | − 0.005 |

discrepancy persists for the higher-mass pairs with smaller error bars, as can be clearly seen in Figure 4.6. Second, and perhaps more importantly, our measured $\zeta_{\rm TiO/CaH}$ values increase and become super-solar (i.e., $\zeta_{\rm TiO/CaH} > 1$) for the higher mass stars. This is inconsistent with the expectation: given the apparent magnitude constraints ($r \sim 15$–$17$), the higher mass stars in this sample can be expected to be farther away and, hence, at larger Galactic heights given most of the SDSS sight lines are at at high Galactic latitudes (Ivezić et al. 2008b). Stars at high latitudes are, on average, older; and consequently, if anything, they might be expected to have lower metallicities (West et al. 2008). Yet, the $\zeta_{\rm TiO/CaH}$-index yields the opposite. This result necessitates a redefinition of $\zeta_{\rm TiO/CaH}$. With a spectroscopic sample of 113 visually resolved binaries, we are in an unique position to modify the definition of $\zeta_{\rm TiO/CaH}$.

Given the lack of subdwarf pairs in our sample, any recalibration of $\zeta_{\rm TiO/CaH}$ would be systematically biased to high metallicity. Hence, we conducted a search for companions around the subdwarfs ($\zeta_{\rm TiO/CaH} < 0.825$) in the SDSS DR7 spectroscopic catalog (West et al. 2011) with extant SDSS spectra. We have identified a sample of ten pairs with low values of $\zeta_{\rm TiO/CaH}$; and they are shown as open circles in Figure 4.6. The full sample that was identified in the search will be presented in a future paper (Dhital et. al., *in preparation*). One of the added pairs is at the sdM/esdM boundary while the other nine are at the dM/sdM boundary. While small this sample provides an invaluable constraint in the low-metallicity regime.

LRS07 defined $\zeta_{\rm TiO/CaH}$ as:

$$\zeta_{\rm TiO/CaH} = \frac{1 - {\rm TiO5}}{1 - [{\rm TiO5}]_{Z_\odot}}, \tag{4.1}$$

where $[{\rm TiO5}]_{\rm Z_\odot}$ is a third-order polynomial of (CaH2+CaH3):

$$[{\rm TiO5}]_{\rm Z_\odot} = \sum_N a_N ({\rm CaH2} + {\rm CaH3})^N, \tag{4.2}$$

and where the coefficients, $a_{\rm N}$, are tabulated in Table IV.5 and were obtained as a single fit to the TiO5 index as a function of CaH2+CaH3 index for kinematically-selected sample of thin disk stars.

We can recalibrate $\zeta_{\rm TiO/CaH}$ by varying the functional form of $[{\rm TiO5}]_{\rm Z_\odot}$ in Eq. (4.2) such that the scatter in the $\Delta\zeta$ distribution is minimized and distributed around zero. As noted earlier, the LRS07 definition, to first-order, is a robust measure of relative metallicity; and a recalibration need only be a perturbation about that definition. Moreover, as the definition was based on the distribution of (TiO5, CaH2+CaH3) of disk stars, it is a good starting point for the recalibration. So we only chose to explore the coefficient values within $\pm 0.03$ of the LRS07 values in steps of $\Delta = 0.001$. We have introduced a fourth-order term Eq. (4.2), with an initial guess of zero, based on the observed deviation of higher-mass pairs from the iso-$\zeta_{\rm TiO/CaH}$ lines. The best fit values for the coefficients were found by minimizing $\chi^2$, where $\Delta\zeta = 0$ was assumed to be the model. All dM/sdM pairs, except for the ones with the large error bars, were considered for the fit.

Figure 4.7 shows the new iso-$\zeta_{\rm TiO/CaH}$ contours, with the coefficients tabulated in Table IV.5. The contours look significantly different despite small changes in the coefficients, reflecting the very sensitive dependence of $\zeta_{\rm TiO/CaH}$ on its independent variables. The differences can be summarized as:

1. The scatter in the $\Delta\zeta$ is smaller, with the m.a.d. decreasing from 0.060 to 0.044. There are fewer outliers as well, with the values converging towards $\Delta\zeta = 0$. As the median error in $\Delta\zeta$ is bigger than the scatter in $\Delta\zeta$, decreasing the scatter further is not possible unless higher S/N data are obtained. The $\Delta\zeta$ distribution is much more

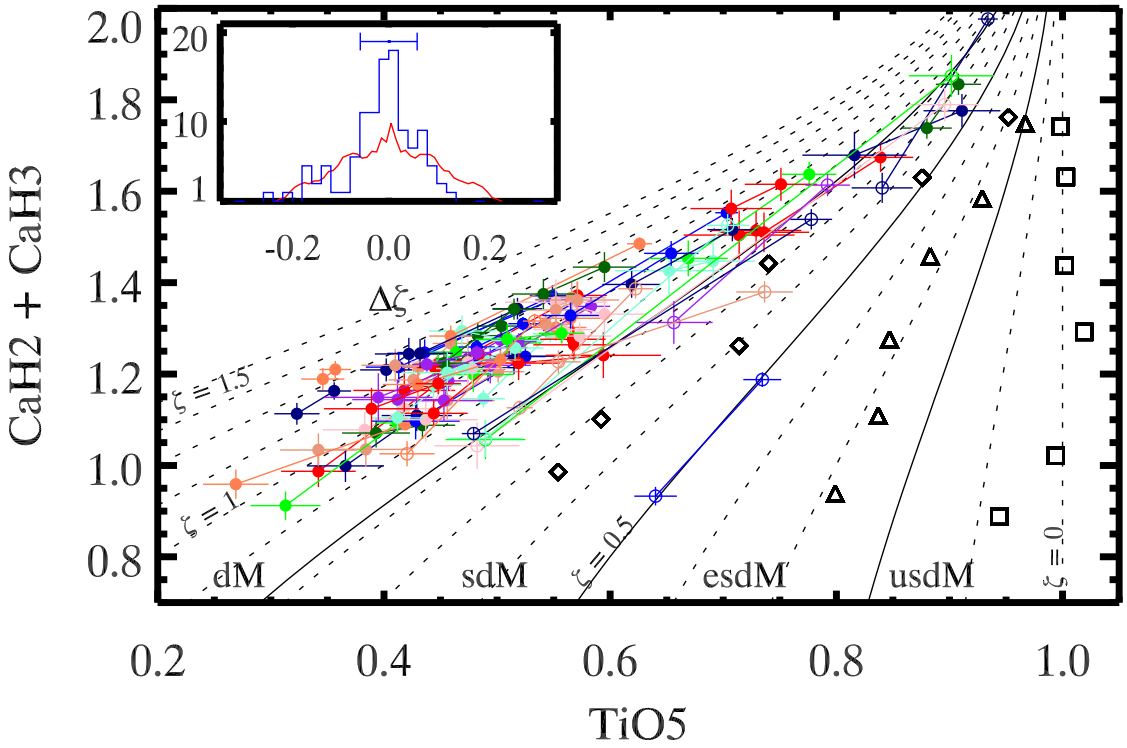


Figure 4.7: Same as Figure 4.6 but with the redefined $\zeta_{\rm TiO/CaH}$, which was done by adding a fourth-order term in Eq. (4.2) and refitting the coefficients by perturbing about the LRS07 values. The new definition of $\zeta_{\rm TiO/CaH}$ minimizes the scatter in the $\Delta\zeta$ distribution and yields lower metallicity for stars at larger Galactic heights, which are expected to be older and have a lower metallicity. The $\Delta\zeta$ distribution is now also much more centrally peaked compared to random pairings of unassociated stars (compare to inset of Figure 4.6.

centrally peaked compared to randomly paired field stars.

2. With only a few pairs at the higher-masses (large TiO5), $\zeta_{\rm TiO/CaH}$ yields more consistent values between components of the higher-mass dMs than in the original LRS07 definition. This congruence is important if we are to have the same metallicity proxy for all low-mass stars and is likely to improve as more pairs are added to that locus. It is especially reassuring to get the same value of $\zeta_{\rm TiO/CaH}$ for the components of pairs with large differences in mass, CaH2+CaH3, and TiO5; the previous definition such pairs were especially discrepant as the primary was assigned a artificially super-solar $\zeta_{\rm TiO/CaH}$. With the new definition, the higher-mass dMs instead have slightly sub-solar $\zeta_{\rm TiO/CaH}$, which is what is expected for stars at larger Galactic heights.

3. The new iso-$\zeta_{\rm TiO/CaH}$ contours are less crowded at the higher-mass regime, allowing for a more robust determination of metallicity. In fact, the iso-$\zeta_{\rm TiO/CaH}$ do not converge before (TiO5, CaH2+CaH3) = (1,2), hence, expanding the regime for sdMs/esdMs/usdMs. The metallicity classes also become more sensitive to TiO5 relative to CaH2+CaH3. However, with the new contours for $\zeta_{\rm TiO/CaH}$, the previously defined standards for the metallicity classes are assessed to be more metal-poor and no longer are in the same class. While this argues for a definition of new standards, we advise against such a revision until there are more subdwarf binaries to more robustly calibrate the contours in that regime.

In general, the new definition of $\zeta_{\rm TiO/CaH}$ better fits the observed sample of visual binaries as well as resolving outstanding issues at the high-mass end. However, due to a paucity of subdwarf pairs, it leaves the low-metallicity regime rather unconstrained. $\zeta_{\rm TiO/CaH}$ looks to be a good proxy for metallicity, and future observations of subdwarf pairs should calibrate it for all low-mass stars. Studies that are using subdwarf binaries (Dhital et al., *in preparation*) and F/G–K/M binaries (Bochanski et al. *in preparation*; Lepine et al. *in preparation*) are already underway and are part of a larger effort to measure the absolute metallicity of low-mass stars.

#### 4.3.4 H$\alpha$ Activity

As M dwarf photospheres are too cold to excite electrons into the $n = 2$ level, any observed H$\alpha$ feature, either in absorption or in emission, is chromospheric in origin. The weakest chromospheres will exhibit no H$\alpha$; as the activity levels increase, H$\alpha$ will be observed in absorption with the line filling in and eventually going into emission for the most active M dwarfs (Stauffer & Hartmann 1986; Cram & Giampapa 1987; Walkowicz & Hawley 2009). As H$\alpha$ is in absorption for both inactive and moderately active M dwarfs, H$\alpha$ emission has traditionally been used as the tracer of chromospheric activity and is biased towards the most active M dwarfs (e.g., West et al. 2011).

In our sample, 11 of the 113 pairs showed clear evidence of H$\alpha$ emission in both components while three pairs had only one component with H$\alpha$ in emission. In addition, 33 pairs

showed H$\alpha$ absorption in both components and 22 pairs in one component; the remaining 47 were classified as inactive. The large fraction (39%) of stars with H$\alpha$ absorption is in accordance with the nearby M dwarfs in the Palomar/MSU Nearby Star Survey Spectroscopic Survey (Gizis et al. 2002). Overall, for 91 of the 113 (81%) pairs in our sample, both components of a pair showed similar levels of activity—in emission, absorption, or the lack or activity. For the pairs with both components having H$\alpha$ emission, we converted the equivalent width in H$\alpha$ to $L_{H\alpha}/L_{bol}$—the ratio of H$\alpha$ luminosity to the bolometric luminosity that is independent of spectral type—following Walkowicz et al. (2004) and West et al. (2004); all pairs had comparable levels of $L_{H\alpha}/L_{bol}$ within the error bars except for the two where the active primary was identified as a candidate SB and had an inactive secondary. The tidal forces due to the tight companion has presumably enhanced the activity of the primary (Shkolnik et al. 2010; Silvestri et al. 2006).

As H$\alpha$ activity depends strongly on mass (West et al. 2008), one way to compare the intrinsic variability in activity levels is by only looking at pairs with components of similar masses. All sixteen pairs with H$\alpha$ in emission or absorption in both components and with similar colors ($\Delta(r-z) < 0.2$) had H$\alpha$ equivalent widths within 130% of each other. Compared to the 200–300% difference in H$\alpha$ activity exhibited by M dwarfs over time (Bell et al. 2012), the components of the similar-mass binary pairs in our sample exhibit a much smaller difference in H$\alpha$ activity. This is consistent with the expectation that stars of similar ages and masses have comparable activity levels, presumably because they experience similar spin-down rates.

## 4.4 Conclusions

We have carried out a spectroscopic follow-up study of 113 ultra-wide, low-mass CPM binary systems from the SLoWPoKES catalog (Chapter II) using the GOLDCAM spectrograph on the KPNO 2.1 m telescope. We measured the radial velocities of each component by cross-correlating them with appropriate standards and used them to assess the fidelity of pairs in the SLoWPoKES catalog. 95 of the 113 (84%) of the pairs have the same radial velocity within 3 $\sigma$. At least five of the pairs with discrepant radial velocities are candidate SBs, which would explain the difference. There may be additional spectroscopic compan-

ions undetected in our low-resolution spectra. Law et al. (2010) found that 45% of the SLoWPoKES systems are either hierarchical triples or quadruples. Either high-resolution spectroscopy or imaging would be needed to identify the close companions and to further quantify the incidence of higher-order systems in wide binaries.

We examined the H$\alpha$ activity in our observed sample. The components of binary pairs exhibited overwhelmingly comparable levels of H$\alpha$ activity. Moreover, the $\Delta$H$\alpha$ of the pairs with similar $r - z$ colors and two active components, while large, was several times smaller than the variation seen in single M dwarfs. Our results corroborate that low-mass stars of the same mass should spin-down at the similar rates over time. However, larger samples of active are needed to confirm this finding and to constrain the rate of this spin-down.

We tested the LRS07 $\zeta_{\rm TiO/CaH}$-index and found that, to first-order, it is a robust measure of relative metallicity. The value of $\zeta_{\rm TiO/CaH}$ for the two components in each binary system match within the error bars for most pairs, indicating a common metallicity as expected. However, we find a systematic bias for the higher-mass M dwarfs such that $\zeta_{\rm TiO/CaH}$ overestimates the metallicity. Assuming all of the pairs are physically associated systems and have the same metallicity, we have redefined $\zeta_{\rm TiO/CaH}$. While the shift is small, it better represents iso-metallicity lines in the high-metallicity regime and represents an incremental step towards defining an absolute metallicity scale for low-mass dwarfs. Planned further observations should extend the calibration of $\zeta_{\rm TiO/CaH}$ as well as map it to an absolute metallicity scale in the near future.

# CHAPTER V

# CONCLUSIONS

A large number of ultra-wide binary stars had been observationally identified over the past few decades (e.g., Luyten 1997; Chanamé & Gould 2004; Lépine & Bongiorno 2007), but their existence remained an enigma. Often larger than or similar in size to the molecular clouds from which they were supposed to have formed, how initially formed and how they continued to survive dynamical interactions with other stars or potentials in the Galaxy was not understood. Similarly, the largest M dwarf binary samples numbered around 100 systems (e.g., Delfosse et al. 2004), severely limiting statistical studies of the lowest mass and most numerous stellar constituents of the Galaxy. Their intrinsic faintness had limited detection of larger samples. The primary foci of my dissertation were to fill these two voids by identifying a large catalog of ultra-wide, low-mass binaries so as to (i) probe the formation and dynamical evolution of the ultra-wide systems and (ii) use the binary systems as coeval laboratories to calibrate and constrain fundamental properties—specifically, metallicity and age—of low-mass stars.

## 5.1 Summary of Dissertation

We created the SLoWPoKES catalog of 1342 ultra-wide binaries—currently, the largest catalog of wide stellar binaries ever assembled—with projected physical separations of $\sim 10^{3-5.5}$ AU (Dhital et al. 2010). They were identified based on their common distances and proper motions using restrictive matching criteria so as to ensure a high level of fidelity in the resulting catalog. Only pairs with a probability of chance alignment, as assessed by our Galactic model, of <5% were included. Followup spectroscopic observations have since verified the fidelity of the catalog: radial velocities were consistent within the errors for >88% of the observed pairs (Dhital et al. 2012). Despite limitations imposed by proper motion and faintness limits, SLoWPoKES contains a wide variety of pairs at distances up to ∼800 pc:

low-metallicity subdwarf–subdwarf, FGK–M dwarf, and white dwarf–M dwarf systems that have already facilitated a wide range of studies.

We built a Galactic model, based on empirical stellar number density (Jurić et al. 2008; Bochanski et al. 2010) and space velocity (Bochanski et al. 2007a) distributions, to quantify the chance alignment probability for each candidate pair. The Monte Carlo-based model generates and repopulates the stellar distribution in six-dimensional phase space around the given location in the Galaxy. The resultant distribution closely mimics both the spatial and kinematic distributions observed in SDSS. In addition to SLoWPoKES, the Galactic model has already seen implementation in a number of other studies: to assess the fidelity of wide brown dwarf pairs (Burgasser et al. 2009; Dhital et al. 2011a), to differentiate thin disk stars from thick disk stars (Irwin et al. 2011), to predict the distribution of low-mass stars in the upcoming LSST survey (Dhital et al. 2011b), and to identify WD–WD pairs (Andrews et al. 2012).

We also reported the discovery of a wide VLM binary, 2MASS J01303563−4445411, based on NIR imaging and spectroscopic observations. At 130 AU, this system is much tighter than the stellar wide binaries discussed above; but the lower system mass makes it just as fragile. As only one of ten VLM binaries wider than 100 AU, 2MASS J0130−4445 helps put strong constraints on formation mechanisms. Moreover, it is only one of six such "grown-up" systems to have survived dynamical ejections and/or interactions and now are in the field. It is part of emerging evidence that not all VLM systems are the result of ejected protostellar systems and multiple formation processes are responsible for the formation of VLMs.

With followup spectroscopic observations of 113 K7–M4 pairs, we found that the $\zeta_{\rm TiO/CaH}$ index (LRS07) yields consistent values for most of our observed sample of M dwarfs, i.e., it is a good tracer of relative metallicity in M dwarfs. However, $\zeta_{\rm TiO/CaH}$ systematically overestimated the metallicity for the early-type M dwarfs. We refined the definition of $\zeta_{\rm TiO/CaH}$ assuming iso-metallicity for components of the observed wide pairs. This yielded significantly better metallicity estimates and also reduced the scatter in the $\Delta\zeta$ distribution for the entire sample. Given $\zeta_{\rm TiO/CaH}$ was initially defined based on a kinematic ensemble of M dwarfs (LRS07), the need for redefinition of $\zeta_{\rm TiO/CaH}$ is not surprising. Moreover,

temperature, metallicity, and gravity probably all affect the CaH and TiO molecular bands (e.g., Jao et al. 2008). So further refinement of $\zeta_{\rm TiO/CaH}$ as binaries of a wide temperature and metallicity ranges are observed is likely. In fact, different definitions of $\zeta_{\rm TiO/CaH}$ for different regimes would not be completely surprising.

### 5.1.1 Formation of Ultra-wide Binaries

One of the key science results from the SLoWPoKES wide binaries was the indication that there are two distinct dynamical populations: (i) tightly-bound "wide" systems ($a \sim 10^3$ AU) that are dynamically stable over >10 Gyr and (ii) loosely-bound systems "ultra-wide" ($a \sim 10^5$ AU) that dissipate in 1–2 Gyr. Age is the obvious explanation for these two populations, where ultra-wide binaries are all young and dissipate over time as they traverse the Galaxy. Another explanation is that the ultra-wide binary population is intrinsically different from the wide population. In other words, there is something fundamentally different about how the ultra-wide binaries were formed.

Our high-resolution imaging of SLoWPoKES binaries found an enhanced multiplicity in the components of wide binaries. Moreover, the multiplicity increases from ∼20% at wide binary separations of ∼1000 AU to ∼80% at ∼5000 AU (Law et al. 2010). First, this immediately suggests that the two groups of binaries were formed differently. Second, while not probing the same regime, this strongly suggests that the widest binaries survive dynamical interactions due to the presence of extra stars in the system. The increase in total system mass by 50–100% significantly lengthens the dissipation timescale of wide binaries, based on comparisons with calculations of Weinberg et al. (1987).

The bimodal population of SLoWPoKES binaries closely resembles the result of N-body simulations where the binaries wider than $\sim 10^3$ AU are almost always formed from stars ejected from protostellar clouds or evaporated from open clusters (Kouwenhoven et al. 2010; Moeckel & Clarke 2011). Multiplicity in wide binaries formed via cluster dissipation should resemble that of the field stars, inconsistent with the enhanced multiplicity we found in Law et al. (2010). However, the physical separation of the inner binaries is peaked strongly at $\lesssim$30 AU (Law et al. 2010), consistent with cluster dissipation. As discussed in Chapter III, wider binaries would have been disrupted before they could get bound with a wide tertiary.

The enhanced multiplicity among the widest binaries, however, is consistent with the premise that the widest binaries were formed via dynamical widening of primordial triples and quadruples, where angular momentum was transferred from the inner orbits to the outer ones. However, even at the widest separations, not every wide binary is a multiple; so not all wide binaries are formed via dynamical widening. The effectiveness of the widening also needs to be more rigorously studied, as the widest identified systems are almost a parsec wide.

In conclusion, there seems to be tantalizing evidence that not all binary systems are formed in a similar manner. Our results do not rule out either dynamical widening or cluster dissipation as a mode for wide binary formation. Rather, both processes could be producing wide binaries and shaping the bimodality in observed distributions. To further characterize the population and distinguish between the two scenarios, a comprehensive measurement of higher-order multiplicity is needed. We also recommend a direct comparison with N-body simulations to assess the viability of ejected or evaporated stars getting bound during cluster dissipation.

## 5.2 Future Work

### 5.2.1 SLoWPoKES-II: A Larger Catalog of Wide Binary Systems

As discussed in Chapter II, the binary pairs in the SLoWPoKES catalog were selected using very restrictive criteria so that the false positive rate would be very low. Such a "pure" catalog would allow for efficient followup observations. However, that approach implies that there are a lot of false negatives, i.e., SLoWPoKES is missing a large number of wide binaries. Assembling a larger catalog, albeit with a higher false positive rate, would allow for statistically constraining the wide binary fraction as well as probing formation scenarios by looking at "complete" population distribution. Followup studies that target exotic populations (e.g., halo binaries) would have access to a larger pool of binaries Their rarity means such programs can afford a larger false positive rate.

There are two ways to expand the sample: (i) simply relax the selection criteria used in Chapter II or (ii) identify binaries withput using proper motions. Selection criteria can

lowered by either lowering the cutoff on probability for change alignment (currently $\leq 5\%$) or accepting candidates with larger differences in proper motion (currently $\leq$ 1-$\sigma$); both could potentially help identify many more binary pairs. However, as can be seen in Figure 2.1, we only searched for companions around $\sim$500,000 of the $\gtrsim$50 million low-mass stars that have excellent photometry. We could not search for companions around the rest of the stars due to lack of proper motions. The proper motions were not available for: (i) stars fainter than $r \sim 20$, (ii) the majority of stars moving faster than $\sim$100 mas yr$^{-1}$, and (iii) stars with another point source within $7''$. These incompletenesses arise mainly because of the limitations of the USNO-B catalog (see Chapter II and Munn et al. (2004) for further details). Therefore, the greatest potential in identifying a larger catalog of wide binaries lies in finding physically associated pairs without proper motions.

Identifying stellar binaries based on just their 3D position in the Galaxy is not trivial, especially when the distances are based on photometric parallax relations with $1\sigma$ errors of $\sim$14%. Cross-correlation techniques have previously been used to identify ensembles of binary candidates, albeit with large false positive rates by finding the excess of pairs (e.g., Bahcall & Soneira 1981, also see Section 1.5). However, we want to identify individual binary pairs with a high level of fidelity. We showed in Figure 2.5 that for our high proper motion ($\mu \geq 40$ mas yr$^{-1}$), bright ($r \leq 20$) sample that adding the proper motion cuts made virtually no difference at $\theta \leq 15''$ and very little difference at $15'' < \theta \leq 30''$. This analysis was based on actual SDSS data over 1600 LOS where candidate binaries were identified. While counter-intuitive at first, this makes sense as the density of stars in 3D volume is rather low: $\sim$0.14 stars pc$^{-3}$ in the Solar neighborhood, which is only 15 pc from the Galactic Plane. This decreases exponentially with Galactic height. Therefore, in theory, at least, it should be possible to identify individual binary pairs based 3D position of stars. While this will not hold along all LOSs (e.g., along the Galactic Plane), our Galactic model can be used reject those LOSs.

Given the various problems and biases inherent in the SDSS proper motion catalog (see Chapter II), the results would be more robust if we were able to not depend on proper motions at all, even to select the initial sample that would searched around. One potential problem with searching for all stars, without regard to kinematics or magnitude, is that

SDSS goes 2.5 mag fainter than we probed in SLoWPoKES. As the photometric distances have relatively large error bars, the contamination by stars that physically in the halo is high.

We searched at $0\farcs4 \leq \theta \leq 15''$ around all 110 million low mass stars ($r - i > 0.54$ and $i - z > 0.31$; Bochanski et al. 2010) with excellent photometry in the SDSS DR8 photometric catalog (Aihara et al. 2011). The lower limit for $\theta$ was empirically determined by looking at how the SDSS pipeline classifies PRIMARY and SECONDARY point sources at close separations. The upper limit of $15''$ was based on our results from Chapter II. Given the logistical challenge involved with such a large search, we used the NEIGHBORS table in our CasJobs query[1], instead of the STAR table that we used Chapter II.

The preliminary results show that we can successfully identify binary pairs at the smaller angular separations. The signature of the presence of binaries, excess at close angular separations, is clearly identifiable. It dominates the expected number of chance alignments ($\propto \theta^2$). However, the number of chance alignments soon grows and dominates the distribution at $\theta \gtrsim 8$–$10''$. While the Galactic model can sift the worst offenders, we need to understand and correct for the reason why the chance alignments dominate at $\theta \gtrsim 8$–$10''$.

One solution is to restrict the search, at least initially, to the stars that are $\lesssim 1000$ pc away. By definition, the candidate companions will also at those distances. Our photometric distances are based on the $r-z$ color, so we can use the position of the companions in $u-g$, $g-r$, or $g-i$ color spaces to reject chance alignments that are at different distances. Another way is to probe the companions found at larger separations and look at how they differ from the ones at smaller separations. While there is no reason to believe that they would occupy different parameter spaces (e.g., in Galactic height, mass ratios, projected physical separations), it should be possible to sift the chance alignments. Alternatively, we can use a brightness cut of $r \leq 20$, as in Chapter II which would solve a large part of the problem. However, we want to avoid introducing additional biases to our resultant catalog as a result of "artificial" restrictions, unless they are absolutely necessary.

SLoWPoKES-II is going to be $\sim$100–1000$\times$ larger than SLoWPoKES, i.e., it will comprise of $10^{5-6}$ binary systems. This estimation is based mostly on pairs found at $0\farcs4 \leq \theta \leq 8''$.

[1] `http://skyservice.pha.jhu.edu/casjobs/`

While the absolute number of binaries seems enormously high, it only represents a binary fraction of $\lesssim$1% as we searched around 119 million stars. Compared to SLoWPoKES, we are also probing the central parts of the log-normal distribution of binary semi-major axis, assuming it peaks at ∼30 AU (Fischer & Marcy 1992). Hence, it is expected that we find a lot more pairs. As most of our initial sample is at 200–300 pc, we are sensitive to binaries as close as 80–120 AU, an order of magnitude lower than SLoWPoKES.

In conclusion, we are assembling a followup catalog, SLoWPoKES-II, that will be orders of magnitude larger. The identification process is based only on 3D position in the Galaxy and does not depend on *any* kinematic information. Hence, we can only search at relatively small angular separations, up to $\theta \sim 15''$. Currently, the identified candidate companions are dominated by chance alignments at the larger angular separations. The pairs found at the smaller separations, however, have a high probability of being real, physically associated binary systems.

### 5.2.2 Wide Binaries as Probes of Theories of Gravitation

The SLoWPoKES binaries are so extremely wide that their orbital acceleration is smaller than the critical level where the effects of modified gravity theories (e.g., MOND; Bekenstein 2004) are discernible. In theory, MOND gravity would be stronger than Newtonian gravity for a ∼7,000 AU binary with a total system mass of 1 $M_\odot$ (Hernandez et al. 2011). For the above binary, the predicted orbital velocity are ∼1000 m $s^{-1}$ for MOND as compared to ∼100 m $s^{-1}$ for Newtonian gravity. Thus, such ultra-wide binaries are novel experimental laboratories in the local Universe to test theories of gravitation and distinguish between them. The stronger MOND gravity also provides an alternative explanation for the continued survival of the ultra- wide binaries in the field. There are two ways to discriminate between theories of gravity using wide binaries. First, a robust measurement of orbital motions of these binaries ($\lesssim$100 m $s^{-1}$) could be made. While this level of precision is achievable with the current generation of ground telescopes, the SLoWPoKES systems are faint and would require long integrations to get the needed signal-to-noise. Extremely precise proper motions and/or radial velocities for a large number of stars are expected to be measured by upcoming/planned missions like LSST (precision of ∼1 mas $yr^{-1}$; Ivezić et al. 2008a),

*Gaia* (5–100 $\mu$as yr$^{-1}$; Lindegren et al. 2012), and *SIM PlanetQuest* (sub-$\mu$as yr$^{-1}$; Shao & Nemati 2009). Second, one can evolve a population of wide binaries, with initial conditions constrained by observations, under classical and modified gravity and compare it with the observed distribution. Normally, most predictions of modified gravity theories can only be tested on cosmological scales (e.g., Bertschinger & Zukin 2008). A stellar laboratory to test MOND in the local Universe provides an unique and invaluable opportunity.

### 5.2.3 Wide Binaries as Coeval Laboratories

To be able to characterize stellar populations across the Galaxy, an absolute metallicity scale tied to an easily observable index is required. While we have shown that $\zeta_{\rm TiO/CaH}$ is a reliable tracer of relative metallicity in low-mass dwarfs, it still needs to be calibrated for the entire lower metallicity and temperature regimes and better tied to the absolute metallicity, [Fe/H]. We are conducting spectroscopic observations of thick and halo subdwarf binary candidates at Kitt Peak National Observatory and of mid–late-type M dwarf binaries as part of SDSS-III BOSS (S. Dhital et al. 2012, *in preparation*). To tie the $\zeta_{\rm TiO/CaH}$ index to [Fe/H], we are also conducting observations of FGK–M dwarf binaries (S. Lepine et al. 2012, *in preparation*), where the metallicity of the FGK primary can be measured and assigned the M secondary. While the current $\zeta_{\rm TiO/CaH}$–[Fe/H] relation has a scatter of $\sim$0.3 dex (Woolf & Wallerstein 2005; Woolf et al. 2009), it suggests a better calibration sample that spans the entire metallicity range could reduce the scatter. Lastly, we are conducting high-resolution spectroscopy to identify other metallicity-sensitive features that would give a more robust metallicity indicator (J. Bochanski et al., *in preparation*).

We are also beginning to probe the magnetic activity–rotation–age relation in low-mass stars with the aim of eventually measuring the ages of field stars. We are taking a three-pronged approach to this problem. First, we have begun to extend the gyrochronology technique to stars that are fully convective: Barnes (2003, 2007, 2010) has developed a model to describe the rotational evolution of solar-type stars as a function of age. The model has been empirically tested in young (Meibom et al. 2009, 2011b; Delorme et al. 2011) and old (Meibom et al. 2011a) open clusters of ages $\sim$100 Myr to $\sim$1 Gyr. However, the nature of rotation–age relation the as the stars becoming fully convective is not known.

We are using time-series imaging data of more than thirty FGK–M and M–M wide pairs for which we will measure rotation periods and their gyro-ages. Second, we are using the WD–M dwarf pairs in SLoWPoKES to measure the progenitor cooling age of the primary WD. The combined age can then be assigned to the secondary M dwarf (D. Morgan et al. 2012, *in preparation*). Third, we are working on calibrating the stratigraphic ages for individual stars, which were defined by comparing dynamics of ensembles of M dwarfs with their H$\alpha$ activity (West et al. 2008). This technique only works for stars with measurable H$\alpha$ emission. By combining the results of these three approaches, we are aiming to empirically constrain a robust activity–rotation–age relation for low-mass stars. lastly, Gunning et al. (2012) are conducting time-series spectroscopy of identical twins from the SLoWPoKES catalog to measure the intrinsic variability in H$\alpha$ as well as to study the flare rates.

In conclusion, we identified the largest ever catalog of wide binaries: the Sloan Low-mass Wide Pairs of Kinematically Equivalent Stars (SLoWPoKES). We are probing wide binary formation scenarios with the ensemble of binaries that are now available. It is likely that two (or more) processes are responsible for forming the observed wide binaries. The diverse population of pairs in the SLoWPoKES catalog has started facilitating studies to measure and/or constrain low-mass star parameters (e.g., metallicity, age, rotation, magnetic activity) as well as their dependence upon each other. With a larger sample of wide binaries (SLoWPoKES-II; Dhital et al. 2012, *in preparation*) to be published in the near future, we can look forward to the SLoWPoKES catalogs having an even broader impact in stellar and Galactic astronomy.

REFERENCES


Abazajian, K. N., et al. 2009, ApJS, 182, 543

Abt, H. A., Gomez, A. E., & Levy, S. G. 1990, ApJS, 74, 551

Abt, H. A., & Levy, S. G. 1976, ApJS, 30, 273

Ackerman, A. S., & Marley, M. S. 2001, ApJ, 556, 872

Adelman-McCarthy, J. K., et al. 2008, ApJS, 175, 297

Aihara, H., et al. 2011, ApJS, 193, 29

Allen, C., Poveda, A., & Herrera, M. A. 2000, A&A, 356, 529

Andrews, J., Agueros, M., Belczynski, K., Dhital, S., Kleinman, S., & West, A. 2012, in American Astronomical Society Meeting Abstracts, Vol. 219, American Astronomical Society Meeting Abstracts, #250.06

Arnaboldi, M., Neeser, M. J., Parker, L. C., Rosati, P., Lombardi, M., Dietrich, J. P., & Hummel, W. 2007, The Messenger, 127, 28

Artigau, É., Lafrenière, D., Albert, L., & Doyon, R. 2009, ApJ, 692, 149

Artigau, É., Lafrenière, D., Doyon, R., Albert, L., Nadeau, D., & Robert, J. 2007, ApJ, 659, L49

Bahcall, J. N., Hut, P., & Tremaine, S. 1985, ApJ, 290, 15

Bahcall, J. N., & Soneira, R. M. 1980a, ApJ, 238, L17

——. 1980b, ApJS, 44, 73

——. 1981, ApJ, 246, 122

Baraffe, I., & Chabrier, G. 2010, A&A, 521, A44+

Baraffe, I., Chabrier, G., Allard, F., & Hauschildt, P. H. 1998, A&A, 337, 403

Barnes, S. A. 2003, ApJ, 586, 464

——. 2007, ApJ, 669, 1167

——. 2010, ApJ, 721

Basri, G., & Reiners, A. 2006, AJ, 132, 663

Bastian, N., Covey, K. R., & Meyer, M. R. 2010, ARA&A, 48, 339

Bate, M. R. 2009, MNRAS, 392, 590

——. 2011, MNRAS, 1310

Bate, M. R., & Bonnell, I. A. 2005, MNRAS, 356, 1201

Bate, M. R., Bonnell, I. A., & Bromm, V. 2002, MNRAS, 336, 705

——. 2003, MNRAS, 339, 577

Bean, J. L., Seifahrt, A., Hartman, H., Nilsson, H., Wiedemann, G., Reiners, A., Dreizler, S., & Henry, T. J. 2010, ApJ, 713, 410

Bekenstein, J. D. 2004, Phys. Rev. D, 70, 083509

Bell, K. J., Hilton, E. J., Davenport, J. R. A., Hawley, S. L., West, A. A., & Rogel, A. B. 2012, PASP, 124, 14

Benson, P. J., & Myers, P. C. 1989, ApJS, 71, 89

Berger, E. 2006, ApJ, 648, 629

Berger, E., et al. 2010, ApJ, 709, 332

Bergeron, P., Wesemael, F., & Beauchamp, A. 1995, PASP, 107, 1047

Bertschinger, E., & Zukin, P. 2008, Phys. Rev. D, 78, 024015

Bessell, M. S. 1982, Proceedings of the Astronomical Society of Australia, 4, 417

Bihain, G., Rebolo, R., Zapatero Osorio, M. R., Béjar, V. J. S., & Caballero, J. A. 2010, A&A, 519, A93+

Billères, M., Delfosse, X., Beuzit, J., Forveille, T., Marchal, L., & Martín, E. L. 2005, A&A, 440, L55

Bochanski, J. J., Hawley, S. L., Covey, K. R., West, A. A., Reid, I. N., Golimowski, D. A., & Ivezić, Ž. 2010, AJ, 139, 2679

Bochanski, J. J., Munn, J. A., Hawley, S. L., West, A. A., Covey, K. R., & Schneider, D. P. 2007a, AJ, 134, 2418

Bochanski, J. J., West, A. A., Hawley, S. L., & Covey, K. R. 2007b, AJ, 133, 531

Bond, N. A., et al. 2010, ApJ, 716, 1

Bonfils, X., Delfosse, X., Udry, S., Santos, N. C., Forveille, T., & Ségransan, D. 2005, A&A, 442, 635

Bonnell, I. A. 1994, MNRAS, 269, 837

Bouvier, J., Duchêne, G., Mermilliod, J.-C., & Simon, T. 2001, A&A, 375, 989

Bouvier, J., Rigaut, F., & Nadeau, D. 1997, A&A, 323, 139

Bouy, H., Brandner, W., Martín, E. L., Delfosse, X., Allard, F., & Basri, G. 2003, AJ, 126, 1526

Burgasser, A. J. 2004, ApJS, 155, 191

——. 2007, ApJ, 659, 655

Burgasser, A. J., Cruz, K. L., Cushing, M., Gelino, C. R., Looper, D. L., Faherty, J. K., Kirkpatrick, J. D., & Reid, I. N. 2010, ApJ, 710, 1142

Burgasser, A. J., Cruz, K. L., & Kirkpatrick, J. D. 2007a, ApJ, 657, 494

Burgasser, A. J., Dhital, S., & West, A. A. 2009, AJ, 138, 1563

Burgasser, A. J., Geballe, T. R., Leggett, S. K., Kirkpatrick, J. D., & Golimowski, D. A. 2006, ApJ, 637, 1067

Burgasser, A. J., & Kirkpatrick, J. D. 2006, ApJ, 645, 1485

Burgasser, A. J., et al. 2003a, ApJ, 592, 1186

Burgasser, A. J., Kirkpatrick, J. D., & Lowrance, P. J. 2005, AJ, 129, 2849

Burgasser, A. J., Kirkpatrick, J. D., Reid, I. N., Brown, M. E., Miskey, C. L., & Gizis, J. E. 2003b, ApJ, 586, 512

Burgasser, A. J., Liu, M. C., Ireland, M. J., Cruz, K. L., & Dupuy, T. J. 2008, ApJ, 681, 579

Burgasser, A. J., Looper, D. L., Kirkpatrick, J. D., & Liu, M. C. 2007b, ApJ, 658, 557

Burgasser, A. J., Reid, I. N., Siegler, N., Close, L., Allen, P., Lowrance, P., & Gizis, J. 2007c, in Protostars and Planets V, ed. B. Reipurth, D. Jewitt, & K. Keil (Tucson, AZ: Univ. Arizona Press), 427

Burningham, B., et al. 2010, MNRAS, 404, 1952

Burrows, A., Hubbard, W. B., Lunine, J. I., & Liebert, J. 2001, Reviews of Modern Physics, 73, 719

Burrows, A., Hubbard, W. B., Saumon, D., & Lunine, J. I. 1993, ApJ, 406, 158

Burrows, A., et al. 1997, ApJ, 491, 856

Caballero, J. A. 2007, ApJ, 667, 520

——. 2009, A&A, 507, 251

Carollo, D., et al. 2010, ApJ, 712, 692

——. 2008, Nature, 451, 216

Caselli, P., Benson, P. J., Myers, P. C., & Tafalla, M. 2002, ApJ, 572, 238

Chabrier, G., & Baraffe, I. 2000, ARA&A, 38, 337

Chabrier, G., Baraffe, I., & Plez, B. 1996, ApJ, 459, 91

Chanamé, J., & Gould, A. 2004, ApJ, 601, 289

Chanamé, J., & Ramírez, I. 2012, ApJ, 746, 102

Clarke, C. 1992, in ASP Conf. Ser., Vol. 32, IAU Colloq. 135: Complementary Approaches to Double and Multiple Star Research, ed. H. A. McAlister & W. I. Hartkopf (San Francisco, CA: ASP), 176

Clemens, D. P., Yun, J. L., & Heyer, M. H. 1991, ApJS, 75, 877

Close, L. M., Siegler, N., Freed, M., & Biller, B. 2003, ApJ, 587, 407

Close, L. M., et al. 2007, ApJ, 660, 1492

Connelley, M. S., Reipurth, B., & Tokunaga, A. T. 2008, AJ, 135, 2496

——. 2009, AJ, 138, 1193

Covey, K. R., et al. 2008, AJ, 136, 1778

——. 2007, AJ, 134, 2398

Cram, L. E., & Giampapa, M. S. 1987, ApJ, 323, 316

Cruz, K. L., Reid, I. N., Liebert, J., Kirkpatrick, J. D., & Lowrance, P. J. 2003, AJ, 126, 2421

Cunha, M. S., et al. 2007, A&A Rev., 14, 217

Cushing, M. C., et al. 2008, ApJ, 678, 1372

Cushing, M. C., Rayner, J. T., & Vacca, W. D. 2005, ApJ, 623, 1115

Cushing, M. C., Vacca, W. D., & Rayner, J. T. 2004, PASP, 116, 362

Cutri, R. M., et al. 2003, 2MASS All Sky Catalog of Point Sources. (The IRSA 2MASS All-Sky Point Source Catalog, NASA/IPAC Infrared Science Archive. http://irsa.ipac.caltech.edu/applications/Gator/)

D'Antona, F., & Mazzitelli, I. 1997, Mem. Soc. Astron. Italiana, 68, 807

Delfosse, X., et al. 2004, in Astronomical Society of the Pacific Conference Series, Vol. 318, Spectroscopically and Spatially Resolving the Components of the Close Binary Stars, ed. R. W. Hilditch, H. Hensberge, & K. Pavlovski, 166–174

Delfosse, X., Forveille, T., Perrier, C., & Mayor, M. 1998, A&A, 331, 581

Delgado-Donate, E. J., Clarke, C. J., & Bate, M. R. 2004a, MNRAS, 347, 759

Delgado-Donate, E. J., Clarke, C. J., Bate, M. R., & Hodgkin, S. T. 2004b, MNRAS, 351, 617

Delorme, P., Collier Cameron, A., Hebb, L., Rostron, J., Lister, T. A., Norton, A. J., Pollacco, D., & West, R. G. 2010, in SF2A-2010: Proceedings of the Annual meeting of the French Society of Astronomy and Astrophysics, ed. S. Boissier, M. Heydari-Malayeri, R. Samadi, & D. Valls-Gabaud , 243

Delorme, P., Collier Cameron, A., Hebb, L., Rostron, J., Lister, T. A., Norton, A. J., Pollacco, D., & West, R. G. 2011, MNRAS, 413, 2218

Dhital, S., Burgasser, A. J., Looper, D. L., & Stassun, K. G. 2011a, AJ, 141, 7

Dhital, S., et al. 2011b, LSST Deep-Drilling Field Observations White Papers

Dhital, S., West, A. A., Stassun, K. G., & Bochanski, J. J. 2010, AJ, 139, 2566

Dhital, S., West, A. A., Stassun, K. G., Bochanski, J. J., Massey, A. P., & Bastien, F. A. 2012, AJ, 143, 67

Duchêne, G. 1999, A&A, 341, 547

Duchêne, G., Bouvier, J., Bontemps, S., André, P., & Motte, F. 2004, A&A, 427, 651

Duchêne, G., Bouvier, J., & Simon, T. 1999, A&A, 343, 831

Duchêne, G., Delgado-Donate, E., Haisch, Jr., K. E., Loinard, L., & Rodríguez, L. F. 2007, in Protostars and Planets V, ed. B. Reipurth, D. Jewitt, & K. Keil, 379–394

Duquennoy, A., & Mayor, M. 1991, A&A, 248, 485

Durisen, R. H., Gingold, R. A., Tohline, J. E., & Boss, A. P. 1986, ApJ, 305, 281

Eisenstein, D. J., et al. 2001, AJ, 122, 2267

Enoch, M. L., Evans, II, N. J., Sargent, A. I., Glenn, J., Rosolowsky, E., & Myers, P. 2008, ApJ, 684, 1240

Faherty, J. K., Burgasser, A. J., Cruz, K. L., Shara, M. M., Walter, F. M., & Gelino, C. R. 2009, AJ, 137, 1

Faherty, J. K., Burgasser, A. J., West, A. A., Bochanski, J. J., Cruz, K. L., Shara, M. M., & Walter, F. M. 2010, AJ, 139, 176

Fischer, D. A., & Marcy, G. W. 1992, ApJ, 396, 178

Folkes, S. L., Pinfield, D. J., Kendall, T. R., & Jones, H. R. A. 2007, MNRAS, 378, 901

Fuchs, B., et al. 2009, AJ, 137, 4149

Fukugita, M., Ichikawa, T., Gunn, J. E., Doi, M., Shimasaku, K., & Schneider, D. P. 1996, AJ, 111, 1748

Garnavich, P. M. 1988, ApJ, 335, L47

Geballe, T. R., et al. 2002, ApJ, 564, 466

Gelino, C. R., Marley, M. S., Holtzman, J. A., Ackerman, A. S., & Lodders, K. 2002, ApJ, 577, 433

Ghez, A. M., McCarthy, D. W., Patience, J. L., & Beck, T. L. 1997, ApJ, 481, 378

Ghez, A. M., Neugebauer, G., & Matthews, K. 1993, AJ, 106, 2005

Gies, D. R. 1987, ApJS, 64, 545

Gilmore, G., Wyse, R. F. G., & Kuijken, K. 1989, ARA&A, 27, 555

Gizis, J. E. 1997, AJ, 113, 806

——. 2002, ApJ, 575, 484

Gizis, J. E., Monet, D. G., Reid, I. N., Kirkpatrick, J. D., Liebert, J., & Williams, R. J. 2000, AJ, 120, 1085

Gizis, J. E., Reid, I. N., & Hawley, S. L. 2002, AJ, 123, 3356

Gizis, J. E., Reid, I. N., Knapp, G. R., Liebert, J., Kirkpatrick, J. D., Koerner, D. W., & Burgasser, A. J. 2003, AJ, 125, 3302

Goodwin, S. P., & Kroupa, P. 2005, A&A, 439, 565

Goodwin, S. P., Kroupa, P., Goodman, A., & Burkert, A. 2007, in Protostars and Planets V, ed. B. Reipurth, D. Jewitt, & K. Keil (Tucson, AZ: Univ. Arizona Press), 133

Goodwin, S. P., Whitworth, A. P., & Ward-Thompson, D. 2004a, A&A, 414, 633

——. 2004b, A&A, 423, 169

Gould, A., & Salim, S. 2003, ApJ, 582, 1001

Guieu, S., Dougados, C., Monin, J., Magnier, E., & Martín, E. L. 2006, A&A, 446, 485

Gunn, J. E., et al. 1998, AJ, 116, 3040

Gunning, H. C., Schmidt, S. J., Davenport, J. R. A., Hawley, S. L., & Dhital, S. 2012, in American Astronomical Society Meeting Abstracts, Vol. 219, American Astronomical Society Meeting Abstracts, #345.16

Haisch, Jr., K. E., Greene, T. P., Barsony, M., & Stahler, S. W. 2004, AJ, 127, 1747

Halbwachs, J. L. 1986, A&AS, 66, 131

Halbwachs, J. L., Mayor, M., Udry, S., & Arenou, F. 2003, A&A, 397, 159

Harris, H. C., et al. 2006, AJ, 131, 571

Hauschildt, P. H., Allard, F., & Baron, E. 1999, ApJ, 512, 377

Hawley, S. L., Gizis, J. E., & Reid, I. N. 1996, AJ, 112, 2799

Heintz, W. D. 1969, JRASC, 63, 275

Henry, T. J., Franz, O. G., Wasserman, L. H., Benedict, G. F., Shelus, P. J., Ianna, P. A., Kirkpatrick, J. D., & McCarthy, Jr., D. W. 1999, ApJ, 512, 864

Henry, T. J., & McCarthy, D. W. J. 1993, AJ, 106, 773

Hernandez, X., Jimenez, M. A., & Allen, C. 2011, ArXiv e-prints

Hilton, E. J., West, A. A., Hawley, S. L., & Kowalski, A. F. 2010, AJ, 140, 1402

Hogg, D. W., Finkbeiner, D. P., Schlegel, D. J., & Gunn, J. E. 2001, AJ, 122, 2129

Howard, A. W., et al. 2011, ArXiv e-prints

Imamura, J. N., Durisen, R. H., & Pickett, B. K. 2000, ApJ, 528, 946

Irwin, J., Berta, Z. K., Burke, C. J., Charbonneau, D., Nutzman, P., West, A. A., & Falco, E. E. 2011, ApJ, 727, 56

Ivezić, Ž., et al. 2008a, Serbian Astronomical Journal, 176, 1

——. 2008b, ApJ, 684, 287

——. 2007, AJ, 134, 973

Jao, W.-C., Henry, T. J., Beaulieu, T. D., & Subasavage, J. P. 2008, AJ, 136, 840

Jeans, J. H. 1919, Problems of cosmogony and stellar dynamics (Cambridge, University press, 1919.)

Jessop, N. E., & Ward-Thompson, D. 2000, MNRAS, 311, 63

Jiang, Y., & Tremaine, S. 2010, MNRAS, 401, 977

Joergens, V. 2008, A&A, 492, 545

Johnson, D. R. H., & Soderblom, D. R. 1987, AJ, 93, 864

Johnson, J. A., & Apps, K. 2009, ApJ, 699, 933

Johnson, J. A., et al. 2011, ArXiv e-prints

Jurić, M., et al. 2008, ApJ, 673, 864

Kaiser, N., et al. 2010, in Society of Photo-Optical Instrumentation Engineers (SPIE) Conference Series, Vol. 7733, Society of Photo-Optical Instrumentation Engineers (SPIE) Conference Series

Keller, S. C., et al. 2007, PASA, 24, 1

Kenyon, S. J., & Hartmann, L. 1995, ApJS, 101, 117

Kilic, M., et al. 2006, AJ, 131, 582

Kirkpatrick, J. D. 2005, ARA&A, 43, 195

Kirkpatrick, J. D., Barman, T. S., Burgasser, A. J., McGovern, M. R., McLean, I. S., Tinney, C. G., & Lowrance, P. J. 2006, ApJ, 639, 1120

Kirkpatrick, J. D., et al. 2008, ApJ, 689, 1295

Kirkpatrick, J. D., Henry, T. J., & McCarthy, Jr., D. W. 1991, ApJS, 77, 417

Kirkpatrick, J. D., et al. 1999, ApJ, 519, 802

——. 2000, AJ, 120, 447

Kiseleva, L. G., Eggleton, P. P., & Mikkola, S. 1998, MNRAS, 300, 292

Kohler, R., & Leinert, C. 1998, A&A, 331, 977

Kouwenhoven, M. B. N., Goodwin, S. P., Parker, R. J., Davies, M. B., Malmberg, D., & Kroupa, P. 2010, MNRAS, 404, 1835

Kowalski, A. F., Hawley, S. L., Hilton, E. J., Becker, A. C., West, A. A., Bochanski, J. J., & Sesar, B. 2009, AJ, 138, 633

Kratter, K. M., Matzner, C. D., & Krumholz, M. R. 2008, ApJ, 681, 375

Kraus, A. L., & Hillenbrand, L. A. 2007, AJ, 134, 2340

——. 2009a, ApJ, 704, 531

——. 2009b, ApJ, 703, 1511

Kroupa, P. 1995, MNRAS, 277, 1491

Kruse, E. A., Berger, E., Knapp, G. R., Laskar, T., Gunn, J. E., Loomis, C. P., Lupton, R. H., & Schlegel, D. J. 2010, ApJ, 722, 1352

Küpper, A. H. W., Kroupa, P., Baumgardt, H., & Heggie, D. C. 2010, MNRAS, 401, 105

Larson, R. B. 1981, MNRAS, 194, 809

Larson, R. B. 2001, in IAU Symposium, Vol. 200, The Formation of Binary Stars, ed. H. Zinnecker & R. Mathieu, 93–+

Latham, D. W., Schechter, P., Tonry, J., Bahcall, J. N., & Soneira, R. M. 1984, ApJ, 281, L41

Laughlin, G., Bodenheimer, P., & Adams, F. C. 1997, ApJ, 482, 420

Law, N. M., Dhital, S., Kraus, A., Stassun, K. G., & West, A. A. 2010, ApJ, 720, 1727

Law, N. M., Kraus, A. L., Street, R. R., Lister, T., Shporer, A., & Hillenbrand, L. A. 2011, ArXiv e-prints

Lawrence, A., et al. 2007, MNRAS, 379, 1599

Laws, C., Gonzalez, G., Walker, K. M., Tyagi, S., Dodsworth, J., Snider, K., & Suntzeff, N. B. 2003, AJ, 125, 2664

Leinert, C., Zinnecker, H., Weitzel, N., Christou, J., Ridgway, S. T., Jameson, R., Haas, M., & Lenzen, R. 1993, A&A, 278, 129

Lépine, S., & Bongiorno, B. 2007, AJ, 133, 889

Lépine, S., Rich, R. M., & Shara, M. M. 2003, AJ, 125, 1598

——. 2007, ApJ, 669, 1235

Lépine, S., & Scholz, R.-D. 2008, ApJ, 681, L33

Lépine, S., & Shara, M. M. 2005, AJ, 129, 1483

Lindegren, L., Lammers, U., Hobbs, D., O'Mullane, W., Bastian, U., & Hernández, J. 2012, A&A, 538, A78

Longhitano, M., & Binggeli, B. 2010, A&A, 509, A46

Looper, D. L., Gelino, C. R., Burgasser, A. J., & Kirkpatrick, J. D. 2008a, ApJ, 685, 1183

Looper, D. L., et al. 2008b, ApJ, 686, 528

López-Morales, M. 2007, ApJ, 660, 732

Low, C., & Lynden-Bell, D. 1976, MNRAS, 176, 367

Lupton, R., Gunn, J. E., Ivezić, Z., Knapp, G. R., Kent, S., & Yasuda, N. 2001, in Astronomical Society of the Pacific Conference Series, Vol. 238, Astronomical Data Analysis Software and Systems X, ed. F. R. Harnden Jr., F. A. Primini, & H. E. Payne, 269

Luyten, W. J. 1922, Lick Observatory Bulletin, 10, 135

——. 1927, Harvard College Observatory Bulletin, 852, 14

——. 1969, Proper Motion Survey with the forty-eight inch Schmidt telescope. XXI. Double stars with common proper motion., by Luyten, W. J.. Separate print. Univ. Minnesota, Minneapolis, Minnesota, 29 p., 21, 1

——. 1972, Proper motion survey with the forty-eight inch Schmidt telescope: XXIX. Double stars with common proper motion., by Luyten, W. J.. Separate print Univ. Minnesota, Minneapolis, Minnesota, 11 p., 29, 1

——. 1977, Proper motion survey with the 48-inch Schmidt telescope. L. Double stars with common proper motion., by Luyten, W. J.. Sep. print Univ. Minnesota, Minneapolis, Minnesota, 35 p., 50, 1

——. 1979a, LHS Catalogue. A Catalogue of Stars with Proper Motions Exceeding 0″.5 Annually, 2nd edn. (Minneapolis: Univ. Minnesota)

Luyten, W. J. 1979b, in New Luyten Catalogue of Stars with Proper Motions Larger than Two Tenths of an Arcsecond, Vol. 1, 0–+

——. 1979c, Proper Motion Survey with the forty-eight inch Schmidt telescope. LII. Binaries with white dwarf components. White dwarf discovery? A travesty on the English language., by Luyten, W. J.. Separat print Univ. Minnesota, Minneapolis, Minnesota, 12 p., 52, 1

——. 1984, Proper motion survey with the 48-inch Schmidt telescope. LXIV. Doublestars with common proper motion.. Separate Print, University of Minnesota, Minneapolis, Minn. 55455, USA, 15 pp., 64, 1

——. 1987, Proper motion survey with Schmidt telescopes. LXXI. Double stars withcommon proper motion.. Separate Print, University of Minnesota, Minneapolis, Minn. 55455, USA, 2 pp., 71, 1

——. 1988, Ap&SS, 142, 17

——. 1997, VizieR Online Data Catalog, 1130, 0

Majewski, S. R. 1993, ARA&A, 31, 575

Makarov, V. V., Zacharias, N., & Hennessy, G. S. 2008, ApJ, 687, 566

Martin, D. C., et al. 2005, ApJ, 619, L1

Martín, E. L., Barrado y Navascués, D., Baraffe, I., Bouy, H., & Dahm, S. 2003, ApJ, 594, 525

Martín, E. L., Brandner, W., Bouvier, J., Luhman, K. L., Stauffer, J., Basri, G., Zapatero Osorio, M. R., & Barrado y Navascués, D. 2000, ApJ, 543, 299

Mason, B. D., Gies, D. R., Hartkopf, W. I., Bagnuolo, Jr., W. G., ten Brummelaar, T., & McAlister, H. A. 1998, AJ, 115, 821

Mason, B. D., Hartkopf, W. I., Gies, D. R., Henry, T. J., & Helsel, J. W. 2009, AJ, 137, 3358

Massey, P., Valdes, F., & Barnes, J. 1992, http://iraf.net/faqman/index.php?op=view&t=20

Mathieu, R. D. 1994, ARA&A, 32, 465

Mathieu, R. D., Ghez, A. M., Jensen, E. L. N., & Simon, M. 2000, Protostars and Planets IV, 703

Matijevič, G., et al. 2010, AJ, 140, 184

Maxted, P. F. L., & Jeffries, R. D. 2005, MNRAS, 362, L45

Mazeh, T., Goldberg, D., Duquennoy, A., & Mayor, M. 1992, ApJ, 401, 265

McElwain, M. W., & Burgasser, A. J. 2006, AJ, 132, 2074

McLean, I. S., McGovern, M. R., Burgasser, A. J., Kirkpatrick, J. D., Prato, L., & Kim, S. S. 2003, ApJ, 596, 561

Meibom, S., et al. 2011a, ApJ, 733, L9

Meibom, S., & Mathieu, R. D. 2005, ApJ, 620, 970

Meibom, S., Mathieu, R. D., & Stassun, K. G. 2009, ApJ, 695, 679

Meibom, S., Mathieu, R. D., Stassun, K. G., Liebesny, P., & Saar, S. H. 2011b, ApJ, 733, 115

Miller, G. E., & Scalo, J. M. 1979, ApJS, 41, 513

Moeckel, N., & Bate, M. R. 2010, MNRAS, 404, 721

Moeckel, N., & Clarke, C. J. 2011, MNRAS, 415, 1179

Mohanty, S., & Basri, G. 2003, ApJ, 583, 451

Mohanty, S., Basri, G., Shu, F., Allard, F., & Chabrier, G. 2002, ApJ, 571, 469

Munn, J. A., et al. 2004, AJ, 127, 3034

——. 2008, AJ, 136, 895

Nutzman, P., & Charbonneau, D. 2008, PASP, 120, 317

Offner, S. S. R., Klein, R. I., & McKee, C. F. 2008, ApJ, 686, 1174

Offner, S. S. R., Kratter, K. M., Matzner, C. D., Krumholz, M. R., & Klein, R. I. 2010, ApJ, 725, 1485

Patience, J., Ghez, A. M., Reid, I. N., & Matthews, K. 2002, AJ, 123, 1570

Patience, J., Ghez, A. M., Reid, I. N., Weinberger, A. J., & Matthews, K. 1998, AJ, 115, 1972

Peterson, D. E., et al. 2008, ApJ, 685, 313

Petr, M. G., Coude Du Foresto, V., Beckwith, S. V. W., Richichi, A., & McCaughrean, M. J. 1998, ApJ, 500, 825

Phan-Bao, N., et al. 2008, MNRAS, 383, 831

Pier, J. R., Munn, J. A., Hindsley, R. B., Hennessy, G. S., Kent, S. M., Lupton, R. H., & Ivezić, Ž. 2003, AJ, 125, 1559

Pinfield, D. J., Dobbie, P. D., Jameson, R. F., Steele, I. A., Jones, H. R. A., & Katsiyannis, A. C. 2003, MNRAS, 342, 1241

Pinfield, D. J., Jones, H. R. A., Lucas, P. W., Kendall, T. R., Folkes, S. L., Day-Jones, A. C., Chappelle, R. J., & Steele, I. A. 2006, MNRAS, 368, 1281

Poveda, A., Allen, C., Costero, R., Echevarría, J., & Hernández-Alcántara, A. 2009, ApJ, 706, 343

Poveda, A., Allen, C., & Parrao, L. 1982, ApJ, 258, 589

Press, W. H., Teukolsky, S. A., Vetterling, W. T., & Flannery, B. P. 1992, Numerical Recipes in FORTRAN. The Art of Scientific Computing, 2nd edn. (Cambridge: Cambridge Univ. Press)

Quinn, D. P., Wilkinson, M. I., Irwin, M. J., Marshall, J., Koch, A., & Belokurov, V. 2009, MNRAS, 396, L11

Radigan, J., Lafrenière, D., Jayawardhana, R., & Doyon, R. 2008, ApJ, 689, 471

——. 2009, ApJ, 698, 405

Raghavan, D., et al. 2010, ApJS, 190, 1

Ratzka, T., Köhler, R., & Leinert, C. 2005, A&A, 437, 611

Rayner, J. T., Toomey, D. W., Onaka, P. M., Denault, A. J., Stahlberger, W. E., Vacca, W. D., Cushing, M. C., & Wang, S. 2003, PASP, 115, 362

Reid, I. N., Burgasser, A. J., Cruz, K. L., Kirkpatrick, J. D., & Gizis, J. E. 2001a, AJ, 121, 1710

Reid, I. N., et al. 2003, AJ, 126, 3007

Reid, I. N., Cruz, K. L., Kirkpatrick, J. D., Allen, P. R., Mungall, F., Liebert, J., Lowrance, P., & Sweet, A. 2008, AJ, 136, 1290

Reid, I. N., & Gizis, J. E. 1997, AJ, 113, 2246

Reid, I. N., Gizis, J. E., Kirkpatrick, J. D., & Koerner, D. W. 2001b, AJ, 121, 489

Reid, I. N., Hawley, S. L., & Gizis, J. E. 1995, AJ, 110, 1838

Reid, I. N., Kirkpatrick, J. D., Liebert, J., Gizis, J. E., Dahn, C. C., & Monet, D. G. 2002, AJ, 124, 519

Reid, I. N., Turner, E. L., Turnbull, M. C., Mountain, M., & Valenti, J. A. 2007, ApJ, 665, 767

Reid, I. N., van Wyk, F., Marang, F., Roberts, G., Kilkenny, D., & Mahoney, S. 2001c, MNRAS, 325, 931

Reid, N. 1998, AJ, 115, 204

Reiners, A., & Basri, G. 2007, ApJ, 656, 1121

Reipurth, B., & Clarke, C. 2001, AJ, 122, 432

Reipurth, B., & Zinnecker, H. 1993, A&A, 278, 81

Richards, G. T., et al. 2002, AJ, 123, 2945

Rojas-Ayala, B., Covey, K. R., Muirhead, P. S., & Lloyd, J. P. 2010, ApJ, 720, L113

——. 2012, ApJ, 748, 93

Ryan, S. G. 1992, AJ, 104, 1144

Salim, S., & Gould, A. 2003, ApJ, 582, 1011

Saumon, D., & Marley, M. S. 2008, ApJ, 689, 1327

Schlaufman, K. C., & Laughlin, G. 2010, A&A, 519, A105+

Schmidt, S. J., Cruz, K. L., Bongiorno, B. J., Liebert, J., & Reid, I. N. 2007, AJ, 133, 2258

Schmidt, S. J., West, A. A., Hawley, S. L., & Pineda, J. S. 2010, AJ, 139, 1808

Scholz, R. 2010, A&A, 510, L8+

Sesar, B., Ivezić, Ž., & Jurić, M. 2008, ApJ, 689, 1244

Shao, M., & Nemati, B. 2009, PASP, 121, 41

Shkolnik, E. L., Hebb, L., Liu, M. C., Reid, I. N., & Cameron, A. C. 2010, ApJ, 716, 1522

Silvestri, N. M., Hawley, S. L., & Oswalt, T. D. 2005, AJ, 129, 2428

Silvestri, N. M., et al. 2006, AJ, 131, 1674

Simon, M., Close, L. M., & Beck, T. L. 1999, AJ, 117, 1375

Simons, D. A., & Tokunaga, A. 2002, PASP, 114, 169

Skrutskie, M. F., et al. 2006, AJ, 131, 1163

Skumanich, A. 1972, ApJ, 171, 565

Smith, J. A., et al. 2002, AJ, 123, 2121

Soderblom, D. R. 2010, ARA&A, 48, 581

Stahler, S. W., & Palla, F. 2005, The Formation of Stars (Wiley-VCH)

Stassun, K. G., Mathieu, R. D., Cargile, P. A., Aarnio, A. N., Stempels, E., & Geller, A. 2008, Nature, 453, 1079

Stassun, K. G., Mathieu, R. D., & Valenti, J. A. 2007, ApJ, 664, 1154

Stauffer, J. R., et al. 1999, ApJ, 527, 219

Stauffer, J. R., & Hartmann, L. W. 1986, ApJS, 61, 531

Stauffer, J. R., Schultz, G., & Kirkpatrick, J. D. 1998, ApJ, 499, L199+

Stelzer, B., Micela, G., Flaccomio, E., Neuhäuser, R., & Jayawardhana, R. 2006, A&A, 448, 293

Stephens, D. C., et al. 2009, ApJ, 702, 154

Stoughton, C., et al. 2002, AJ, 123, 485

Strauss, M. A., et al. 2002, AJ, 124, 1810

Terrien, R. C., Mahadevan, S., Bender, C. F., Deshpande, R., Ramsey, L. W., & Bochanski, J. J. 2012, ApJ, 747, L38

Thies, I., & Kroupa, P. 2007, ApJ, 671, 767

Tohline, J. E. 2002, ARA&A, 40, 349

Tokovinin, A. A. 1997, Astronomy Letters, 23, 727

——. 2000, A&A, 360, 997

Tokunaga, A. T., & Kobayashi, N. 1999, AJ, 117, 1010

Tokunaga, A. T., Simons, D. A., & Vacca, W. D. 2002, PASP, 114, 180

Tsuji, T., Ohnaka, K., Aoki, W., & Jones, H. R. A. 1998, Highlights of Astronomy, 11, 439

Tucker, D. L., et al. 2006, Astronomische Nachrichten, 327, 821

Unwin, S. C., et al. 2008, PASP, 120, 38

Vacca, W. D., Cushing, M. C., & Rayner, J. T. 2003, PASP, 115, 389

Valenti, J. A., & Fischer, D. A. 2005, ApJS, 159, 141

——. 2008, Physica Scripta Volume T, 130, 014003

Voges, W., et al. 1999, VizieR Online Data Catalog, 9010, 0

Walkowicz, L. M., & Hawley, S. L. 2009, AJ, 137, 3297

Walkowicz, L. M., Hawley, S. L., & West, A. A. 2004, PASP, 116, 1105

Wasserman, I., & Weinberg, M. D. 1991, ApJ, 382, 149

Watkins, S. J., Bhattal, A. S., Boffin, H. M. J., Francis, N., & Whitworth, A. P. 1998a, MNRAS, 300, 1205

——. 1998b, MNRAS, 300, 1214

Weinberg, M. D., Shapiro, S. L., & Wasserman, I. 1987, ApJ, 312, 367

Weistrop, D. 1972, AJ, 77, 366

West, A. A., & Basri, G. 2009, ApJ, 693, 1283

West, A. A., Bochanski, J. J., Hawley, S. L., Cruz, K. L., Covey, K. R., Silvestri, N. M., Reid, I. N., & Liebert, J. 2006, AJ, 132, 2507

West, A. A., Hawley, S. L., Bochanski, J. J., Covey, K. R., Reid, I. N., Dhital, S., Hilton, E. J., & Masuda, M. 2008, AJ, 135, 785

West, A. A., et al. 2004, AJ, 128, 426

——. 2011, AJ, 141, 97

West, A. A., Walkowicz, L. M., & Hawley, S. L. 2005, PASP, 117, 706

White, R. J., & Ghez, A. M. 2001, ApJ, 556, 265

White, R. J., Ghez, A. M., Reid, I. N., & Schultz, G. 1999, ApJ, 520, 811

Whitworth, A. P., & Zinnecker, H. 2004, A&A, 427, 299

Wielen, R. 1977, A&A, 60, 263

Witte, S., Helling, C., Barman, T., Heidrich, N., & Hauschildt, P. H. 2011, A&A, 529, A44+

Woolf, V. M., Lépine, S., & Wallerstein, G. 2009, PASP, 121, 117

Woolf, V. M., & Wallerstein, G. 2005, MNRAS, 356, 963

Wright, E. L., et al. 2010, AJ, 140, 1868

Yoo, J., Chanamé, J., & Gould, A. 2004, ApJ, 601, 311

York, D. G., et al. 2000, AJ, 120, 1579

Zapatero Osorio, M. R., Béjar, V. J. S., Pavlenko, Y., Rebolo, R., Allende Prieto, C., Martín, E. L., & García López, R. J. 2002, A&A, 384, 937

Zapatero Osorio, M. R., & Martín, E. L. 2004, A&A, 419, 167

Zuckerman, B., & Song, I. 2009, A&A, 493, 1149

# LIST OF ABBREVIATIONS

| | |
|---|---|
| 2MASS | Two Micron All Sky Survey |
| AMR | Adaptive Mesh Refinement |
| BD | Brown dwarfs |
| CCF | cross-correlation function |
| CPM | Common Proper Motion |
| dM | M dwarfs; metallicity class defined by LRS07 |
| DM91 | Duquennoy & Mayor (1991) |
| esdM | M extreme subdwarfs; metallicity class defined by LRS07 |
| LMS | Low-mass Star |
| LOS | Line of sight |
| LRS07 | Lépine, Rich, & Shara (2007) |
| LSST | Large Synoptic Survey Telescope |
| MS | Main sequence |
| PMS | Pre-main sequence |
| sdM | M subdwarfs; metallicity class defined by LRS07 |
| SDSS | Sloan Digital Sky Survey |
| SIM | Space Interferometry Mission |
| SLoWPoKES | Sloan Low-mass Wide Pairs of Kinematically Equivalent Stars |
| SPH | Smoothed Particle Hydrodynamics |
| UKIDSS | UKIRT Infrared Deep Sky Survey |

| | |
|---|---|
| usdM | M ultra subdwarfs; metallicity class defined by LRS07 |
| VLM | Very Low-mass |
| WBF | Wide binary fraction |

# APPENDIX A

## SQL CASJOBS QUERY USED IN SLoWPoKES

1. Search for all low-mass stars in SDSS DR7 CasJobs ($r \leq 20$, $\mu \geq 40$)

   Context: DR7

```
SELECT S.objID,S.ra,S.dec,S.psfmag_r
INTO mydb.LMSpm40
FROM Star S, ProperMotions pm
WHERE
  S.psfmag_r between 0 AND 20 AND
  (S.psfMag_r - S.psfMag_i) >= 0.3 AND
  (S.psfMag_i - S.psfMag_z) >= 0.2 AND
  SQRT(POWER(pm.pmra,2) + POWER(pm.pmdec,2)) >= 40
```

2. Create a table for results to be stored (necessary to use SpGetNeighbors).

   Context: MYDB

```
CREATE TABLE SDSSmatches(
  targetID bigint, objID bigint,
  ra float, dec float,
  pmra float, pmdec float, pmraerr float, pmdecerr float,
  run smallint, rerun smallint, camcol tinyint,
  field smallint, obj smallint,
  psfMag_u float, psfMag_g float, psfMag_r float,
  psfMag_i float, psfMag_z float,
  psfMagErr_u float, psfMagErr_g float, psfMagErr_r float,
  psfMagErr_i float, psfMagErr_z float,
  extinction_u float, extinction_g float,extinction_r float,
  extinction_i float, extinction_z float,
  flags_u bigint, flags_g bigint, flags_r bigint,
  flags_i bigint, flags_z bigint,
  status bigint, SpecObjID bigint,
  pmL float, pmB float, delta float, match int, nFit int, dist22 int,
  sigRa float, sigDec float, usnoO float, usnoJ float);
```

3. Run the query using SpGetNeighbors for all matching stellar objects within $\Delta\theta \leq 180''$.

   Context: DR7

```
-- create a temporary table in which to upload your search objects
CREATE TABLE #upload (up_ra FLOAT, up_dec FLOAT, up_id BIGINT);
-- upload the search object
INSERT INTO #upload SELECT RA as up_ra, DEC as up_dec, OBJID as up_id
  FROM MYDB.LMSpm40
-- create a temporary table to save your results of your query
CREATE TABLE #tmp (up_id BIGINT, objID BIGINT);
-- run spGetNeigbors which saves
-- the objID of your target and found objects into #tmp
INSERT INTO #tmp EXEC spGetNeighbors 3

-- extract the data fields for all the objects
-- that were recovered in the search
INSERT INTO MYDB.SDSS SELECT
  t.up_id as targetID, t.objID,
  S.ra, S.dec, pm.pmra, pm.pmdec, pm.pmraerr, pm.pmdecerr,
  S.run, S.rerun, S.camcol, S.field, S.obj,
  S.psfMag_u, S.psfMag_g, S.psfMag_r, S.psfMag_i, S.psfMag_z,
  S.psfMagErr_u, S.psfMagErr_g, S.psfMagErr_r,
  S.psfMagErr_i, S.psfMagErr_z,
  S.extinction_u, S.extinction_g, S.extinction_r,
  S.extinction_i, S.extinction_z,
  S.flags_u, S.flags_g, S.flags_r, S.flags_i, S.flags_z,
  S.status, S.type, S.SpecObjID,
  pm.pmL, pm.pmB, pm.delta, pm.match, pm.nFit, pm.dist22,
  pm.sigRa, pm.sigDec, pm.O as usnoO, pm.J as usnoJ

FROM #tmp t, MYDB.LMSpm40 LMS, dr7.Star S, dr7.ProperMotions pm
WHERE
  t.up_id = LMS.objID AND
  t.objID = S.objID AND
  t.objID = pm.objID AND
  SQRT(POWER(pm.pmra,2) + POWER(pm.pmdec,2)) >= 20 AND
  S.psfMag_r <=20
ORDER BY t.up_id
```

# APPENDIX B

## SQL CASJOBS QUERY USED IN SLoWPoKES-II

1. Search for all low-mass stars in SDSS DR7 CasJobs ($0 < r \leq 22.5$)

   Context: DR8

```
-- define bad_flags so as to reject objects with
-- bad or possibly contaminated photometry
declare @PEAKCENTER bigint set
  @PEAKCENTER=dbo.fPhotoFlags('PEAKCENTER')
declare @NOTCHECKED bigint set
  @NOTCHECKED=dbo.fPhotoFlags('NOTCHECKED')
declare @PSF_FLUX_INTERP bigint set
  @PSF_FLUX_INTERP=dbo.fPhotoFlags('PSF_FLUX_INTERP')
declare @INTERP_CENTER bigint set
  @INTERP_CENTER=dbo.fPhotoFlags('INTERP_CENTER')
declare @BAD_COUNTS_ERROR bigint set
  @BAD_COUNTS_ERROR=dbo.fPhotoFlags('BAD_COUNTS_ERROR')
declare @SATURATED bigint set
  @SATURATED=dbo.fPhotoFlags('SATURATED')
declare @BRIGHT bigint set @BRIGHT=dbo.fPhotoFlags('BRIGHT')
declare @NODEBLEND bigint set
  @NODEBLEND=dbo.fPhotoFlags('NODEBLEND')
declare @DEBLEND_NOPEAK bigint set
  @DEBLEND_NOPEAK=dbo.fPhotoFlags('DEBLEND_NOPEAK')
declare @bad_flags bigint set
  @bad_flags=(@PEAKCENTER|@NOTCHECKED|@PSF_FLUX_INTERP|
  @INTERP_CENTER|@BAD_COUNTS_ERROR|@SATURATED|@BRIGHT|
  @NODEBLEND|@DEBLEND_NOPEAK)

SELECT objID, ra, dec INTO boo
FROM Star S
WHERE (flags & @bad_flags) = 0 and nChild = 0
  and (psfmag_r-psfmag_i) > 0.54 and (psfmag_i-psfmag_z) > 0.31
  and psfmag_r > 0 and psfmag_r <= 22.5
  and abs(psfMagErr_r) <= 0.05 and abs(psfMagErr_i) <= 0.05
  and abs(psfMagErr_z) <= 0.05
```

2. Run the query using the NEIGBORS table. Note: this query will need to be run in smaller batches, otherwise the output file will be ∼100 GB big. For our run, the numbers of targets was around 200,000 for each search. The number of fields that are extracted are minimized for the same reason.

   Context: DR8

```
-- define bad_flags so as to reject objects with
-- bad or possibly contaminated photometry
declare @PEAKCENTER bigint set
  @PEAKCENTER=dbo.fPhotoFlags('PEAKCENTER')
declare @NOTCHECKED bigint set
  @NOTCHECKED=dbo.fPhotoFlags('NOTCHECKED')
declare @PSF_FLUX_INTERP bigint set
  @PSF_FLUX_INTERP=dbo.fPhotoFlags('PSF_FLUX_INTERP')
declare @INTERP_CENTER bigint set
  @INTERP_CENTER=dbo.fPhotoFlags('INTERP_CENTER')
declare @BAD_COUNTS_ERROR bigint set
  @BAD_COUNTS_ERROR=dbo.fPhotoFlags('BAD_COUNTS_ERROR')
declare @SATURATED bigint set
  @SATURATED=dbo.fPhotoFlags('SATURATED')
declare @BRIGHT bigint set @BRIGHT=dbo.fPhotoFlags('BRIGHT')
declare @NODEBLEND bigint set
  @NODEBLEND=dbo.fPhotoFlags('NODEBLEND')
declare @DEBLEND_NOPEAK bigint set
  @DEBLEND_NOPEAK=dbo.fPhotoFlags('DEBLEND_NOPEAK')
declare @bad_flags bigint set
  @bad_flags=(@PEAKCENTER|@NOTCHECKED|@PSF_FLUX_INTERP|
  |@INTERP_CENTER|@BAD_COUNTS_ERROR|@SATURATED|@BRIGHT|
  @NODEBLEND|@DEBLEND_NOPEAK)

SELECT
  N.objID as target_id, N.NeighborObjID as objID,
  round(S.ra,6) as ra, round(S.dec,6) as dec,
  round(S.psfMag_u,3) as psfmag_u, round(S.psfMagErr_u,3) as psfmagErr_u,
  round(S.psfMag_g,3) as psfmag_g, round(S.psfMagErr_g,3) as psfmagErr_g,
  round(S.psfMag_r,3) as psfmag_r, round(S.psfMagErr_r,3) as psfmagErr_r,
  round(S.psfMag_i,3) as psfmag_i, round(S.psfMagErr_i,3) as psfmagErr_i,
  round(S.psfMag_z,3) as psfmag_z, round(S.psfMagErr_z,3) as psfmagErr_z,
  round(S.extinction_r,3) as extinction_r
INTO MYDB.SDSSresults

FROM MYDB.LMS as LMS,
```

```
  Neighbors as N JOIN STAR as S on S.objID = N.NeighborObjID
WHERE N.objID = L.objID
  and N.mode = 1
  and (N.neighborMode = 1 or N.neighborMode = 2)
  and N.type = 6 and N.neighborType = 6
  and (S.flags_r & S.flags_i & S.flags_z & @bad_flags) = 0
  and S.nChild = 0
ORDER BY N.objID
```

# APPENDIX C

## IDL CODE FOR THE GALACTIC MODEL

```
PRO SLW_MODEL,outfile=outfile

;+
; NAME:
;       SLW_MODEL
; PURPOSE:
;       Calculate probability of chance alignment for a CPM binary candidate
;
; EXPLANATION:
;       This program calculates calculates the probability of chance
;       alignment for a candidate binary pair using a Monte Carlo Galactic
;       model. The Galactic model is based on empirical stellar number density
;       (Juric et al., 2008, ApJ, 673, 864; Bochanski et al., 2010, AJ, 139,
;       2679) and space velocity distributions (Bochanski et al., 2007, AJ,
;       134, 2418).  In essence, the model uses the input phase space
;       parameters (3 positions, 3 velocities) and calculates how many other
;       stars are expected in that  6D phase space ellipsoid. The simulated
;       stars are redistributedin  position and velocity space using the
;       rejection method (Press et al., 1992). The probability of chance
;       alignment is then simply the total number of stars found  in the
;       simulated ellipsoid per realization. The full algorithm is described
;       in Dhital et al. (2010, AJ, 139, 2566). Currently, the third velocity
;       dimension, radial velocity, is not included in the model but can be
;       added with a trivial amount of code.
;
; CALLING SEQUENCE:
;       slw_model,infile,outfile=outfile,nstepsMC=nstepsMC
;
; INPUTS:
;       INFILE - name of the input FITS file with at least the following fields:
;
;                RA   - Right Ascension of binary (or primary) in decimal deg
;                DEC  - Declination of the binary (or primary) in decimal deg
;                DIST - heliocentric distance of binary (or primary) in parsecs
;                dtheta - Angular separation binary (or primary) in arcseconds
;                pmRA     - Proper motion in Right Ascension of binary (or primary)
```

```
;                pmDEC    - Proper motion in Declination of binary (or primary)
;                pmRAerr  - Error in Proper motion in RA of binary (or primary)
;                pmDECerr - Error in Proper motion in DEC of binary (or primary)
;                    All proper motions are in arcseconds/yr
;
; OPTIONAL KEYWORD INPUTS:
;       OUTFILE  - Name of the output file.
;                  By default, the results will be printed to the screen
;       nstepsMC - Number of Monte Carlo realizations for the model
;                  By default, 10^5 realizations are run
;
; OUTPUTS:
;       outfile_prob.dat: Data file containing
;                RA     --> Right Ascension of simulated ellipsoid
;                DEC    --> Declination of simulated ellipsoid
;                DIST   --> Distance of simulated ellipsoid
;                P1     --> P(chance alignment | theta)
;                P2     --> P(chance alignment | theta, distance)
;                P3     --> P(chance alignment | theta, pmRA, pmDEC)
;                Nstars --> No. of stars simulated ellipsoid
;
;       outfile_theta.dat: Data file containing the cumulative number
;                          of stars as a function of angular
;                          separation in 1 arcsec bins where
;                theta  --> angular separation
;                theta  --> No. of stars | theta
;                theta  --> No. of stars | theta, distance
;                theta  --> No. of stars | theta, distance, pmRA, pmDEC
;
; EXAMPLE:
;       IDL> slw_model,'binary',outfile='binary_model',nstepsMC=1000
;
; PROCEDURES CALLED:
;
; REVISION HISTORY:
;       Written    S. Dhital             April, 2009
;-
On_error,2                              ;Return to caller
compile_opt idl2

FORWARD_FUNCTION gen_nstars,gen_pm,gen_2Dgaussian
FORWARD_FUNCTION calc_sigmaVel,calc_rho,count_nstars
FORWARD_FUNCTION conv_to_galactic,conv_to_equatorial,calc_UVW
astrolib
```

```
COMMON CONSTS,Rsun,Tsun,Zsun,rho0,au2pc,cell_size,max_dist,seed
Rsun = 8500.d    ; R, theta, & Z coords FOR the sun in parsecs
Tsun = 0.d
Zsun = 15.d
rho0 = 0.0064d                  ; rho0 from Juric et al. (2008)
au2pc = 1.d/206264.806          ; conversion from AU to parsecs
cell_size = 0.5d                ; size of one cell in degrees
max_dist = 2500.d    ; maximum allowed distance for simulated star
seed = ranseed()

nstepsMC = 1e5                 ; no. Monte Carlo steps

; ****************************************************************
; ****************************************************************
print,'Start Time: ',systime(0)
t_start = systime(1)

bry = mrdfits(infile,1)
n = n_elements(bry)

print,'No. of input binary candidates: ',n
print,'No. of MC steps per candidate : ',nstepsMC

; storage arrays
nstars = lonarr(n)            ; stores no. of stars in each 30'x30'LOS
count_star = lonarr(n,3)       ; stores no. of companions for each LOS

plothist,[-1,181],theta_x,theta_tot1,bin=1,/noplot,/halfbin
theta_tot2 = theta_tot1 & theta_tot3 = theta_tot1

FOR i = 0l,n-1 DO BEGIN      ; loop for each LOS (binary)

    ra0    = bry[i].ra1       ; system properties are subscripted with 0
    dec0   = bry[i].dec1
    theta0 = bry[i].dtheta

    dist0  = 0.5*(bry[i].dist1 + bry[i].dist2)
    sig_ddist0 = 0.1383*sqrt(bry[i].dist1^2 + bry[i].dist2^2)

    pm0  = 0.5*[bry[i].pmra1+bry[i].pmra2, bry[i].pmdec1+bry[i].pmdec2]
    sigpm0  = [sqrt(bry[i].pmraerr1^2  + bry[i].pmraerr2^2),$
               sqrt(bry[i].pmdecerr1^2 + bry[i].pmdecerr2^2)]

    temp   = conv_to_galactic(ra0,dec0,dist0,R0,T0,Z0)
```

```
; ************************************************************
; ********************      CALC PROB    *********************
; ************************************************************
                                ; storage arrays
    count_MC = lonarr(3)        ; store data for each niter
    theta_arr1 = 0. & theta_arr2 = 0. & theta_arr3 = 0.

    ; count the number of stars in each cell of length cell_size
    nstars[i] = round(count_nstars(ra0,dec0))

    FOR niter = 0l,nstepsMC-1 DO BEGIN
        temp = gen_nstars(ra0,dec0,nstars[i],ra,dec,dist)

        theta = angdist(ra0,dec0,ra,dec)
        ddist = abs(dist-dist0)

          ; ************** COUNT FOR MATCHES  *******************
        ; counts all stars within given theta and all d
        ind1 = where(theta GE 0. AND theta LE 180,count1)
        ; counts stars within given theta and 26% of given d
        ind2 = where(theta GE 0. AND theta LE 180 AND $
                     ddist LE sig_ddist0 AND ddist LE 100,count2)
        IF count2 GT 0 THEN BEGIN
           ; returns [[pmra], [pmdec]]
           pm = gen_pm(R0,T0,Z0,ra0,dec0,dist0,count2)

            dpmRA  = abs(pm[*,0]-pm0[0])/sigpm0[0]
            dpmDEC = abs(pm[*,1]-pm0[1])/sigpm0[1]

            ind3 = where(dpmRA^2+dpmDEC^2 le 2,count3)
        ENDIF ELSE count3 = 0

         ; ******************** STORE DATA FOR EACH NITER  ********
        count_MC += [count1,count2,count3]

        IF count1 NE 0 THEN theta_arr1 = [theta_arr1,theta[ind1]]
        IF count2 NE 0 THEN theta_arr2 = [theta_arr2,theta[ind2]]
        IF count3 NE 0 THEN theta_arr3 = [theta_arr3,theta[ind2[ind3]]]

    ENDFOR                      ; END of ONE MC STEP

        ; ********************** STORE DATA FOR EACH STAR ***********
    count_star[i,*] = count_MC

    IF count_star[i,0] NE 0 THEN BEGIN
```

```
        plothist,[-1,theta_arr1[1:*],181],x1,h1,bin=1,/noplot,/halfbin
        theta_tot1 += h1
    ENDIF
    IF count_star[i,1] NE 0 THEN BEGIN
        plothist,[-1,theta_arr2[1:*],181],x1,h1,bin=1,/noplot,/halfbin
        theta_tot2 += h1
    ENDIF
    IF count_star[i,2] NE 0 THEN BEGIN
        plothist,[-1,theta_arr3[1:*],181],x1,h1,bin=1,/noplot,/halfbin
        theta_tot3 += h1
    ENDIF

    IF (i MOD round(0.1*n)) EQ 0 THEN $
      print,systime(),(100.*i/n),'% done. N = ',i+1,$
      FORMAT='(a,f8.1,a,i-5)'

ENDFOR                          ; END of ONE STAR

prob  = count_star/nstepsMC
theta = [[theta_tot1],[theta_tot2],[theta_tot3]]/(n*nstepsMC)

format = '(2(f13.7),f8.1,3(f14.5),i8'
IF keyword_set(outfile) THEN BEGIN
   COMMENT=['RA','DEC','DIST','P1','P1','P1','nstars']
   print,comment,format='2(a13),a8,3(a14),a8'

   forprint,ra1,dec1,dist,prob[*,0],prob[*,1],prob[*,2],nstars,$
            text=outfile,format=format,COMMENT=comment
    forprint,theta_x,theta[*,0],theta[*,1],theta[*,2],$
             text=outfile+'_theta.dat'
ENDIF ELSE BEGIN
    print,'            *************               '
    print,'            *************               '
    forprint,bry.ra1,bry.dec1,prob[*,0],prob[*,1],prob[*,2],nstars,$
             format=format
ENDELSE
print,'TOTAL TIME TAKEN   : ',(systime(1)-t_start)/3600.,' hours'
print,'TIME TAKEN PER LOS : ',(systime(1)-t_start)/(60*n),' minutes'
print,'END TIME           : ',systime(0)
END
```

```
; ************************************************************
; ***************      FUNCTIONS             ***************
; ************************************************************

; generate the proper motions for a given number of stars (num) based
; on the space velocity distributions which are quantified as
; [U, V, W] = f([ R, Theta, Z]) (Bochanski et al. 2007)
; LSR velocities are assumed

FUNCTION GEN_PM,R0,T0,Z0,ra0,dec0,dist0,num
COMMON CONSTS,Rsun,Tsun,Zsun,rho0,au2pc,cell_size,max_dist,seed

; calculate the UVW velocity dispersions
; returns [U_thin,V_thin,W_thin,U_thick,V_thick,W_thick]
sigmaa = calc_sigmaVel(Z0)

; calc the frac of thin/thick disk stars
; returns frac = [f_thin, f_thick, f_halo]
temp = calc_rho(R0,Z0,frac=frac)

; convert to cartesian velocities
; returns [U,V,W]
vel = calc_UVW(R0,T0,Z0)-calc_UVW(Rsun,Tsun,Zsun)


; draw from both the thin and thick disks for UVW velocities
U = gen_2Dgaussian(vel[0],sigmaa[0],sigmaa[3],frac[0],1-frac[0],num)
V = gen_2Dgaussian(vel[1],sigmaa[1],sigmaa[4],frac[0],1-frac[0],num)
W = gen_2Dgaussian(vel[2],sigmaa[2],sigmaa[5],frac[0],1-frac[0],num)

; change UVW to pmra and pmdec
ra = fltarr(num)+ra0
dec = fltarr(num)+dec0
dist = fltarr(num)+dist0
gal_uvw_pm,pmra,pmdec,U=U,V=V,W=W,/LSR,ra=ra,dec=dec,dist=dist

RETURN,[[pmra],[pmdec]]
END

; generate values from a 2D Gaussian distribution
; values are generated using the rejection algorithm from between
; +/-5 sigma of the mean of each of the distributions

FUNCTION GEN_2DGAUSSIAN,mu,sig1,sig2,f1,f2,num
n_acc = 0l                ; number of stars accepted
```

```
WHILE n_acc LT num DO BEGIN
    n_lft = num - n_acc ; no. of needed stars

    ; generate random numbers between (-5,5) sigma of a normalized gaussian
    X = randomu(seed,n_lft)*10*sig2 - 5*sig2

;    X = num_gen(-5*sig2,5*sig2,0.1)
    z1 = (X-mu)/sig1 & z2 = (X-mu)/sig2
    G1 = 1/(sqrt(2*!dpi)*sig1)*exp(-z1^2/2) ; thin disk
    G2 = 1/(sqrt(2*!dpi)*sig2)*exp(-z2^2/2) ; thin disk

    Px = f1*G1+f2*G2
    Fx = 1.2*max(Px)

    rand = randomu(seed,n_lft)
    ind = where(rand LT Px/Fx, count) ; uniformm deviate comp function

    IF count NE 0 THEN BEGIN
        IF n_acc EQ 0 THEN Xarr = x[ind] ELSE Xarr = [Xarr,x[ind]]
        n_acc += count
    ENDIF
ENDWHILE

RETURN,Xarr
END

; count the number of stars at heliocentric distances of 0-2500 pc
; (these limits can be changed) for a given RA, DEC, and angular
; radius of 30 arcmins. The intergration is done in 5 pc bins and along
; seven different points within the 30 arcmins. The latter is done such
; that the difference in densities within the radius is accounted for.
FUNCTION COUNT_NSTARS,ra,dec
COMMON CONSTS,Rsun,Tsun,Zsun,rho0,au2pc,cell_size,max_dist,seed

ddist = 5                       ; steps in distance in pc
n = max_dist/ddist + 1
nstars = fltarr(n)
dist = findgen(n)*ddist         ; 0 < d < 2500 in 5 pc steps
rho  = fLTarr(n) ; create an array to store rho FOR each d

; define fractional positions so that rho can be averaged
x = cell_size*[-0.5, 0.0, 0.5,-0.25, 0.25,-0.5,$
               0.0, 0.5,-0.25,0.25,-0.5,0.0,0.5]
y = cell_size*[-0.5,-0.5,-0.5,-0.25,-0.25, 0.0,$
               0.0,0.0, 0.25,0.25, 0.5,0.5,0.5]
```

```
; change to galactic coordinates (R,Z) from input convert (ra, dec, dist)
FOR k = 0,n_elements(dist)-1 DO BEGIN
    temp = conv_to_galactic(ra+x,dec+y,dist[k],R,Z,1)

    rho[k] = mean(calc_rho(R,Z)) ; calculate the stellar density
    ; volume at that d = pi * r^2 * h
    vol = !dpi * (1800.*dist[k]*au2pc)^2 * 5.d
    nstars[k] = rho[k] * vol
ENDFOR
nstars_tot = total(nstars)

RETURN,nstars_tot
END

; redistribute the stars around the given RA and DEC within the
30 armin radius and 2500 pc using the rejection algorithm.
FUNCTION GEN_NSTARS,ra0,dec0,num,ra,dec,dist
COMMON CONSTS,Rsun,Tsun,Zsun,rho0,au2pc,cell_size,max_dist,seed

; ra0,dec0,num - input parameters
; ra,dec,dist - output arrays for the generated stars

seed = ranseed()
n_acc = 0l                ; number of stars accepted

WHILE n_acc LT num DO BEGIN
    n_lft = num - n_acc ; no. of needed stars

    ra1   = ra0 + randomu(seed,n_lft)*cell_size
    dec1  = dec0+ randomu(seed,n_lft)*cell_size
    dist1 = randomu(seed,n_lft)*max_dist

    temp = conv_to_galactic(ra1,dec1,dist1,R,Z,1)

    rho = calc_rho(R,Z)

    rand = randomu(seed,n_lft)

    ; accept if random number is less than rho(R,Z)/rho0
    ind = where(rand LT rho/rho0, count)

    IF count NE 0 THEN BEGIN
        IF n_acc EQ 0 THEN BEGIN
            ra   = ra1[ind]
```

```
            dec  = dec1[ind]
            dist = dist1[ind]
        ENDIF ELSE BEGIN
            ra   = [ra,ra1[ind]]
            dec  = [dec,dec1[ind]]
            dist = [dist,dist1[ind]]
        ENDELSE
        n_acc += count
    ENDIF
ENDWHILE

RETURN,0
END

; calculate the stellar number density for a given R, theta, Z
; densities are calculated separately for the thin disk, thick disk,
; and the halo
FUNCTION CALC_RHO,R,Z,frac=frac
COMMON CONSTS,Rsun,Tsun,Zsun,rho0,au2pc,cell_size,max_dist,seed

H_thin = 255.d  & H_thick = 1360.d  ; scale height in pc
L_thin = 2200.d & L_thick = 4100.d ; scale length in pc

; stellar density in the solar neighborhood
f_thick = 0.03d & f_halo = 0.0025
f_thin = 1 - f_thick - f_halo

r_halo = 2.77                   ; halo density gradient
q = 0.64                        ; halo flattening parameter

rho_thin  = rho0 * exp(-abs(Z-Zsun)/H_thin)  * exp(-(R-Rsun)/L_thin)
rho_thick = rho0 * exp(-abs(Z-Zsun)/H_thick) * exp(-(R-Rsun)/L_thick)
rho_halo  = rho0 * (Rsun/sqrt(R^2+(Z/q)^2))^r_halo

rho  = f_thin*rho_thin + f_thick*rho_thick + f_halo*rho_halo
frac = [f_thin*rho_thin, f_thick*rho_thick, f_halo*rho_halo]/rho

RETURN,rho
END
```

```
; calculate the UVW velocities for given R, theta, Z
FUNCTION CALC_UVW,R,theta,Z

Rdot = 0.d
Tdot = (210.-0.013*Z-1.56e-5*Z^2)/R
Zdot = 0.d                    ; typical values for the MW in km/s

theta = theta*!DTOR

Xdot =   Rdot*COS(theta) - Tdot*SIN(theta)
Ydot = -(Rdot*SIN(theta) + Tdot*COS(theta))

RETURN,[Xdot,Ydot,Zdot]

END

; convert Galactic coordinates (R, theta, Z) to equatorial coordinates (ra, dec, d)
FUNCTION CONV_TO_EQUATORIAL,R,theta,Z,ra,dec,d
COMMON CONSTS,Rsun,Tsun,Zsun,rho0,au2pc,cell_size,max_dist,seed

dcosb = SQRT(R^2+Rsun^2-2*R*Rsun*COS(theta*!DTOR))

l = ASIN(R*SIN(theta*!DTOR)/dcosb) * !RADEG
IF l LT 0 THEN BEGIN                          ; 3rd or 4th quadrant
   IF cos(l) GT 0 THEN l = 180-l ELSE l=360+l ; 3rd else 4th
ENDIF

IF l GE 0 THEN BEGIN                          ; 1st or 2nd quadrant
   IF cos(l) GT 0 THEN l=l ELSE l=180-l       ; 1st else 2nd
ENDIF

b = ABS(ATAN((Z-Zsun)/dcosb) + ATAN(Zsun/Rsun)) * !RADEG
IF z LT 0 THEN b = -b
d = dcosb/COS(b*!DTOR)
euler,l,b,ra,dec,2

RETURN,0
END

; convert cartesian coordinates (R, theta, Z) to Galactic coordinates (ra, dec, d)
FUNCTION CONV_TO_GALACTIC,ra,dec,d,r,t,z
COMMON CONSTS,Rsun,Tsun,Zsun,rho0,au2pc,cell_size,max_dist,seed

euler,ra,dec,l,b,1
```

```
r = SQRT( (d*COS(b*!DTOR))^2 + Rsun *(Rsun- 2*d*COS(b*!DTOR)*COS(l*!DTOR)))
t = ASIN(d*SIN(l*!DTOR)*COS(b*!DTOR)/R) * !RADEG
z = Zsun + d * SIN(b*!DTOR - ATAN(Zsun/Rsun))

RETURN, 0
END


; calculate the dispersion of UVW velocities (thin and thick disk)
; as a function of Z
FUNCTION CALC_SIGMAVEL,Z

; U_thin,V_thin,W_thin,U_thick,V_thick,W_thick
; Values obtained by fitting sigma = coeff * Z^power
; data from Bochanski et al. (2006)
; see ~/sdss/uw/velocity_ellipsoid.pro[.ps] FOR fitting algorithm[fit]
coeff = [7.085,3.199,3.702,10.383,1.105,5.403]
power = [0.276,0.354,0.307, 0.285,0.625,0.309]

; calculate sigma_vel from the empirical power-law fit
sigmaa = coeff * abs(Z)^power

RETURN,sigmaa
END
```